Exchange Bias in Nanostructures

Robert Carpenter

Doctor of Philosophy

University of York

Physics

April 2015

Abstract

This study was concerned with two issues facing the technological application of exchange bias. The first is the ferromagnet (F)/antiferromagnet (AF) interface which was investigated via the effect of the IrMn (111) in-plane texture on the magnetisation reversal of IrMn/CoFe samples. The second is the change in the magnitude of the exchange bias H_{ex} and the median blocking temperature $\langle T_b \rangle$ with element size in sub-500nm nanostructures.

The evolution of the magnetisation reversal over the annealing/field cooling process in CoFe and CoFe/IrMn thin films was measured for samples deposited on Cu and NiCr seed layers. The samples deposited on the Cu seed layer were found to be polycrystalline but randomly oriented whilst those on a NiCr seed layer had a strong (111) in-plane texture. The training effect is the change in the first point to reversal H_{c1} between the first and second hysteresis loops measured after field cooling. This was found to vary drastically with texture where ΔH_{c1} was found to be (10$\pm$2.5)Oe and (60$\pm$2.5)Oe for the samples deposited on the NiCr and Cu seed layers respectively.This was hypothesised to be due to a distribution of orientation of the easy axis of the interfacial spin clusters. In the case of the sample deposited on the Cu seed layer there is a 3-D random distribution of easy axis orientations similar to that of Stoner-Wohlfarth entities whereas for the sample grown on the NiCr seed layer there is a 2-D random distribution of easy axis. It is the tensioning of the cluster-cluster interactions with the easy axis orientation that is thought to give rise to the training effect and other phenomena in exchange bias.

The change in H_{ex} and $\langle T_b \rangle$ with element size was measured in 4$\times$4mm arrays of nanodots patterned through e-beam lithography and fabricated using the lift-off method. Following an initial decrease of 66% due to the patterning process, H_{ex} decreased from (105$\pm$5)Oe to (40$\pm$5)Oe with element size from 425 to 80nm. However whilst an initial decrease in $\langle T_b \rangle$ from (448$\pm$5)K to $\sim$405K occured due to the patterning process no significant change is seen with element size. This implies that the change in H_{ex} is due to a modification of the interface i.e. non-planar deposition as a result of depositing the film through a mask.

Contents

List of Figures

List of Tables

Acknowledgments

For a 25 year old 5 years is alot of time to spend in one place so either they must be insane or enjoy what they do. Either way it is the people around you who make help to make it happen. Of these I would like to thank my colleagues from over the years. Both Jessada and Alejandro made my introduction to post-graduate study enjoyable and they have both been missed. However new people have come into the group who have helped to make it the best, in my opinion, it has ever been. For what can only be described as raw insanity Kelvin, Teo and Ioan always provide quality entertainment. As for those who have been here nearly as long as me both Ben and Chris have been an enjoyable and helpful pair, particularly for free sweets and an easy target for a prank. For those who have just started; Will, John and Jason you have a frustrating but wonderful time ahead of you and I am sure you will make the most of it.

I cannot fail to mention my supervisors as well. Both Gonzalo and Atsufumi have both been a great help with my work and a lot of fun and hope that in the future I will be in a position to continue to work with them. I would also like to thank Susan who has always been a happy face and a great chat, I do miss having you actually in the office. Finally without Kevin I would just have a 2:2 degree in physics and not much else. The opportunity and education over the years has most certainly been worth the mental trauma and I can only hope that I have done enough to have made the risk of letting me stay worthwhile.

Then of course I would like to thank Juliet for giving me a reason to not just sit around and play video games all day.

Declaration

I declare that the work presented in this thesis is based purely on my own research, unless otherwise stated, and has not been submitted for a degree in either this or any other university.

Publications

R. Carpenter, N. C. Cramp and K. O'Grady "Effect of Mn Interface Doping in Polycrystalline Exchange Bias Thin Films" *IEEE: Transactions on Magnetics*, vol. 48, no. 11, pp. 4315–4354, 2012

N. C. Cramp, R. Carpenter, K. O'Grady "Characterisation of Interface Spin Clusters in Exchange Bias Systems" *IEEE: Transactions on Magnetics*, vol. 48, no. 11, pp. 2881–2884, 2012

R. Carpenter, G. Vallejo-Fernandez, K. O'Grady "Interfacial Spin Cluster Effects in Exchange Bias Systems" *Journal of Applied Physics*, vol. 115, no.17D715, pp. 1–3, 2014

R. Carpenter, N. C. Cramp, G. Vallejo-Fernandez, K. O'Grady "Coercivity and Interfacial Spin Clusters in Exchange Bias Systems" *Journal of the Magnetics Society of Japan*, vol. 38, pp. 61–65, 2014

R. Carpenter, A. J. Vick, A. Hirohata, G. Vallejo-Fernandez, K. O'Grady "Effect of Grain Cutting in Exchange Biased Nanostructures" *Journal of Applied Physics*, vol. 115, no.17B905, pp. 1–3, 2014

T. F. Alhuwaymet, R. M. Abdullah, O. Whear, T. Huminiuc, R. Carpenter, M. El-Gomati, A. Hirohata "New Bandgap Measurement Technique for a Half-Metallic Ferromagnet" *IEEE: Transactions on Magnetics*, vol. 50, no. 11, pp. 1–4, 2014

T. F. Alhuwaymet, R. Carpenter, C. N. T. Yu, B. Kuerbanjiang, R. M. Abdullah, V. K. Lazarov, M. El-Gomati, A. Hirohata "Direct Band-Gap Measurement on Epitaxial $Co_2FeAl_{0.5}Si_{0.5}$ Heusler-Alloy Films" *Journal of Applied Physics*, vol. 117, no.17B131, pp. 1–3, 2015

Chapter 1

Introduction

Exchange bias was first discovered by Meiklejohn and Bean in 1956 in oxidised Co nanoparticles [1]. On cooling the Co/CoO nanoparticles in a strong field to 77K the hysteresis loop was seen to shift and was accompanied by an increase in the coercivity H_c. This behaviour was due to the ferromagnetic (F) Co core coupling to the antiferromagnetic (AF) CoO shell. As the AF does not see the applied field during measurement it provides a unidirectional anisotropy to the F which manifests as the shift in the hysteresis loop H_{ex}. Exchange bias has since been observed across a large range of materials and systems [1–6] however initially it was of fundamental interest alone.

With the discovery of Giant Magneto Resistance (GMR) in 1988 by Grünberg and Fert [7] and its application in the read head of a Hard Disk Drive (HDD) in 1998 [8] exchange bias became of technological interest due to its use in the pinning of the reference F layer. A rapid decrease in the lateral dimensions and layer thicknesses of the read head was required in order to match the extreme increase in areal density which drove an equal development of the materials and models of exchange bias. The importance of read head design can be seen in figure 1.1. This graph shows the increase in the areal density of HDDs with the key read head developments labelled.

Before the development of readily available computing power the models of exchange bias were analytical and concerned solely with the F/AF interface [9–12]. Despite some limited success at predicting the loop shift these models were unable to calculate the increase in H_c, its behaviour with temperature or the training effect. Following the development of

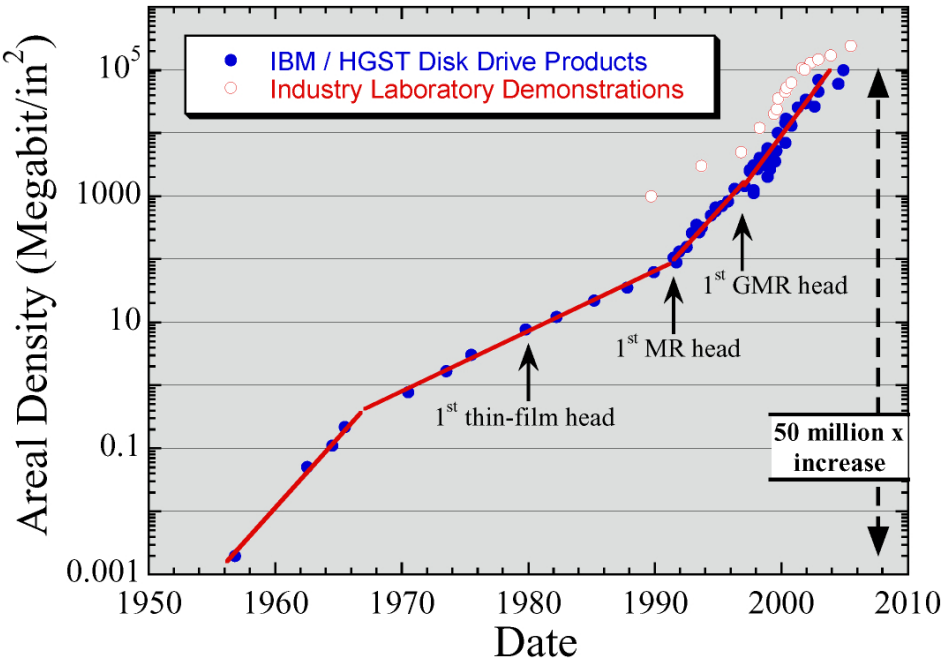

Figure 1.1: Increase in areal density in HDDs with key head developments labelled [8]

quantative computational models and the application of exchange bias in read heads there was a change in focus towards the order in the bulk of the AF [13] and, in polycrystalline films, the thermal stability of the AF grains [4]. The understanding provided by these models have allowed for the development of materials exibiting H_{ex} of >5kOe [14]. However a number of issues remain for the continued technological development of devices utilising exchange bias.

A schematic diagram of the layer structure in a Magnetic Tunnel Junction (MTJ) is shown in figure 1.2 a). This structure can be broken up into different functional parts: Capping layers (grey), Magnetic layers (green/red) and Seed layers (orange/white). In longitudinal media the read head lies in-plane with the surface of the disk. However with the development of perpendicular media the read head needed to be placed perpendicular to the plane of the disk. Therefore the total thickness of the read head is important and is one of the factors that defines the measurable bit size. As can be seen the portion of the MTJ that is the pinned layer takes up 16.4nm of the stack of which 10nm is the AF $IrMn_3$. Therefore the clear focus for thinning of the stack would be the AF layer, however this thickness is required to ensure thermal stability of the pinned/reference layers at operating

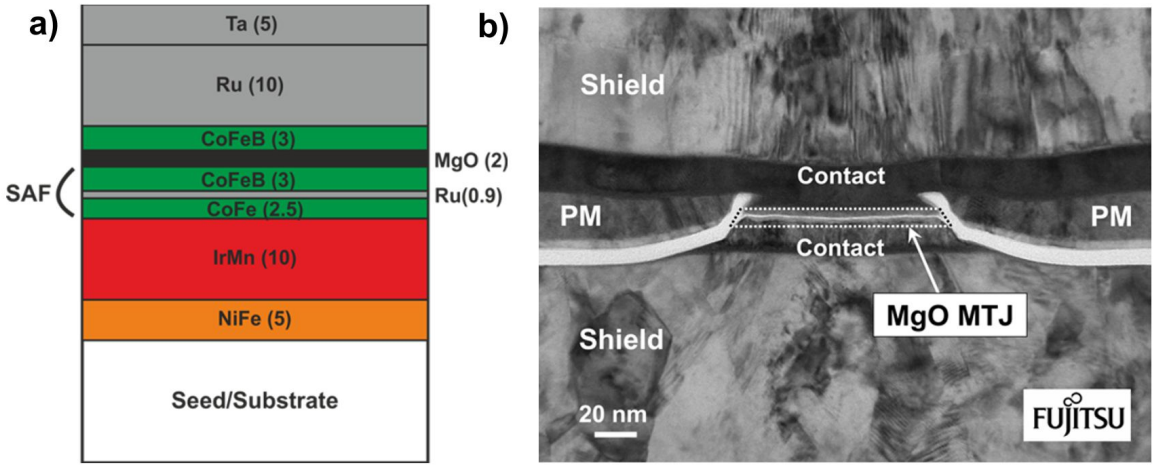

Figure 1.2: a) Schematic diagram of the typical layer structure of a MTJ in 2012 [15] where thicknesses are in nm and b) a cross-section TEM image of the air bearing surface of a MTJ for a read head [16].

temperatures of 70°C. Another focus for decreasing the stack thickness would be thinning of the seed layers as these can be up to 30-50nm thick. However these are required to produce the (111) texture in the $IrMn_3$ that gives the highest loop shifts and AF anisotropy and furthermore act as the bottom in-track shield [17]. Therefore a greater understanding of exchange bias could allow for thinning of the AF. Indeed the understanding provided by the York Model of exchange bias has allowed for optimisation of the granular structure of the AF layer decreasing the required thickness of the layer to 6-7nm [4].

However thermal stability of the AF is not the only concern in a MTJ. To obtain ideal Tunneling Magneto Resistance (TMR) ratios the MgO tunnel barrier must crystallise (001) in-plane. However crystallisation of NaCl-type (001) MgO is not possible on the face centered cubic (FCC) (111) textured AF/Synthetic Antiferromagnet (SAF) structure. This is due to a mismatch in the structural symmetry which for the MgO is 4-fold and the AF/SAF is 3-fold [16]. Furthermore crystallisation of the MgO tunnel barrier improves with increased annealing temperatures up to 500°C whilst layer diffusion in the SAF and AF are observed at temperatures above 300°C. Although a number of approaches to overcome these issues have been developed MgO crystallisation could be improved with a (100) textured exchange biased system. However this would require an understanding of the AF

spin structure and F/AF interface both of which are lacking.

Another control of the bit size in a HDD are the lateral dimensions of the read head. These are fabricated through a process of patterning the deposited film and Ar ion etching. A decrease in H_{ex} and the blocking temperature T_b is known to occur in elements $<$100nm in diameter [18–22]. Modern read heads have lateral dimensions $<$50nm and so degradation of the pinned layer will occur. Figure 1.2 b) shows a cross-section TEM image of the air bearing surface of a TMR-read head. As can be seen the read head is a trapezoid with the free layer at the narrower top and the SAF/AF on the wider bottom. This design allows for the lateral dimensions of the pinned layer/AF to be greater than that of the free layer. This relaxes the lateral restrictions on the AF layer limiting the damage due to patterning. However this is not the only concern as recent work has shown that significant Ar-ion and material implantation at the F/AF interface occurs during the etching process [23]. Furthermore there is evidence that secondary grain growth can occur during etching which could impact the granular structure in the AF and therefore the magnetic properties of the system [24].

The use of exchange bias to pin the fixed layer in MTJs has been a significant barrier in decreasing the read head size. Progress has been made in the development of exchange biased materials for application however the theoretical models of exchange bias are still lacking. The development of the York Model of exchange bias and the associated York Protocols has allowed for controlled, repeatable experiments and provided an understanding of the contribution of the bulk AF grains to H_{ex} and T_b [4]. These controlled measurements have provided the tools to precisely probe the interface however despite this an understanding of the behaviour of the F/AF interface is still lacking.

In this study two of the above mentioned issues of exchange bias will be tackled. The first is the fundamental issue with the mechanisms of the F/AF interface. Building on previous work of the group the effect of the (111) texture in $IrMn_3$ on the magnetisation reversal hasl been studied in detail [17]. This has been further explored in the setting field H_{set} dependence of H_{ex} [25, 26] and the training effect [27]. Secondly the effect of sub-500nm patterning on H_{ex} and the distribution of T_b will be carried out. The results will then be compared to a modification of the York Model which assumes the change in H_{ex} and T_b with element size to be due to grain cutting at the edge of the structure [28, 29]. A preliminary comparison between the fabrication methods of lift-off and etching through

a hard mask will also be carried out.

Chapter 2

Magnetic Thin Films

2.1 Fundamentals of Magnetism

The study of magnetic thin films is vital for modern technologies e.g. the Hard Disk Drive and Magnetic Random Access Memory. In the state of the art the thicknesses of layers in such films can be as low as 0.3nm with lateral dimensions of $<$50nm [30–32] bringing the study into the realm of atomic engineering. Although the basic mechanisms of magnetism are understood depending on the scale and application, the combination of these can give a wide variety of behaviour. In the interest of brevity only those mechanisms involved in granular F and metallic AF films will be considered in detail.

Before any further discussion there are three points of importance. Firstly for all future equations and results the c.g.s. unit system has been used due to its application in the magnetic recording industry. This is despite some movement towards the usage of SI units in areas of academia. A detailed discussion of units in magnetism is given in the text by Jiles [33]. Secondly where possible all errors on numerical results in graphs have been calculated with methods based on the standard Gaussian error techniques. With regard to data taken from books or literature if no error is quoted then it is not known. In keeping with group policy the source text used for fundamentals of magnetism is that of Cullity and Graham [34]. As such in the following section this is the key reference for any information given unless otherwise stated. Finally the group has a large library of diagrams that have been produced over the years. Any that have been used have not been referenced directly.

2.2 The Exchange Interactions

In order to explain the self ordering of Ferromagnetic (F) materials Weiss proposed the concept that a material will feel from itself a molecular field H_m given by

$$\underline{H}_m = \gamma_m \underline{M} \tag{2.1}$$

where M is the magnetisation of the sample and γ_m is the molecular field constant. From this equation it is clear that the phenomenon involved is cooperative where with greater ordering of the spins the aligning force felt by any independent spin is larger. This effect is clearly not entirely magnetic as the fields involved are typically three orders of magnitude too large e.g. in iron at room temperature H_m is found to be 6.9×10^6Oe whilst the demagnetising field H_d is 7200Oe.

It wasn't until the advent of quantum mechanics that Heisenberg showed that H_m was due to inter-atomic exchange forces. In the case of two atoms i and j with spin angular momentum $S_i h/2\pi$ and $S_j h/2\pi$ the exchange energy E_{ex} between them is given by

$$E_{ex} = -2J_{ex}\underline{S}_i\underline{S}_j = -2J_{ex}S_iS_j cos\theta_{ij} \tag{2.2}$$

where J_{ex} is the exchange integral and θ_{ij} is the angle between the spins. It is the sign of J_{ex} that controls the ordering of the material. If J_{ex} is positive then E_{ex} is at a minimum when the spins are parallel $(cos\theta_{ij} = 1)$ and a maximum when antiparallel $(cos\theta_{ij} = -1)$. If J_{ex} is negative then the lowest energy state occurs when the spins are antiparallel. Equation 2.2 is a simplification in that it only applies to a two atom system and so must be summed over all atom pairs in a given crystal. This situation can be simplified by only considering nearest-neighbour pairs due to the short range of the exchange force. This gives a Hamiltonian of the form

$$\langle H \rangle = -2J_{ex}\Sigma\underline{S}_i\underline{S}_j \tag{2.3}$$

This theory allows for the rationalisation of the appearence of ferromagnetism, antiferromagnetism and ferrimagnetism in some materials and not others. The graph in figure 2.1

is known as the Bethe-Slater curve which shows the variation of the sign of J_{ex} for the ratio r_A/r_{3d} where r_A is the atomic radius and r_{3d} is the radius of the 3d electron shell. If two atoms are brought closer together without any change in r_{3d} the ratio r_A/r_{3d} will decrease. When the ratio is large a weak positive J_{ex} results. As the atoms are brought closer together the positive exchange interaction which favours parallel spins becomes stronger. As the interatomic distance approaches that of $2r_{3d}$ J_{ex} decreases to zero and eventually turns negative favouring an antiparallel alignment leading to antiferromagnetism.

The Bethe-Slater Curve in 2.1 can be applied to different elements if r_A/r_{3d} is compared for the known atomic diameters and shell radii. This correctly seperates the F 3d transition metals (Fe, Co and Ni) from the lighter AF metals Mn and Cr (T_N=95K and 310K respectively). When J_{ex} is positive its magnitude is proportional to that of the Curie temperature T_C. This is because the exchange force holding the spins in parallel alignment is strong and requires a large amount of thermal energy to be overcome. This matches the prediction of the Bethe-Slater curve however difficulties arise when attempting to measure both the sign and magnitude of J_{ex} [35].

This coupling due to the exchange interaction is what is referred to as direct exchange. However direct exchange cannot explain the ordering that occurs across non-magnetic or frustrated boundaries. An important piece of evidence for a long range interaction is seen in

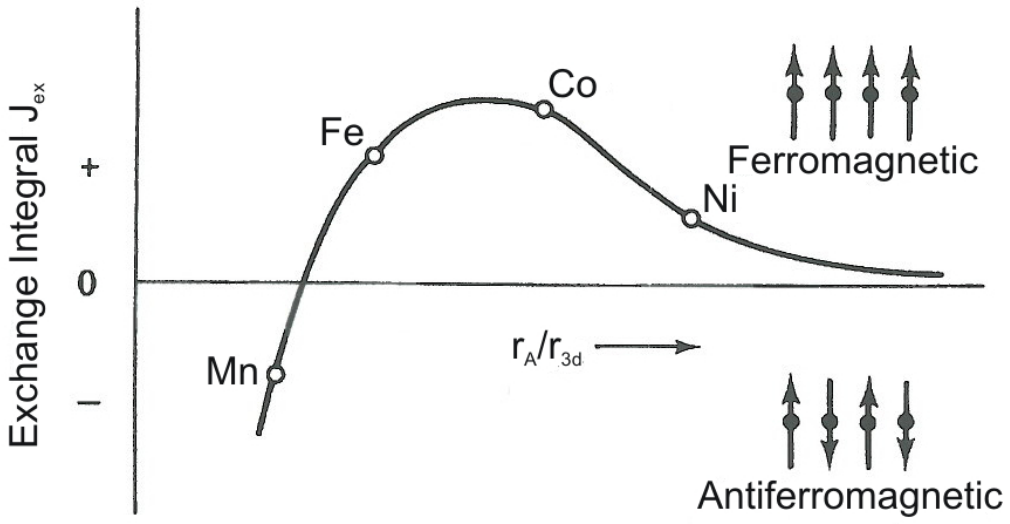

Figure 2.1: Bethe-Slater curve schematic [34].

the variation in coupling between Fe layers seperated by a Cr spacer of increasing thickness as shown in figure 2.2. In the work of Parkin et al. [36] it was found that the coupling across a non-magnetic boundary oscillated from favouring a parallel to antiparallel alignment depending on the spacer thickness with a periodicity of 18-21Å.

This indirect exchange occurs due to polarisation of the conduction electrons by the unpaired bound electrons. These polarised conduction electrons can then exchange this polarisation to the bound electrons of the neighbouring atom. The sign of this coupling is controlled by the spacing between these atoms as observed in figure 2.2.

The oscillation of the sign of the coupling is explained by looking at the behaviour of the up and down spins in the spacer layer. In the case of ferromagnetic alignment there are empty states present in the e.g. up spin band for the spacer and both F layers. Therefore

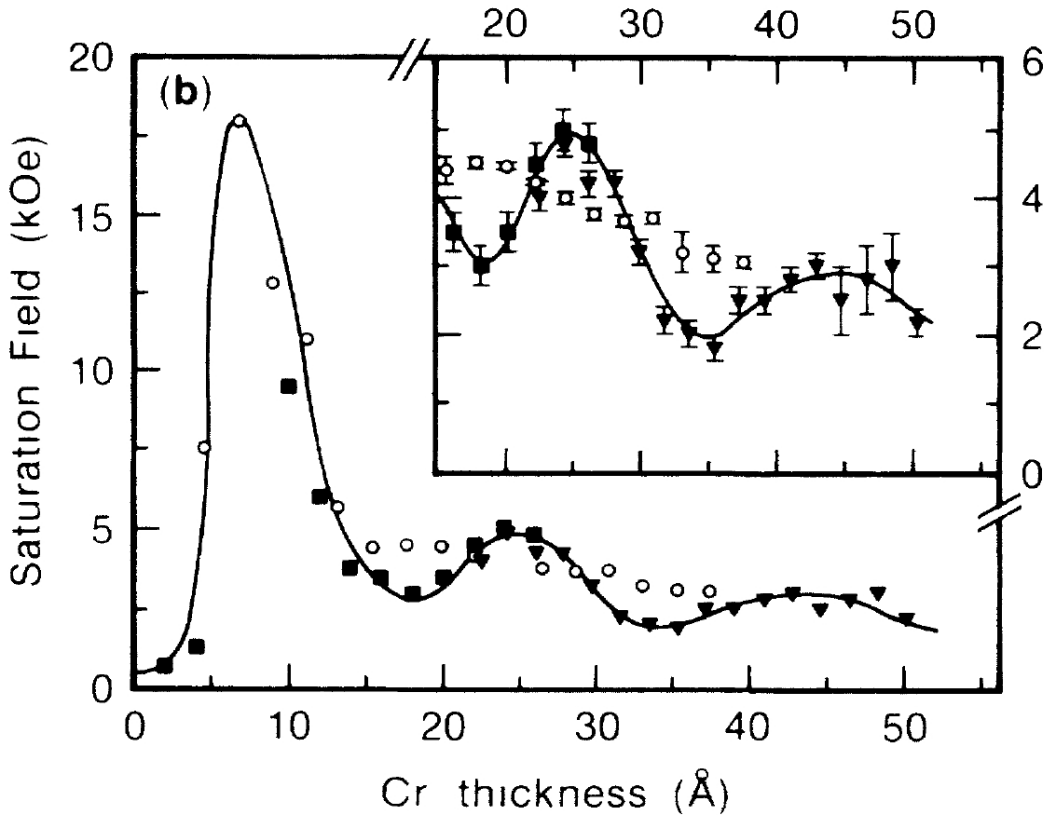

Figure 2.2: Change in saturation field as measured at 4.5K with Cr layer thickness in Fe(20Å/Cr(t_{Cr}) multilayers [36].

the up spin electrons are free to move throughout the stack whilst the down spin electrons must remain confined within the spacer layer in an analogy to a quantum well. In the case of antiferromagnetic alignment the up spin electrons will be free to travel through one of the F layers and the spacer stopping at the interface with the oppositely magnetised F layer with the down spins doing the opposite. These two orientations have different energies which are dependent on the spacer thickness. Therefore as the thickness is varied a change in orientation will occur due to the competing energies. The oscillation of this occurs due to the quantised nature of the density of states which is also dependent on the spacer thickness [37].

This concept was developed initially by Ruderman, Kittel, Kasuya and Yosida (RKKY) in order to explain the presence of exchange coupling in the rare earth metals in which the unpaired, highly localised 4f electrons are ordered despite their wave functions not overlapping. It has since been expanded to explain the coupling in a large variety of systems and is known as the RKKY interaction. Depending on the system the oscillation in coupling can have a periodicity of anything from 1Å to multiple atomic layers.

In granular systems it is known that grains couple with their neighbours. Such an interaction is assumed to be due to RKKY coupling across the grain boundary. Despite there being no calculation from first principles showing this to be the case, the success of the associated models implies this to be correct. This assumption has been used for many systems i.e. recording media [38] which further validates the approach. In granular systems even a small variation in atomic spacing i.e. at a grain edge can lead to a change in the sign of the coupling from grain to grain. This is particularly the case for systems such as binary alloys where one of the atoms is non-magnetic.

2.2.1 Exchange Interactions in Antiferromagnetic Thin Films

The ordering in an AF material e.g. $IrMn_3$ or Cr is solely dictated by direct exchange. From the work of Slater, Stoner and Néel [39, 40] and as shown in the Bethe-Slater curve, the orientation of the exchange integral is dependent on the smallest distance between the magnetic shells. This is defined by the difference between the diameter of the 3d-band and the atomic separation. Whilst F behaviour is limited to distances of around 1.1-1.5Å the sign

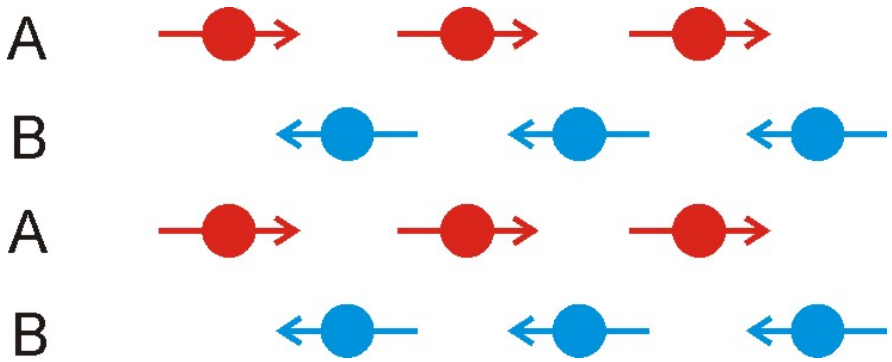

Figure 2.3: AF spin structure schematic showing A and B sublattices.

of J_{ex} changes at a spacing of less than 1.1Å leading to antiferromagnetic or ferrimagnetic ordering.

Although calculation of these interactions in a region is now possible, to obtain a conceptual understanding of the system the principles of the Wiess molecular field may be used. For ferrimagnets and antiferromagnets the interaction felt by an ion A can be broken into two components; those due to nearest neighbour A ions and those due to nearest neighbour B ions. As shown in the schematic in figure 2.3 the interaction between the A ions leads to parallel ordering with the same occuring between the B ions. However between the A and B planes the interaction leads to an antiparallel alignment. In order to obtain an AF material the number of A and B ions within a lattice must be the same otherwise the material displays ferrimagnetic behaviour. Therefore an understanding of the spin structure within the crystal lattice of an AF material which may only be obtained via neutron diffraction is required for any meaningful attempts at modelling the system.

The spin structure in AF materials is a relatively contentious area due to the difficulty of measuring the magnetic properties of an AF. In the case of $IrMn_3$ it is thought that there are two AF crystallographic phases; the chemically disordered γ-$IrMn_3$ and the ordered $L1_2$-$IrMn_3$ [41, 42]. These structures are shown schematically in figure 2.4 a) along with the expected spin structure. Whilst there is no experimental evidence of the spin structure in γ-$IrMn_3$ neutron scattering experiments in large single crystals [42] and films of thickness $>$100nm [41] of $L1_2$-$IrMn_3$ indicate that it is trigonal. This is known as the T1 structure in which the maganese moments are parallel to the $\{111\}$ planes and aligned along the $<112>$ directions. However in the case of the work done in this thesis the composition and

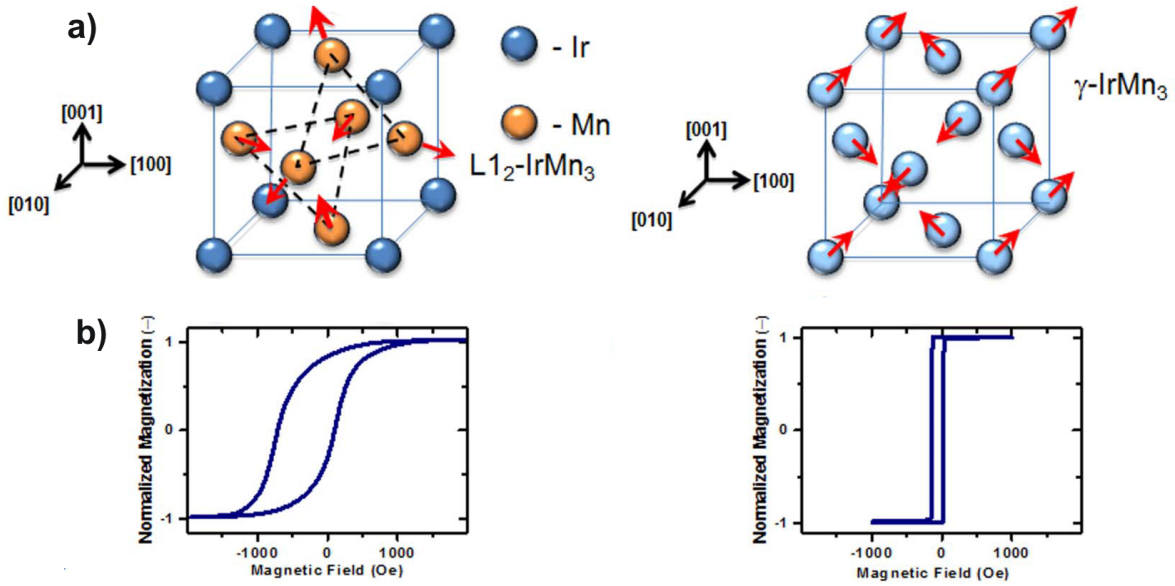

Figure 2.4: The a) schematics of the two predicted spin structures in $IrMn_3$ and b) measured hysteresis loops obtained when couple to a layer of iron. [41]

therefore spin structure can be brought into some question. The work of Tsunoda et al. shows that a peak in exchange bias is observed within the composition range 22-32% iridium as mentioned above [43]. However for the deposition system used in this work the peak in H_{ex} is obtained at a composition of 13-22% iridium which is indicative of $IrMn_4$ [44]. Despite this, the crystallography of these samples as discussed in chapter 6 show the (111) peak which implies the deposition of $L1_2$ phase $IrMn_3$.

One of the key differences between these structures is the value of T_N. However reports of the values vary where T_N= 700-780K for γ-$IrMn_3$ and T_N=960-1000K for $L1_2$-$IrMn_3$ [41–43]. This is also accompanied by an increase in exchange bias and the blocking temperature T_b when the AF is coupled to a F. An example of the difference as observed magnetically is shown in figure 2.4 b) where in the ordered phase H_{ex}=310Oe and H_c=410Oe and in the disordered phase H_{ex}=60Oe and H_c=90Oe [41]. From early neutron diffraction studies on single crystals of IrMn alloys a composition of 22-32% iridium required a temperature of 600-700K to form the ordered $L1_2$ phase. Consquent studies have found that through use of seed layers the temperature required for the ordered phase can be significantly lowered for thin films e.g. for a copper seed a deposition temperature of 440K will give the $L1_2$

phase [43].

There are two more forms of AF interaction that deserve mention. The first occurs in what is known as a SAF. This is an artificial system where multiple layers 1-2 atoms thick of a F material i.e. cobalt are deposited with a non-magnetic separating layer. This non-magnetic layer is of a sufficient thickness to force anti-parallel alignment of the F layers due to indirect exchange. The second occurs in oxides of F materials i.e. CoO. In these oxides the distance between the moment carrying atoms is too great for the ordering to be due to direct exchange. This shows there is some form of indirect exchange occuring. When the oxygen atom is bound to a cobalt atom with an up spin it is the oxygen's down spin electron that is shared. When a second cobalt atom is bound to the oxygen atom it is forced to be down spin creating an antiparallel alignment. This form of coupling is known as super exchange and it is with these oxides that exchange bias was first observed [1].

2.2.2 Exchange Interactions in F/AF Thin Films

In order to make a succesful model of exchange bias the interactions that occur between the F and AF layers must be understood. This requires a definition of the system that is to be used, in this work and all applications the system is that of a polycrystalline thin film. Following the simple model of Meiklejohn and Bean [1] where the interface is perfectly flat and compensated there will be only two interactions to consider. The first is the direct exchange between the AF and F grains with the second being the indirect exchange in the F layer known as intergranular coupling. There will be no intergranular coupling between the AF grains as the boundaries will be highly disordered i.e. an iridium vs. mangenese terminated edge. This assumption is proven by the ability of the York Model of Exchange

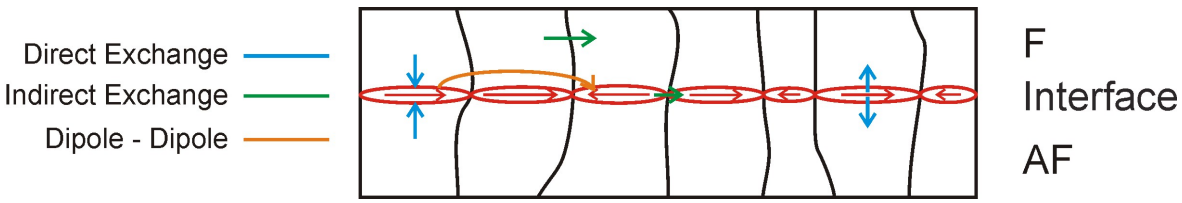

Figure 2.5: Schematic of exchange interactions in a F/AF bilayer.

Bias to fit the granular dependence of H_{ex} to the grain size distribution as explained in detail in chapter 3 [4].

This simple model has since been shown to not fully describe the system. At the interface the magnetic ordering will be highly frustrated due to competition between the ordering from the F and AF layers. As will be described in detail in chapter 3 this frustration of the spins at the interface leads them to behave as an entity independent from that of the bulk layers where they form clusters which behave analagous to a spin glass/fine particle system [45, 46]. Such a system will behave like superparamagnetic particles the ordering of which is described by the Langevin function $L(a_L)$

$$L(a_L) = \frac{a_L}{3} - \frac{a_L^3}{45} + \frac{2a_L^5}{945} - \cdots \tag{2.4}$$

where a_L=$\mu_m H/k_B T$. The field H felt by these clusters will be defined by a number of interactions: AF-cluster, F-cluster, and cluster-cluster. The cluster-cluster interaction is particularly unclear however it is expected that this will be some combination of indirect exchange and dipole-dipole coupling. This situation is shown schematically in figure 2.5 with the interactions labelled. Evidence for these interactions can be found in the reversal mechanics of the films which will be discussed further in sections 2.5 and 6.2. However as can be seen, this is a multi-body system and as such seperating out the interactions is a difficult task.

2.3 Anisotropies in Magnetic Materials

A key feature of ordered magnetic materials i.e. ferro, ferri and antiferromagnetic substances is magnetic anisotropy. This simply means that the magnetic properties of a material will depend on the direction in which they are measured. There are two main origins of anisotropy; magnetocrystalline and shape. The dominance of the anisotropies is system dependent and dictates the shape of the magnetisation curve and as such an understanding of both is required. There are a number of other 'anisotropies' that are induced by external effects such as stress, plastic deformation and irradiation. A full description of these will not be made as they are external modifications to either the magnetocrystalline or shape anisotropies

i.e. stress applied to a single crystal will change the lattice constant along a single direction inducing a change in the magnetocrystalline anisotropy.

2.3.1 Magnetocrystalline Anisotropy

Magnetocrystalline anisotropy is intrinsic to a given material and is dependent on the crystal structure. If a disk is cut from a single crystal with a cubic structure along the $\{110\}$ plane then the directions $\langle 100\rangle$, $\langle 110\rangle$ and $\langle 111\rangle$ will be diameters. If this disk is measured along these directions then information about the three crystallographic directions may be obtained. The data for such a measurement is shown in figure 2.6a) for iron which has a body centered cubic (BCC) structure. When measured along the $\langle 100\rangle$ direction saturation occurs at $\sim$100Oe and is known as the easy axis. In the $\langle 111\rangle$ direction saturation does not occur until $\sim$500Oe and is known as the hard axis.

The origin of the magnetocrystalline anisotropy is the so called 'crystal field'. This field arises because when atoms are bonded the angular moment component of the electrons is fixed. Through the spin-orbit interaction this also fixes the spin component of the electrons. As such during the magnetisation process the energy required is equal to that of the spin-orbit interaction. This implies that in a crystal where M_s points from the easy axis energy must be stored. This crystal anisotropy energy E_A can be expressed in terms of a series

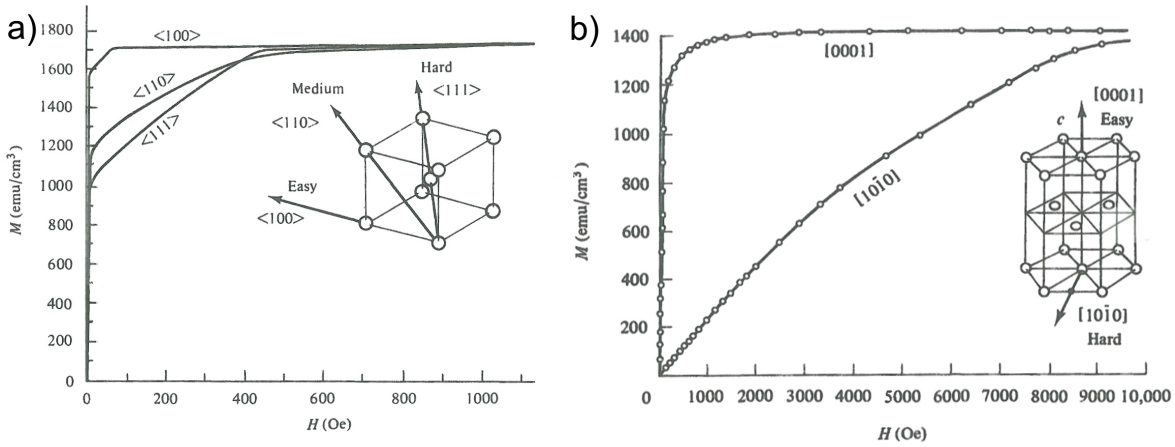

Figure 2.6: Magnetisation curves for single crystal a) iron and b) cobalt [34].

expansion of the direction cosines $\alpha_1, \alpha_2, \alpha_3$ of M_s with respect to the crystal axes. This gives

$$E_A = K_0 + K_1(\alpha_1^2\alpha_2^2 + \alpha_2^2\alpha_3^2 + \alpha_3^2\alpha_1^2) + K_2(\alpha_1^2\alpha_2^2\alpha_3^2) + \cdots \tag{2.5}$$

where K_0, K_1,K_2,... are anisotropy constants for a given material at a known temperature and measured in ergs/cc. Higher order terms are generally neglected and K_2 is often negligible. The value of K_0 is independent of angle and so it is only K_1 that is of interest. In this case it is the sign of K_1 that gives the direction of the easy axis.

The situation is slightly different when the crystal structure is hexagonal close-packed as is shown in figure 2.6b) for cobalt. In the case of cobalt there is a uniaxial anisotropy where the easy direction lies along the c axis with the basal plane found to be equally hard in all directions. This gives an equation for E_A in terms of the angle θ_U between the M_s vector and the c axis as given by

$$E_A = K_0 + K_1 sin^2\theta_U + K_2 sin^4\theta_U + \cdots \tag{2.6}$$

In this case it is the sign of both K_1 and K_2 that give the easy direction. When both are positive the crystal has a uniaxial anisotropy with the easy direction along the c-axis and when negative the easy direction lies within the basal plane. A more complicated situation arises when K_1 and K_2 are of opposite sign. In such a case an easy cone of magnetisation may be obtained.

The magnetocrystalline anisotropy force can be expressed in terms of a magnetic field attempting to hold the magnetisation parallel to the axis. The field is parallel to the easy direction and of a magnitude so that at small angles it exerts a similar torque on M_s to that of the crystal anisotropy. This field is called the anisotropy field and is given the symbol H_K. The torque due to the magnetocystalline anisotropy is dependent on the crystal structure, anisotropy constants, easy axis direction and occasionally the crystallographic plane in which M_s rotates away from the easy axis.

The measurement of the anisotropy constant is difficult where often the value is only known to one or two significant figures with disagreement between different investigators.

This is due to difficulty in seperating out contributions due to shape as well as the other induced anisotropies i.e. stress. In the case of AF materials this is an even more difficult task due to there being no measurable magnetisation. As such the AF anisotropy K_{AF} is often measured via its effect on a neighbouring material i.e. exchange bias [47] and ferromagnetic resonance [48].

2.3.2 The Demagnetising Field and Shape Anisotropy

Shape anisotropy is extrinsic in that its origin is in the demagnetising field H_d generated by the sample. In order to understand the shape anisotropy a knowledge of H_d is required. If a bar sample is magnetised by applying a field from left to right and then removing it a north pole will be formed at the right hand end with a south being formed at the left hand end. The lines of flux radiate out from the north pole and end at the south creating a field both in and outside the magnet. This field acts from north to south tending towards demagnetisation of the magnet. An example of this in an ellipsoid magnet is shown in figure 2.7. The field H_d opposes and is proportional to that of the magnetisation M that creates it as given by

$$\underline{H_d} = -N_d \underline{M} \tag{2.7}$$

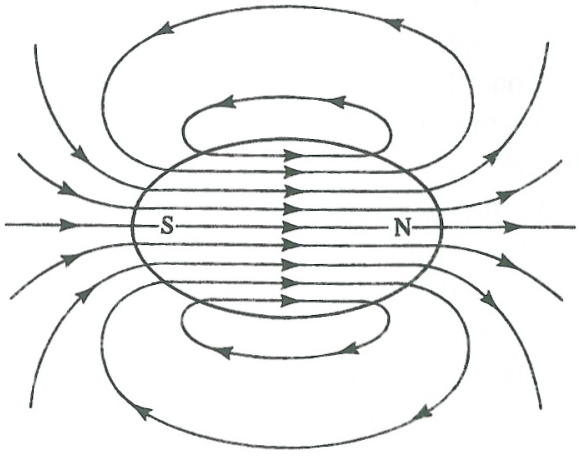

Figure 2.7: Schematic of the H field in an ellipsoid magnet at zero field [34].

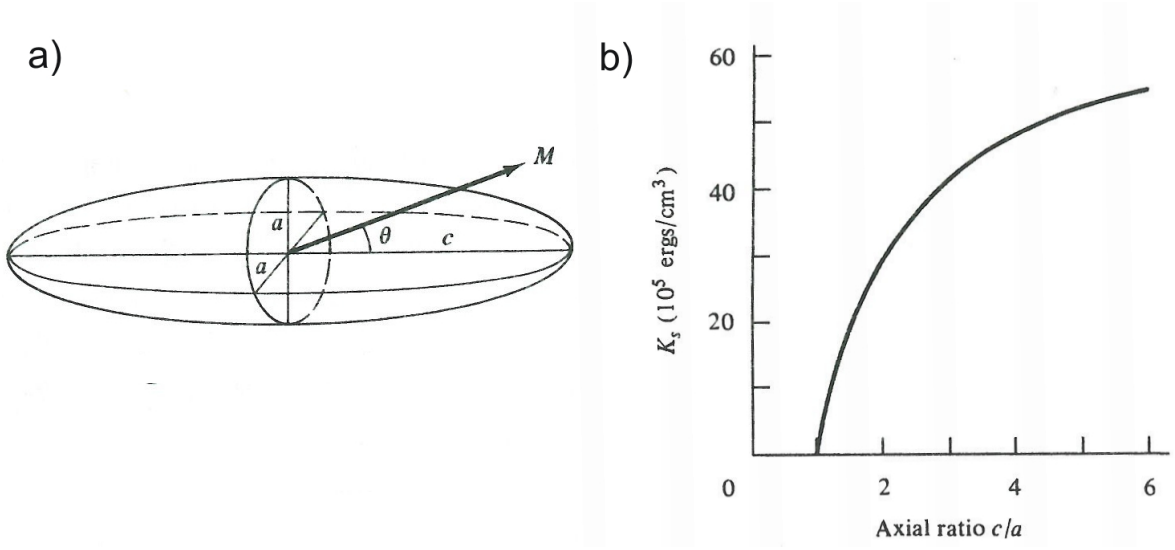

Figure 2.8: A a) schematic of a prolate spheroid with b) graph showing the change in shape anisotropy with axial ratio for Co (M_s=1422emu/cc) [34].

where N_d is known as the demagnetising factor which depends on the shape of the body. In the case of a prolate spheroid as shown in figure 2.8a) the shape anisotropy constant K_{sh} is given as

$$K_{sh} = \frac{1}{2}(N_a - N_c)M_s^2 \tag{2.8}$$

where N_a and N_c are the demagnetising factors along the semi-major and semi-minor axes respectively. An example of the variation in K_{sh} with axial ratio c/a for cobalt is shown in figure 2.8 b). At an axial ratio of 3.5 K_{sh}=4.5$\times 10^6$ ergs/cc which is equivalent to that of K_1 for cobalt. In the case of materials with a lower magnetocrystalline anisotropy such as Fe_3O_4 and CoFe above an axial ratio of 1.4 shape anisotropy will dominate [49]. As such shape anisotropy is not a negligible contribution and so when measuring the magnetocrystalline anisotropy it must be removed or taken into account.

In polycrystalline F films the grains are strongly coupled and almost 100% dense. Even if the grains are not fully equiaxed free poles cannot form and so shape anisotropy does not apply. However in patterned films such as those studied in this work interaction between dots can occur via the demagnetising field. Furthermore shape anisotropy will become more

of an issue as the size of the dots decreases to be equivalent to the thickness of the films. Finally AF materials will have no shape anisotropy due to them having no net magnetisation.

2.4 Domain Structures

Although the concept of exchange forces helped to explain the appearance of magnetism across the different metals and alloys it could not explain why, for instance, it was easy to obtain a chunk of iron in the demagnetised state. Weiss proposed that a F material in a demagnetised state is in fact broken up into spontaneously magnetised regions called domains. Each of these domains would be at saturation however oriented in such a way that the net magnetisation of the sample is zero. The magnetisation process of a F material then becomes a process of converting a multi-domain object into that of a single domain as shown in figure 2.9.

The transition from one domain to the next is known as a domain wall and it is the formation, movement and destruction of these which controls the reversal of a F material.

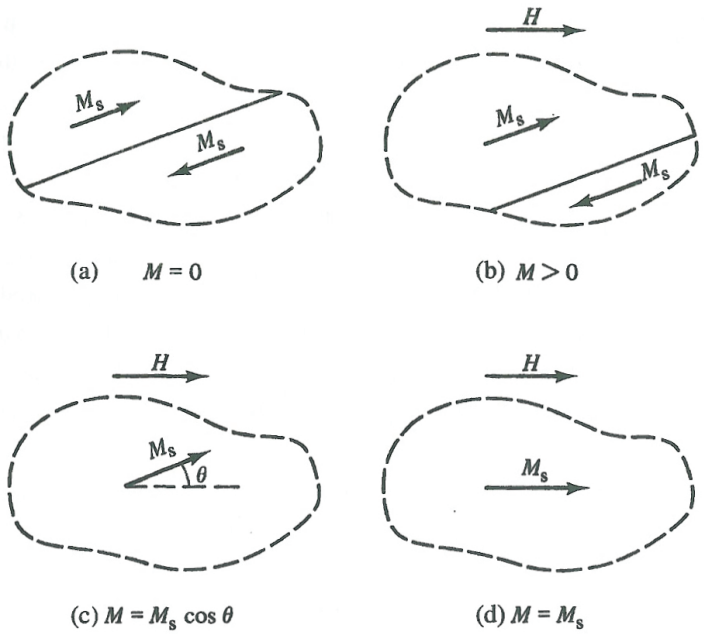

Figure 2.9: Change in domain 'structure' during the magnetisation process in a ferromagnet [34].

This mechanism is shown schematically in figure 2.9 where a field is applied at some angle θ to the two oppositely magnetised domains. As the magnitude of the field is increased the domain wall moves through the sample until it contains a single domain. With subsequently higher fields the moment of the domain rotates to align with the field reaching saturation. This is a simplification of the reversal process which will be described in greater detail in chapter 2.5.2.

The formation of domains is an attempt of the system to minimise the large magnetostatic energy that is due to the large H_d present in a single domain entity. An example of this is shown in figure 2.10. The energy per unit volume of a single-domain crystal is given by equation 2.8. For the crystal shown in figure 2.10 the energy per unit area of the top surface is given by

$$E_{ms} = \frac{2}{3}\pi M_s^2 D_T \tag{2.9}$$

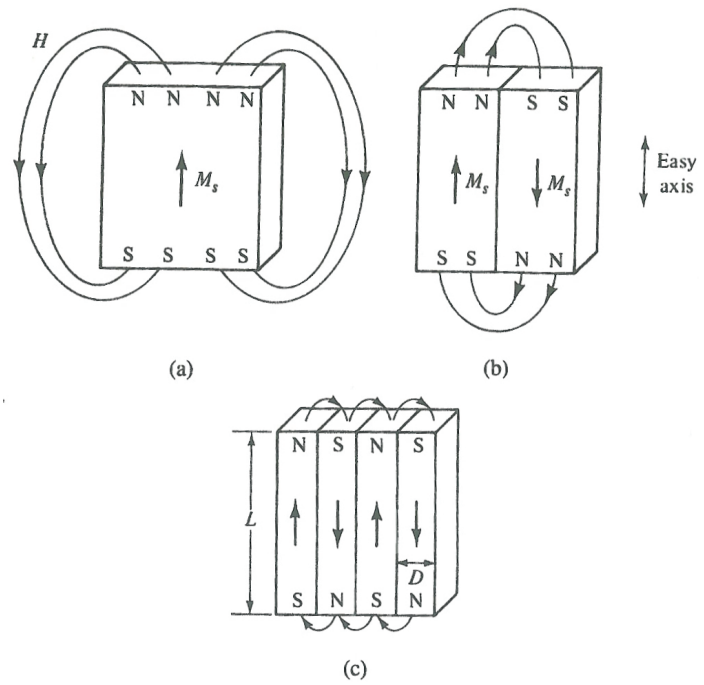

Figure 2.10: Division of a single crystal into domains where only the external field is shown [34].

where D_T is the thickness of the domain. The calculation of this is non-trivial for multi-domain crystals. Furthermore the division to even smaller domains is limited by the exchange energy required for the formation of a domain wall. This energy is given by equation 2.2 however in order to lower the energy of the domain wall the change in spin direction occurs over a number of atoms requiring a continuum expression

$$E_{ex} = 2A_{es}cos\Big(\frac{d\theta}{dx}\Big) \tag{2.10}$$

where A_{es}=$(n_A J_{ex} S_i S_j / L_p)$ which is known as the exchange stiffness. In this the n_A is the number of atoms per unit cell and L_p is the lattice parameter. The energy cost of a wall is thus defined by its thickness. Again in order to minimise E_{ex} the domain wall will be as thick as possible. However the magnetocrystalline anisotropy favours a thinner wall in order to limit the number of atoms oriented away from the easy axis.

As can be seen the size of a domain and the width of the walls is dictated by the exchange and magnetostatic energies as well as the magnetocrystalline anisotropy. This gives rise to complex domain patterns. This is also the case in polycrystalline thin films due to direct exchange between grains of varying easy axis orientation [50]. Furthermore in the case of exchange biased materials an extra anisotropy is added due to coupling with the AF which will also vary in easy axis orientation separately to that of the F layer.

2.4.1 Domains in an Antiferromagnet

In a perfect AF crystal domains will be unable to form due to a lack of a net magnetisation and therefore a magnetostatic energy which is required for the formation of domains. There are however a number of models and some experimental evidence for the formation of AF domains in some materials. The first suggestion of the existence of AF domains was by that of Néel [40] where domains with separating walls form due to variations in the orientation of the magnetocrystalline anisotropy across the material. Néel proposed that the domain wall widths and energy would be comparable to that of a F material. However the fields required for the displacment of a domain wall and rotation of a domain would be $\sim$3 orders of magnitude larger than those required in a F material. In the work of Kouvel [51, 52] it was hypothesised that AF domains form in dilute AFs where the moment carrying atom

is only 5-30% of the material. In the case of these dilute AFs 'domains' form due to a variation in composition across the sample i.e. regions where the local composition leads to AF ordering which are seperated by areas which have F ordering. These 'domains' are therefore due to a variation in structure and will not vary with applied field.

The works of Kouvel and Néel were cited in the model of Malozemoff [11] where domain walls were said to form perpendicular to a F/AF interface due to a random field [53] generated by defects at the interface. In both works the domains formed are due to local variations in structures where the domains will be fixed. Multiple domains of these types are not feasible in the polycrystalline AF materials used in applications where grain diameters and layer thicknesses are $\sim$6nm. In the work of Chien and Shull et al. [54,55] domains were observed in a F/AF thin film. However in this case the domains formed in the AF are an 'imprint' of the F domain structure. On reversal it is only the F domain walls that move creating an exchange spring with the AF wall. Such a situation would only occur if the sample is set with the F not at saturation and so will not apply to the samples used in this study.

2.5 Magnetisation Reversal in Granular Films

The magnetisation process in an ordered magnetic material is difficult to predict as it is a prime example of a multi-body system. Not only do the above mechanisms interact with each other but as magnetism is a microscopic effect local variations can add to observable yet unpredictable pertubations to the ideal system. Despite this progress has been made in the development of models and experiments leading to an understanding of the different reversal processes. Of the many variations on a theme only two of the fundamental processes will be considered; domain wall reversal and coherent reversal which is otherwise known as Stoner-Wohlfarth theory.

2.5.1 Stoner-Wohlfarth Theory and Coherent Reversal

The most general system to consider is that of an isolated single domain particle where magnetisation reversal occurs through rotation. The model that describes the magnetisation

reversal process in such particles is known as Stoner-Wohlfarth theory. A schematic of such a particle with a field H applied at an angle α_h to the easy axis is shown in figure 2.11 a). When the field is applied to the particle at an angle α_h the total energy of the system E_T at $T= 0$ is given by a combination of the anisotropy energy E_A and the Zeeman energy E_Z

$$E_T = E_A + E_Z = V[K_U \cdot sin^2\theta - HM_S \cdot cos(\alpha_h - \theta_m)] \tag{2.11}$$

where θ_m is the angle between the magnetisation and the easy axis, K_U is the uniaxial anisotropy, M_s is the saturation magnetisation and V is the volume of the particle. By differentiating E_T with respect to θ_m the equilibrium position of M_s may be found and is given in the general case as

$$sin\theta_m cos\theta_m = h_n sin(\alpha_h - \theta m) = 0 \tag{2.12}$$

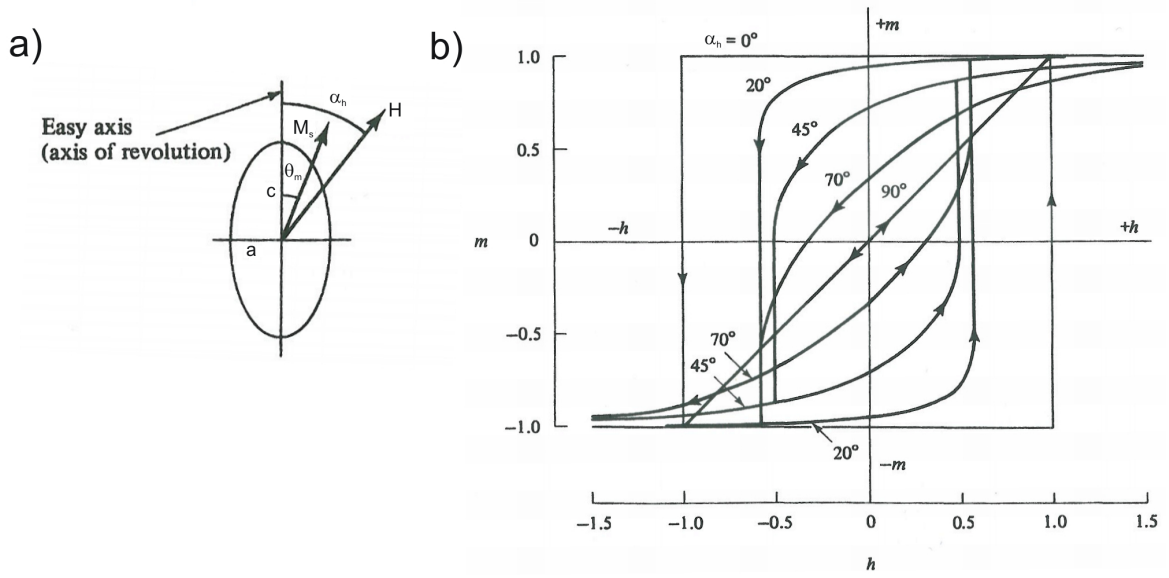

Figure 2.11: Schematics of a) the rotation of the magnetisation by an external field in a single domain elipsoid and b) hysteresis loops of said elipsoid at different angles of α_h [34].

where the component of the magnetisation in the field direction is given as

$$m_n = cos(\alpha_h - \theta m) \tag{2.13}$$

where h_n is the normalised field H/H_K and m_n is the normalised magnetisation M/M_s which are both equal to $H(M_s/2K_U)$. The evolution of m_n as a function of H at any angle of α_h can be calculated by the second derivative of E_T a full derivation of which can be found in Cullity and Graham [34]. The hysteresis loops obtained for a single domain particle at different α_h are shown in figure 2.11 b).

In the special case where $\alpha_h = 0$ and h_n is in opposition the magnetisation will not reverse until the anisotropy energy barrier, the origin of which will be described in chapter 2.6, can be overcome. When $\alpha_h \neq 0$ a torque is felt by the moment leading to a reduction in the energy barrier and consequently the coercivity H_c. This leads to the breaking up of the M/H loop into reversible and irreversible portions. The extremes are shown in 2.11 b) where $\alpha_h = 90$ and $\alpha_h = 0$ are completely reversible or irreversible processes respectively with a combination occuring for the intervening angles.

The process of coherent reversal in a polycrystalline film is that which assumes Stoner-Wohlfarth entities. In such a system a key requirement is that the particles must be non-interacting otherwise reversal via domain wall motion will occur. In coherent reversal the atomic moments must be parallel during the reversal process. In the case of exchange biased materials used in this study the AF grains are known to be non-interacting and therefore assumed to behave as Stoner-Wohlfarth entities, the mechanism of which is identical to ferromagnetic case.

2.5.2 Domain Wall Reversal

In exchange coupled or large grain polycrystalline films magnetisation reversal will occur via a process of domain wall nucleation, propogation and rotation which is shown schematically in figure 2.12 a). Assuming a perfect material at low fields rotation of magnetisation does not occur due to the low energy process of domain wall movement. On approach to saturation if there is any misalignment between the applied field and the easy axis a process of rotation will occur leading to a 'tail' to form.

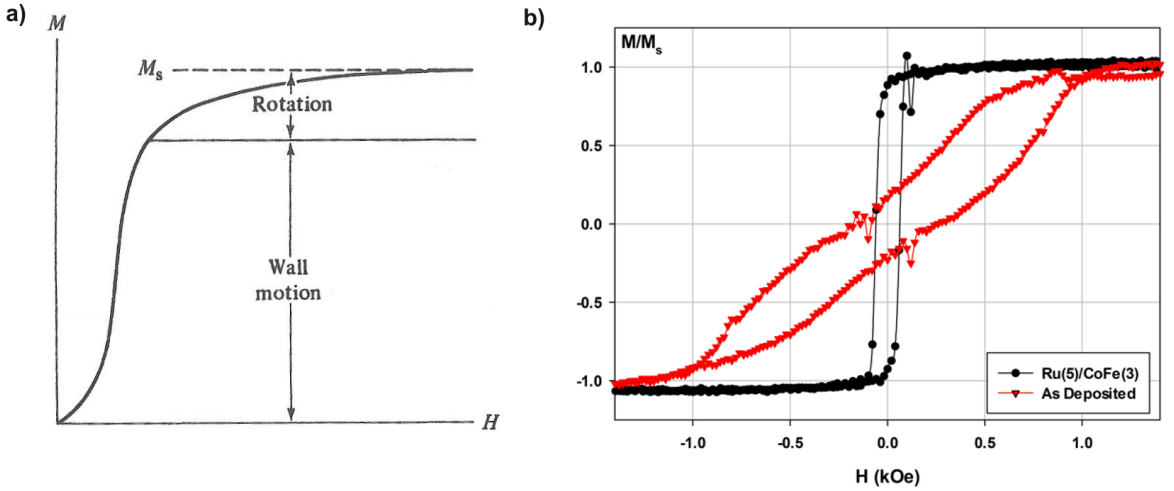

Figure 2.12: Graphs of a) the magnetisation process in an ideal material [34] and b) a comparison between thin films of structure Cu/CoFe and Cu/IrMn/CoFe [56].

In real materials inclusions will exist in the film i.e. defects, inclusions, stress or variations in local anisotropy. These lead to pinning of domain walls during reversal which gives skewing of the loop. Furthermore in the case of real polycrystalline materials there will be a distribution of easy axis across the distribution of grains. This will lead to a further skew in the loop representative of the distribution. Asperities and edge roughness i.e. in patterned structures can lead to formation of closure domains which leads to significantly higher saturation fields.

An example of the change in magnetic reversal with exchange bias is shown in figure 2.12 b). The black loop is an example of polycrystalline CoFe where the grains are exchange coupled and reverse via domain wall nucleation, propogation and closure. The red loop is an as deposited CoFe layer deposited on AF $IrMn_3$. As can be seen the reversal process is more similar to that of a distribtion of randomly oriented and isolated grains which is a reflection of the state of the underlying AF grains. These results will be discussed in detail in chapter 6. As it stands the reversal process in magnetic materials is a complex and difficult to model process. As can be seen exchange biased materials are exceedingly complex due to the summation of two interacting systems where one of the layers is near unmeasurable.

2.6 Thermal Activation and Time Dependence

In a uniaxial particle there are two stable states of minimum energy. In order to reverse the particle from the one state to the other it must pass through a state of maximum energy. The difference between the maximum and minimum energies is known as the energy barrier to reversal. A schematic of this situation is shown in figure 2.13.

Assuming the field is applied along the easy axis the total energy of a uniaxial particle as given in equation 2.11 can be used to find the minimum E_{min} and maximum E_{max} energies as given by

$$E_{min} = -HM_sV \tag{2.14}$$

$$E_{max} = K_UV\left(1 - \frac{M_sH}{2K_U}\right)^2 \tag{2.15}$$

The energy barrier ΔE is therefore given by $E_{max} - E_{min}$ as

$$\Delta E = K_UV\left(1 - \frac{M_sH}{2K_U}\right)^2 \tag{2.16}$$

As can be seen from equation 2.16 ΔE is proportional to V and K_U in zero applied field. On application of an external field the energy barrier is lowered until alignment of the moment along the field direction can occur. The energy barrier is also lowered with increased temperature [40] via a fictitious field known as the fluctuation field H_f. A schematic of the thermal activation of a single grain is shown in figure 2.14 where an initial field is applied and then removed after saturation is reached. After this point thermal energy will cause the magnetisation to fluctuate with an attempt frequency f_0 until ΔE is overcome. The relaxation time τ of a uniaxial particle is given by the Néel-Arrhenius law

$$\tau^{-1} = f_0 exp(-K_UV/k_BT) \tag{2.17}$$

The relaxation time is extremely sensitive to the volume of the particle e.g. in the case of Cobalt particles at room temperature a change from 6.8 to 9nm will increase τ from

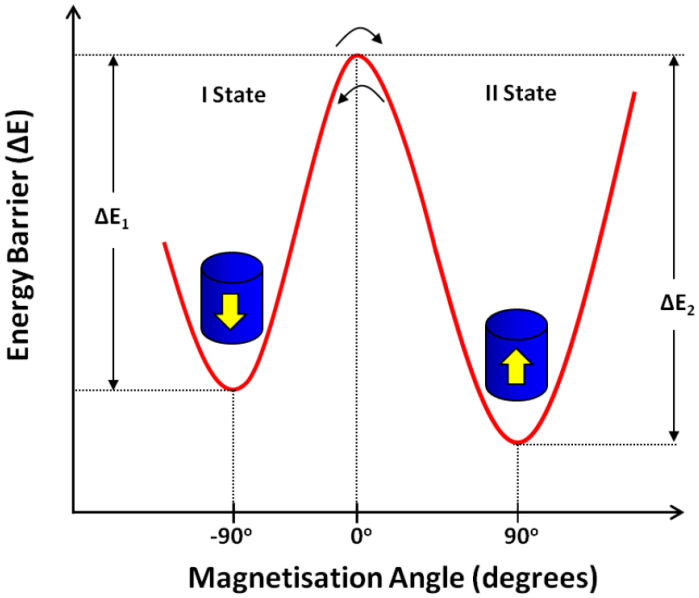

Figure 2.13: Schematic of the energy barrier to reversal with respect to angle of magnetisation.

0.1s to 100 years. If τ is shorter than the time of measurement then the material is said to be superparamagnetic.

For a fixed temperature the change in the magnetisation M is found experimentally to follow

$$M = const + S_v ln(\frac{t}{t_0}) \tag{2.18}$$

where t is the time since the field change, t_0 is a constant the origin of which is described in [57] and S_v is the coefficient of viscocity the sign of which is dependent on the direction of the change in field [58]. The linear change of M in ln$t$ is found only if there is a distribution of the energy barriers as is the case in a polycrystalline film.

In the case of a single domain AF particle no field is felt and as such equation 2.16 simplifies to $\Delta E{=}K_{AF}V_{AF}$. However the AF grain will behave analagous to that of a Stoner-Wohlfarth entity and so undergo thermal activation following equation 2.17. In an AF polycrystalline thin film thermal activation will occur across a distribution of energy barriers as in the F case described above. In this case thermal activation will lead to

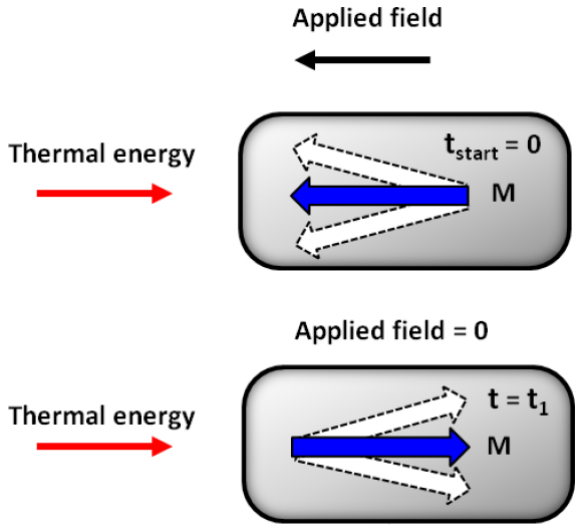

Figure 2.14: Schematic the thermal activation process in a single grain.

a disordering of the orientation of the grains magnetisation with respect to each other. However in the case of an exchange biased thin film the AF feels an effective field through direct exchange with the F layer. If the exchange biased film is then field cooled with the F at saturation the AF grains will orient with respect to the F layer. Through this process of thermal activation and field cooling the AF grains may be 'set'. This is shown through a ln$t$ dependence of H_{ex} with setting time consistent with thermal activation across a volume distribution. A similar measurement was also used to obtain the value of τ in the AF. This process is shown in the work of Vallejo-Fernandez et al. [59, 60] through use of the York Model which will be covered in more detail in chapter 3.8.

Chapter 3

Models and Measurements of Exchange Bias

Since its discovery in 1956 [1] exchange bias has undergone intensive research due in part to its technological application in the read head of a HDD. Despite this effort there is still no encompassing theory that can predict both the temperature and field dependence of the shift in the hysteresis loop (H_{ex}) and the evolution of the coercivity (H_c) which is defined as the half loop width. Part of the reason why the development of a coherent model has been hampered is the variety of systems in which exchange bias has been observed and studied. These range from nanoparticles where the F/AF interface will not be flat [1, 2] to sputtered polycrystalline films where the interface will have significant roughness leading to structural and magnetic frustration [3, 4] and finally epitaxially grown films with a near atomically flat interface [5, 6].

A number of models have been made of these systems in an attempt to predict H_{ex} and the increase in H_c with varying levels of success. However it is the sputtered polycrystalline films, and in particular the $IrMn_3$/CoFe bilayer system, which are used within the read head of a HDD. This is because it is the sputtered polycrystalline films which display the largest exchange bias at room temperature. As such, aside from a few key models, it is only those concerning polycrystalline films that will be covered in depth.

3.1 The Model of Meikljohn and Bean

The first and most simple model of exchange bias proposed was that of Meiklejohn and Bean [1, 9, 10]. In this model they attempted to predict the non-vanishing rotational hysteresis observed at high fields in exchange biased materials. They assumed a system where both the F and AF are single domain and of equal volume with a plane interface. The sole interaction considered is that of the direct exchange between the F and AF assuming the interface magnetisation of the AF is fully uncompensated. This coupling at the interface is taken to be weaker than in either the F or AF. A vector diagram of this model is shown in figure 3.1 with the interfacial energy given as

$$E_F = -HM_s t_F cos(\theta_H - \beta_M) + K_F sin^2 \alpha_{AF} - J_{INT} cos(\beta_M - \alpha_{AF}) \qquad (3.1)$$

Where H is the applied field, t_F is the F layer thickness, M_s and K_F are the saturation magnetisation and uniaxial anisotropy of the F layer respectively and J_{INT} is the interfacial coupling constant. The angles α_{AF}, β_M and θ_H in figure 3.1 are the orientation of the AF sublattice magnetisation, F magnetisation and applied field respectively.

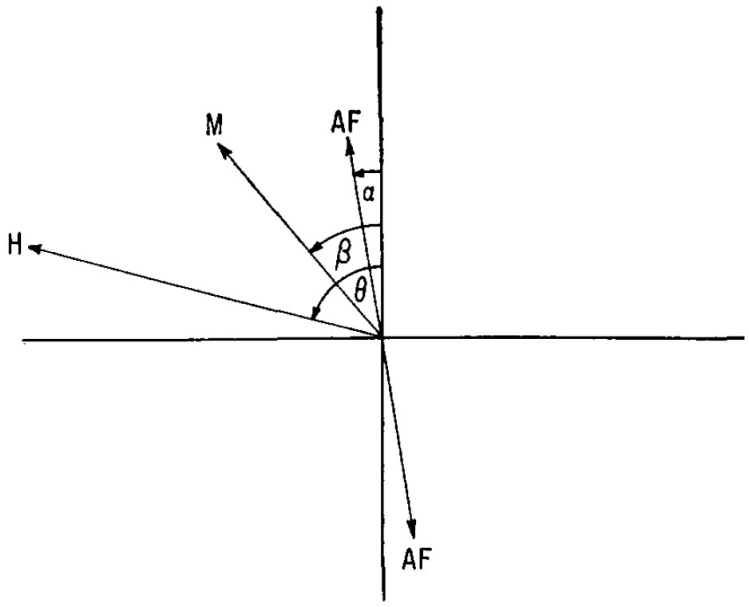

Figure 3.1: Vector diagram of the model of Meiklejohn and Bean [10].

In order to calculate H_{ex} and the increase in H_c a number of restrictions are required [61]. Firstly the applied field H must align along the easy axis with M_s taken to be constant. Secondly the angle α_{AF} must be rigidly fixed and parallel to that of the F layer easy axis. This allows equation 3.1 to be simplified to

$$E_F = -HM_s t_F cos\beta_M + K_F sin^2\beta_M - J_{INT} cos\beta_M \tag{3.2}$$

At saturation this energy has minima and maxima at β_M=0 and π given the conditions $J_{INT} + H + 2K_F > 0$ and $2K_F - J_{INT} - H > 0$ respectively. These conditions allow the bounds for the coercive fields H_{c1} and H_{c2} to be given as

$$H_{c1} = -\frac{2K_F + J_{INT}}{M_s tF} \tag{3.3}$$

and

$$H_{c2} = -\frac{2K_F - J_{INT}}{M_s tF} \tag{3.4}$$

where H_{c1} is the first point of reversal to negative saturation and H_{c2} is the point of return to positive saturation. As neither of these values is equal, a biased loop is obtained. This gives a bias field which can be defined as the midpoint of the hysteresis and is directly proportional to the interfacial coupling.

$$H_{ex} = \frac{J_{INT}}{M_s t_F} \tag{3.5}$$

This calculation gives a value of H_{ex} which is typically two orders of magnitude higher than that observed experimentally [62]. A number of causes for this have been suggested such as interface roughness, contamination and pinholes. However there are some fundamental issues such as if the interface in the model is instead assumed to be fully compensated no loop shift is predicted which again is not the case. Despite this, the conclusion can be drawn that in order to obtain exchange bias the condition of $K_{AF} t_{AF} \geq J_{INT}$ must be met. If this is not the case then the AF will simply rotate with the F magnetisation giving only an increase in H_c with no loop shift.

3.2 Domain Models: Classical

In order to improve upon the model of Meiklejohn and Bean a number of modifications to equation 3.1 have been made arising from many different sources. A number of these involved the formation of domains within the AF. In the case of a F domain formation is due to the the demagnetising field H_d however in an AF $H_d \simeq 0$ and therefore domains are unlikely to occur. This is because there will be insufficient magnetostatic energy in the AF to overcome the magnetocrystalline anisotropy. In the case of polycrystalline AF films, for any domains that do form there is no mechanism to allow any domain walls present to propagate e.g. intergranular exchange. However in exchange biased materials the F layer can provide sufficient magnetostatic energy to the AF to allow the formation of domains. Such a situation was first proposed by Néel [63] and observed optically by Shull [55]. The first of the models to make use of this were those of Malozemoff and Mauri et al. [11, 12].

In the model of Mauri et al. it was proposed that the formation of a domain wall in the AF leads to the reversal of the spins at the interface. This leads to the modification of equation 3.1 by adding a domain wall energy term $2\sqrt{S_{AF}K_{AF}}$ where S_{AF} is the exchange stiffness in the AF. This term arises due to the tail of a domain wall in the F layer extending into the bulk of the AF [64] which gives the value of H_{ex} as

$$H_{ex}M_s t_F = 2\sqrt{S_{AF}K_{AF}} \tag{3.6}$$

Despite the success of the model in calculating H_{ex} it fails to predict the increase in H_c as well as the training effect which is the decrease in H_{c1} with field cycling. The authors attempt to explain this as being due to the pinning of the domain walls in the AF by imperfections which leads to irreversible changes at the interface. However a key assumption of the model is that the AF layer must be thicker than the domain wall width $\pi\sqrt{S_{AF}/K_{AF}}$. This is clearly not the case in the $IrMn_3$ films used in modern HDD read heads where K_{AF} is $> 5 \times 10^6$ergs/cc with a thickness of 6nm.

The model of Malozemoff [11] attempts to simplify the calculation of the exchange field H_{ex} by assuming a uniaxial F layer with a domain wall driven by an external field H. This gives a prediction of H_{ex} by calculating the difference in the two interfacial energies $\Delta\sigma$

of the F/AF interface between the two oppositly magnetised regions of the F layer. This is given by

$$H_{ex} = \Delta\sigma / M_s t_F \tag{3.7}$$

However this equation assumes an atomistically perfect interface. Malozemoff takes this into account by assuming a random interface roughness. This variation at the interface leads to a local unidirectional interface energy $J_{INT} = \pm z_c c_e / a^2$ to be random where z_c and c_e are a number of order unity and the magnitude of the exchange constant respectively. By allowing a planar domain wall to form in the AF at the interface the overall energy of the system can be decreased similar to that of Imry-Ma domains [53]. However during field cooling the F layer is a single domain. With the assumption that the bulk AF configuration is fixed the AF domain pattern must be frozen in during field cooling through its ordering temperature.

On freezing the size of the AF domain is assumed to be constant and is defined as $L_D \simeq \pi\sqrt{S_{AF}/K_{AF}}$. If half of the AF interface exchange fields point in each direction then the energy change per unit area when reversing the F layer is given by $\Delta\sigma = 4 z_c J_{INT} / \pi a L_D$. By inserting this into equation 3.7 along with the value of L_D the exchange anisotropy field is given by

$$H_{ex} = 2 z_c \sqrt{S_{AF} K_{AF}} / \pi^2 M_s t_F \tag{3.8}$$

Again this model is able to predict the magnitude of H_{ex}. However as with the model of Mauri it cannot account for variation in the coercivity. Malozemoff also cites the work of Kouvel [52] as giving similar results. However the model of Kouvel and results apply to CuMn and related alloys where Mn rich regions give AF behaviour and as such is not comparable to the NiFe/FeMn thin film systems modelled by Malozemoff. Furthermore the domain sizes obtain in $IrMn_3$ exceed the 6nm thick and $< 50nm$ diameter grains obtained in the polycrystalline films used in the read head of a HDD. Another major issue with these two models is that neither take into account the temperature dependence of the exchange bias.

3.3 Domain Models: Computational

With the vast increase in computational power post-1990 there came a marked change in the modelling of exchange bias from the solving of energy equations to micromagnetic modelling of the spin structure at the interface. Of the earlier micromagnetic models it was those of Koon [65] and Schulthess and Butler [66, 67] that saw the most success.

The model of Koon [65] uses a similar model to that of Mauri in that the F/AF interface is perfectly flat and fully compensated with the formation of a domain wall in the AF. The spin structure of the F/AF is assumed to be a simple body centered tetragonal with the exchange interactions along the body diagonal. This gives a simple ordering in the AF where the spins in the two sublattices are oriented in opposite directions and only interact with the spins on the opposing sublattice as shown in figure 3.2 a).

Using this model Koon calculated the angular dependence of the orientation of the F magnetisation on the interfacial energy. This was done for both a frustated and pure F/AF interface where the former corresponds to that of a fully compensated AF. For the frustrated interface the minimum energy occurs when the F couples at 90° to that of the AF easy axis. The configuration of the spins in such a situation is shown in figure 3.2 b) where the AF spins cant away from the direction of the F. This canting angle decays rapidly to zero at 5-6 monolayers which is analgous to that of the AF spin-flop state.

The model of Koon was able to calculate the value of H_{ex} as obtained in Co/CoO [1] and

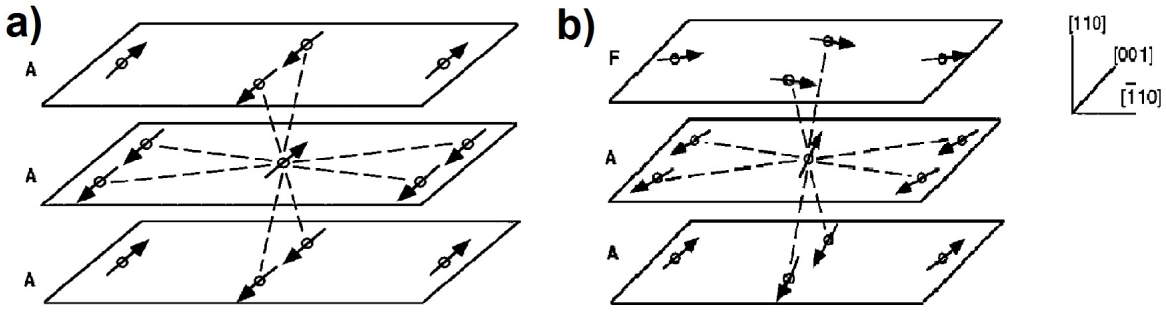

Figure 3.2: Spin structure diagrams showing a) the magnetic structure and interactions of the AF assumed by the models of Koon and Schulthess and Butler and b) spin-flop coupling at the F/AF interface [65].

Fe/FeF_2 [68,69] thin films. Furthermore it predicted both a decrease in H_{ex} with increasing roughness [69] and the observation of a positive exchange bias when field cooled in large applied fields ($\sim$70kOe) [68]. However one of the assumptions made to obtain this result was that spin motion in the film is parallel to the interface. Although this is a reasonable assumption for the F spins it is not for the AF spins. Schulthess and Butler [66,67] relaxed this constraint and found that spin-flop coupling led only to a uniaxial coupling and an increase in H_c with no loop shift. This led to the idea that two coupling mechanisms were at play. The first was that of spin-flop coupling and the other F/AF coupling due to uncompensated defects. By adding an AF defect in the F layer both H_{ex} and the increase in H_c could be predicted. However despite the success of these models they still neglected the time, temperature and setting field dependence of H_{ex} and furthermore are only applicable to that of near-epitaxial single crystals.

3.4 The Domain State Model

The domain state model is similar to the model of Malozemoff [70] in that it is thought that domains can form in an AF due to defects within the film. However in the domain state model these defects are within the bulk of the AF and are assumed to lead to the formation of a domain state. The domain state model uses the random field argument of Imry-Ma [53] and by assuming a dilute AF it was thought that a domain state could form by either a) cooling the sample to below T_N in an applied field or b) applying and decreasing a sufficiently high field [71]. As mentioned in a previous section there is normally insufficient magnetostatic energy to form a domain wall in an AF. However in the theory of Imry-Ma [53] if a domain wall can pass preferentially through a non-magnetic defect the energy cost is brought to a minimum allowing the formation of a domain. These domains are of non-trivial shape with a distribution of sizes following from energy optimisation.

A 2D schematic of the spin configuration of a domain state as following the argument of Imry-Ma in a dilute AF is shown in figure 3.3. The defects are represented by black spots and can be either nonmagnetic ions or vacancies while the black line surrounds the domain of opposite orientation to the background. In the case of figure 3.3 the AF has been zero field cooled and so a small applied field is required to maintain the domain state [13,71,72].

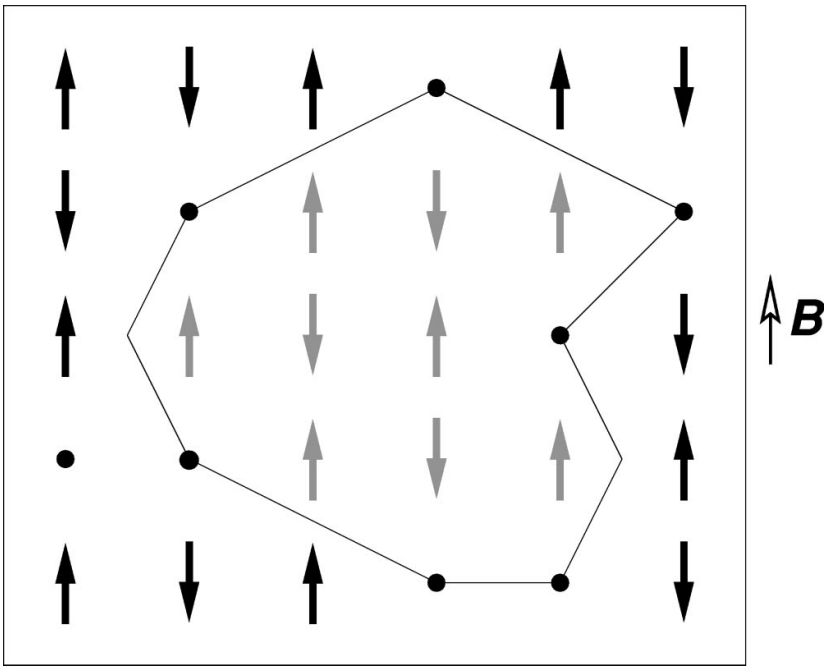

Figure 3.3: Schematic illustration a domain state in an AF [13].

However through comparison of the theory to experimental work it was found that by field cooling to below a critical temperature $T_i(B)$ the AF forms a meta-stable domain state with a remanent magnetisation that decays over time [72, 73]. The metastability of the domain state is thought to be due to the strong pinning of the domain walls by the AF dilution and the coupling of the domain wall magnetisation with the external applied field following the model of Imry-Ma [13, 53]. Such a field cooled system is what is proposed by the domain state model for an exchange biased system.

The domain state model of exchange bias is a Monte Carlo simulation which consists of a single F layer coupled to a dilute AF consisting of n monolayers. A 3D schematic of this model with n=3 is shown in figure 3.4. On calculation the model showed hysteretic behaviour of the AF interface magnetisation and upon field cycling there was found to be a change in M_s of $\sim 10\%$. This was thought to be proof of the remanent magnetisation in the AF domains. It is this shifted interface magnetisation that provides an effective field to the F and was proposed as the cause of exchange bias [13, 74]. This model does not predict the enhancement of H_c observed in exchange bias systems and so was extended using a mean field approach [75]. This was better able to predict the temperature dependence of

the enhancement of H_c whilst remaining at least in qualitative agreement with the previous Monte Carlo calculations. The increase in H_c was thus attributed to the coupling of the F with the AF interface magnetisation which follows the applied field.

The domain state model was able to provide a number of qualitative predictions of exchange bias. Firstly it was able to give an estimate for the loop shift. Secondly the dependence of exchange bias on the dilution of the AF was predicted. The model showed that with greater dilution the number of domains formed increased leading to a growth in the interface magnetisation of the AF and thus exchange bias. However if too many defects are entered into the system AF order is lost and therefore so is the exchange bias. The training effect was also predicted and was thought to be due to the relaxation of the remanent magnetisation of the AF interface with field cycling. A positive or reduced exchange bias was predicted as well and thought to be dependent on the sign of the coupling between the F and AF layers. Finally the domain state model predicted an AF thickness dependence of H_{ex}. For thin AF layers (0-4 layers) an increase in H_{ex} was predicted and explained as being due to an increase in the stability of the domain state. However with increasing thickness the energy required to form a domain wall increases meaning fewer are formed leading to a decrease in H_{ex} [6,13,74]. However the thickness of the AF layer where these features were observed was an order of magnitude thinner than volumes observed experimentally [76].

The ability of the domain state model to predict these facets of exchange bias meant it was the dominant model during the first decade of 2000. However a number of issues with the model has since seen it surpassed [4]. The first issue with the model are the systems it is applicable to. Most of the successful predictions of experimental results were for those

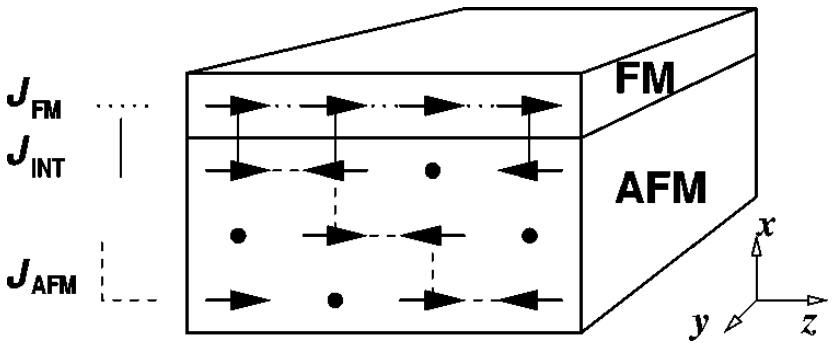

Figure 3.4: Schematic illustration of the domain state model where dots mark defects [13].

of single crystal Fe/FeF_2 and Co/CoO with controlled dilutions [6]. However in the case of the polycrystalline materials used in application, particularly for alloys such as $IrMn_3$, a number of system parameters are not considered. Firstly aside from perfectly textured materials there will be some distribution of the F/AF coupling dependent on the grain to grain variation of the orientation of the F/AF layers. Secondly in a polycrystalline material although a grain may be well crystallised the boundary between two grains will be essentially amorphous. This leads to a situation where within a grain there will be very few dilutions and therefore a domain state will not be favoured whilst in the grain boundary, dilutions will be at a maximum and therefore no domain state may form. Finally the value of the AF magnetocrystalline anisotropy K_{AF} was chosen initially to be sufficiently high to allow for a domain wall width of zero. Whilst the consequences of lifting this restriction were met with some success [74] the change in the basic model has not been discussed in detail in any publications since.

3.5 The Model of Fulcomer and Charap

The first granular model of exchange bias was that of Fulcomer and Charap [77]. It was developed in order to explain a number of features of exchange bias that had been observed in polycrystalline NiFe, Co and Ni films which had been coupled to their AF oxides NiO and CoO. The first of these was the presence of a transition temperature T_t below that of the T_N of the antiferromagnetic oxides at which H_{ex} decreases to zero. This in contrast to that of in single crystal films were $T_t \simeq T_N$. Furthermore at or near T_t a peak in the value of H_c is observed. Secondly H_{ex} is seen to increase with decreasing temperature. However this trend varies from material to material with NiFe increasing linearly with the logarithm of decreasing temperature whilst Co goes linearly with that of the temperature itself [78].

As well as the temperature dependence of H_{ex} and H_c a number of magnetic afteraffects are also observed. This is where a magnetic aftereffect is defined as a delay in the change of the magnetisation following a variation in the magnetic field [78]. In oxidised NiFe films this was seen through the direct observation of the slowed motion of domain walls with a constant applied field [79]. The training effect observed after field cooling is another example of a magnetic aftereffect [80,81]. Finally in torque measurements a large decrease is observed

over many seconds in an applied field of constant magnitude and direction [82]. Fulcomer and Charap postulated that if the magnetic aftereffect was a fundamental characteristic of exchange biased materials then both H_{ex} and H_c will be frequency dependent [78].

This was confirmed through a set of experiments carried out on three different NiFe films which were deposited by vacuum deposition. The main sample studied was a NiFe film that had been exposed to air for a number of years. This was reduced in a dry hydrogen environment and oxidised controllably in a wet oxygen atmosphere and measured in steps of supposed oxided thickness. The remaining two were control samples which were made so that one was a non-oxidised NiFe film with a SiO cap while the other was a NiFe film oxidised in a wet oxygen atmosphere containing 1ml of 3% hydrogen peroxide. The temperature dependence of H_{ex} and H_c for these samples was measured using the Magneto Optical Kerr Effect (MOKE) at a range of frequencies from 0.05Hz to 100Hz [78].

The experiment showed the expected increase of H_{ex} and H_c with decreasing temperature however T_t was found to be dependent on the level of oxidation. Also the peak in H_c near T_t was found to be frequency dependent and disappeared when measured below

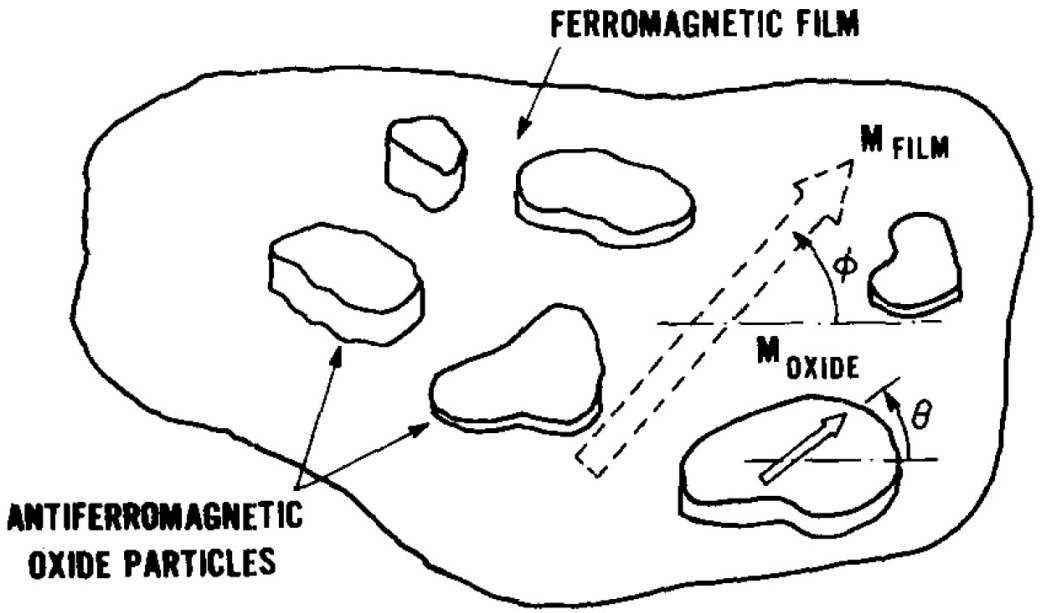

Figure 3.5: Schematic illustration of the AF oxide particles coupled to the underlying F layer [77].

1Hz for all the oxidised samples. Finally it was found that H_{ex} increased with frequency whilst H_c decreased. Given that the antiferromagnetic oxide is likely to be composed of fine particles Fulcomer and Charap came to the conclusion that the magnetic aftereffects were due to thermal fluctuations. This led to the concept that T_t was in fact the blocking temperature T_b of the largest AF particle. To model this Fulcomer and Charap developed a thermal fluctuation aftereffect model.

In the model of Fulcomer and Charap the AF is modelled as non-interacting particles that are distributed in size and shape and exchange coupled to the moment of the underlying F layer, a schematic of which is shown in figure 3.5. In the model it is assumed that the F and AF easy axis lie parallel. The value of H_{ex} is therefore given by the angle between the AF surface moment and the F easy axis. As such when the F layer is reversed the sign of the coupling between the F and AF changes leading to switching of the AF particles through thermal fluctation. This was said to lead to the formation of a new equilibrium state of the angle between the AF surface moment and F easy axis over a given time.

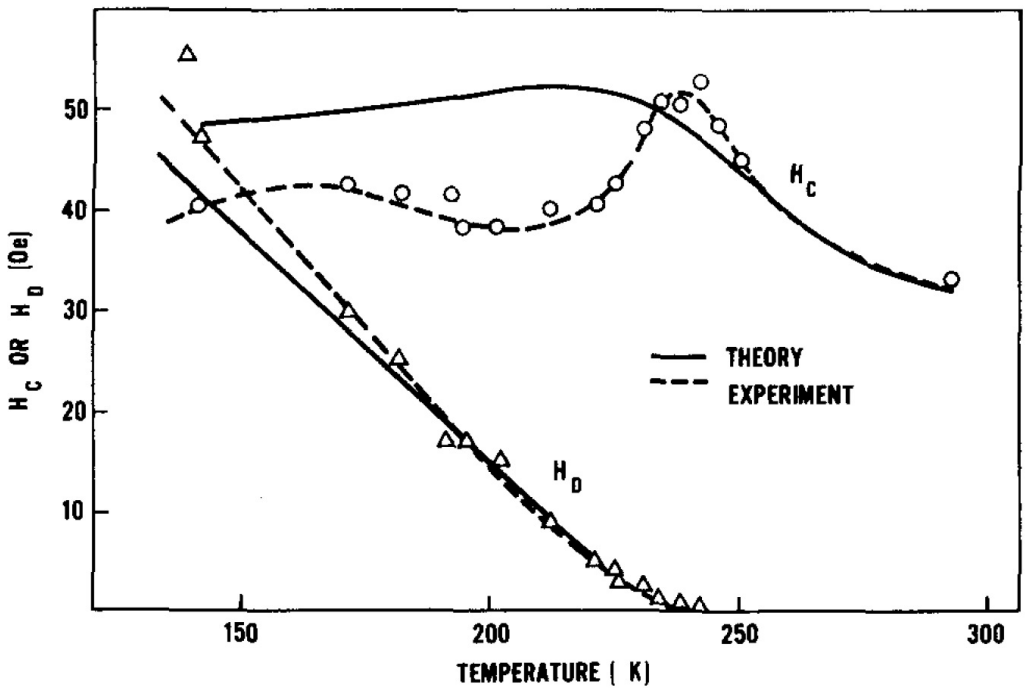

Figure 3.6: Theoretical fit derived using the thermal fluctation afteraffect model and plotted against experimental results for Co/CoO films [77, 82].

As this relaxation time increased with temperature the concept of T_t being equivalent to a T_b of the AF particles was introduced. This leads to the definition of T_b being that if the temperature of the experiment $T{=}T_b$ then the relaxation time of the AF particles is equal to the time of measurement and therefore $H_{ex}{=}0$. As the sample is cooled and $T{<}T_b$ the relaxation time increases and so the AF particles appear to be blocked leading to an increase in H_{ex} whereas when $T{>}T_b$ the opposite occurs and so the AF was labelled as superparamagnetic [77, 78].

This model and the associated experimental work helped to show the importance of both the time and temperature of the measurement where an AF particle that is blocked when measured at a frequency of 1kHz might not be so at 1Hz. The distribution of AF particle diameter and thickness was also considered and used to predict the temperature dependence of H_{ex} and H_c for Co/CoO films [77]. The experimental results and calculated values are shown in figure 3.6. As can be seen the model fits the results for H_{ex} very well. However the fit for H_c is poor although unlike previous models reasonable values are obtained. Fulcomer and Charap explain this discrepency in H_c as being due to a number of things. Firstly they only considered a single distribution when defining the shape and size of the AF particles. Secondly it was proposed that the values of K_{AF} and J_{INT} may be different in small particles from in bulk. Finally they state that the location of the AF particles is unknown and some could be located on grain boundaries leading to unexpected behaviour [77]. An important point to consider about the model is that although it takes into acount a distribution of particle volumes it is stated that the shape of the distribution is irrelevent which will be seen to not be the case [4]. Furthermore the samples were not at T_{na} and so the AF will have been thermally active leading to irreproducible changes occuring with measurement times greater than the AF relaxation time.

3.6 The Measurements of van der Heijden

The measurements of van der Heijden et al. [83, 84] gave strong evidence towards a thermal activation model of exchange bias in polycrystalline thin films. In the work of van der Heijden et al. the temperature dependence of the relaxation time of the AF orientation was measured in samples with NiO layers of thickness 40 and 60nm [84] which were then compared to films

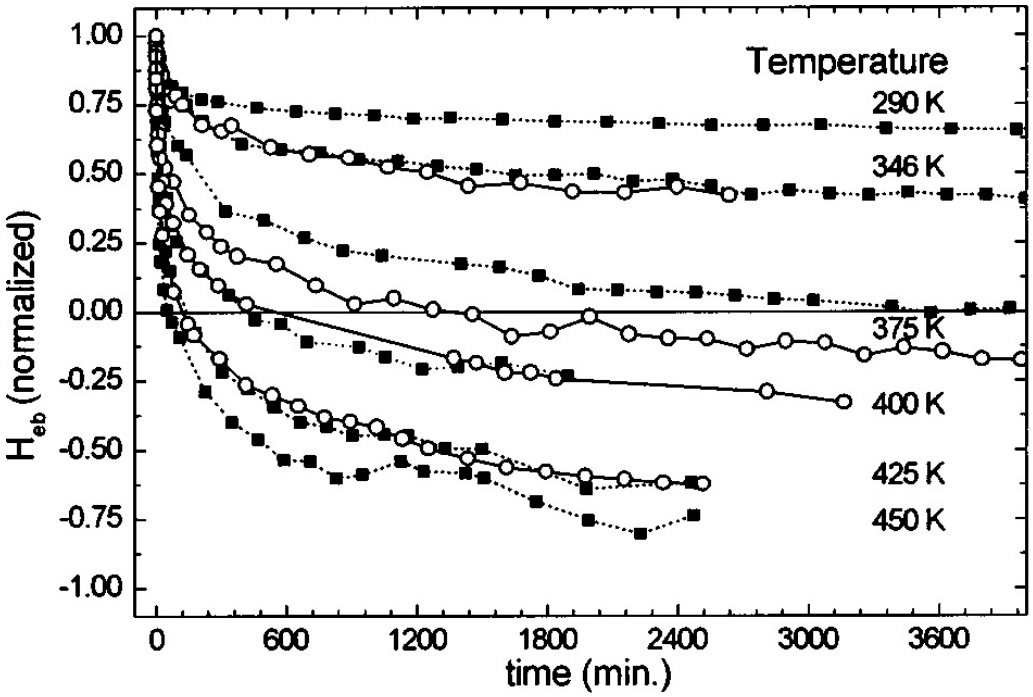

Figure 3.7: Time dependence of H_{ex} as a function of time at different temperatures with a field applied so as to negatively saturate the F layer [83].

with the AF FeMn [83]. The metallic and oxide films were deposited using Direct Current (DC) and Radio Frequency (RF) magnetron sputtering respectively and the hysteresis loops were measured using a temperature controlled MOKE.

The samples were first annealed at 500K and then cooled in a field of 565 Oe to room temperature over a time of 10 hours. A field of 565 Oe was then applied opposite to that of the setting field and the desired temperature set. The value of H_{ex} was then measured as a function of time with a constant temperature. Although the value of H_{ex} was obtained from a hysteresis loop and therefore by varying the applied field the time of measurement was 12s and so was insufficient to cause any observable changes [84]. The result of these measurements is shown in figure 3.7. It was found that the relaxation time of the AF orientation was temperature dependent with H_{ex} reversing sign when heated to T_b. Furthermore a drop in H_{ex} of 25% was observed at room temperature over a time of 4 hours. This shows that at room temperature changes in the AF order are observed. In previous works using NiO and similar AF materials this was not considered and as such the measurements would not have been reproducible [68, 69, 78].

The temperature dependence of H_{ex} was compared for 40nm and 60nm of NiO. No change was observed with AF layer thickness which disagrees with the model of Fulcomer and Charap [77, 78]. Van der Heijden et al. suggested that the grains of NiO were in fact multi-domain and that the use of the model of Malozemoff [70] would have been more applicable. A sample with 10nm of FeMn was also measured however no other thicknesses were attempted [83]. Although the formation of domains in a 60nm thick layer of NiO is reasonable it is far less likely to have occured in the 10nm thick FeMn layer. Furthermore the distribution of grain sizes was not measured. As the volume of a grain varies in quadrature with its radius whilst only linear with its thickness the change from 40 to 60nm would have been negligble. Furthermore the temperature dependence was carried out at different values of applied field with no observable change. The conclusion of van der Heijden et al. was that in order to obtain exchange bias the F layer must be at saturation. However the magnitude of H_{ex} is independent of the applied field beyond this. This is in disagreement with a number of studies where an increase in H_{ex} is observed in setting fields of up to 80kOe [25].

Although the measurements of van der Heijden et al. confirmed the validity of a thermal activation model for polycrystaline thin films a number of key conclusions were neglected. First of all the comparison between NiO and FeMn [83] showed that the assumption made in the model of Fulcomer and Charap [77] that the oxide particles were exchange decoupled may also be applied to that of metallic granular films. This is not immediately obvious as interactions between nearest neighbour grains would be expected. Second of all the temperature dependence of the relaxation time looks to be linear in lnt however no attempt to plot this was made [4, 83, 84]. Finally only 2 AF layer thicknesses were measured limiting the ability to draw any real conclusions on the effect of the AF grain volume on the temperature dependence of the relaxation time.

3.7 The Model of Stiles and McMichael

The model of Stiles and McMichael is similar to that of Fulcomer and Charap in that it is granular and assumes exchange decoupled AF grains that interact solely with the underlying F layer. However there are a number of key differences betwen the models. Whilst Fulcomer

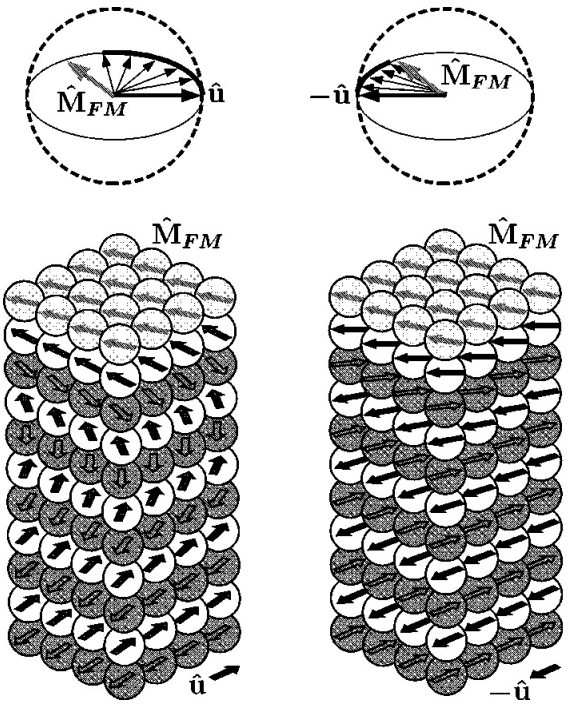

Figure 3.8: Schematic diagram of the domain wall formation in a single AF grain for two different orientations of the sublattice [85].

and Charap assume that the AF grains have uniform orientation and magnetisation, Stiles and McMichael assume a randomly oriented AF and allow the formation of a domain wall parallel to the interface. Furthermore they neglect any distribution in grain size and therefore energy barrier and instead choose a fixed size that is equivalent to the domain wall length [85, 86]. The model was only initially used for the prediction of the behaviour of the rotational hysteresis and ferromagnetic resonance of exchange biased films however it was later extended towards the calculation of both H_{ex} and the increase in H_c [87].

In the model of Stiles and McMichael the AF is polycrystalline and exchange decoupled and interacts solely with the F layer. The AF grains are assumed to have a uniaxial anistropy with a random distribution of easy axis directions in three dimensions. The coupling between the F and AF is only due to direct exchange. Spin-flop coupling was considered in the first presentation of the model however it was found to eliminate any unidirectional anisotropy and so was not considered in later modifications [85]. The coupling varies in magnitude from grain to grain due to disorder at the interface leading to both sublattices being present. This

gives a mixture of compensated and uncompensated spins at the interface in each grain which, when averaged over all the grains, leads to a net coupling. In the case of the basic model the F layer is assumed to be fully saturated with its magnetisation being rotated by an external applied field. As this occurs the AF interface magnetisation attempts to align with it. This leads to the formation of a partial domain wall within the AF in an attempt to minimise the exchange energy. In an isolated AF grain there are two possible configurations and as such two possible domain wall energies. This is shown schematically in figure 3.8 with the total energy of the each configuration given by the equation

$$E^{\pm} = -N_s J_{net} \hat{M}_{FM} \cdot \hat{m}_{int}(0) + \frac{N_s a_s^2 \sigma_d}{2}[1 - \hat{m}_{int}(0) \cdot (\pm \hat{u}_{ea})] \tag{3.9}$$

where $\hat{m}_{int}$ and $\hat{M}_{FM}$ are the directions of the AF interfacial and F magnetisations respectively, a_s^2 and J_{net} are the area of the interface and interfacial coupling per spin respectively, σ_d is the domain wall energy per unit area in the AF, $\hat{u}_{ea}$ is the deviation of $\hat{m}_{int}$ from the AF easy axis direction and N_s is the number of spins at the interface of a given grain. As a distribution of easy axis is assumed this leads to a grain to grain variation in the interfacial coupling energy $N_s J_{net}$. In real samples there would be a distribution of grain size N_s which is neglected in the model.

This model was extended to try to explain the temperature depedence of exchange bias [86]. It was assumed that the value of T_C of the F layer far exceeds T_N of the AF and that the properties of the F are independent of the temperature. They further assume that the moment in the AF at the interface is temperature independent which from a number of low temperature measurements is known to not be the case [45, 46, 88]. To add temperature dependence to the model two contributions are thought to be present. The first is the temperature dependence of the domain wall energy where the approximation $\sigma_d = \sigma_{d0}(1 - T/T_N)^{5/6}$ is used. This was done to ensure that domain wall formation becomes more likely as T approaches T_N. The second contribution is that of thermal activation of the AF grains. However unlike the model of Fulcomer and Charap the columnar grains are sufficiently thick to support the formation of a domain wall. Therefore the mechanism of grain reversal is that of domain wall motion where the wall nucleates at the F/AF interface and propagates through the AF grain. This leads to similar behaviour to that of the model of Fulcomer and Charap in that, with increasing temperature, the relaxation time decreases.

In order to calculate the probablity of reversal at a given temperature an energy barrier ΔE between the initial (+) and final (-) state was given by a modification to equation 3.9 to give

$$\Delta E = \frac{N_s a_s^2 \sigma_d}{2}([1 + 2r_{dc}\hat{M}_{FM} \cdot \hat{u}_{ea} + r_{dc}^2]^{1/2} - [1 - 2r_{dc}\hat{M}_{FM} \cdot \hat{u}_{ea} + r_{dc}^2]^{1/2}) + N_s r_{dc}^2 \sigma_d \quad (3.10)$$

where r_{dc} is the ratio of the direct coupling and domain wall energies. During a measurment over a time t at a temperature T the probability P_{rev} of crossing this energy barrier is given by

$$P_{rev} = exp[-f_0 t exp(-\Delta E/k_b T)] \quad (3.11)$$

where f_0 is the attempt frequency and k_B is Boltzmann's constant. By assuming f_0= $1 \times 10^9 s^{-1}$ and t=1 for most values of ΔE the probablity is near 1 for most angles of applied field with a rapid transition to close to 0 occuring for all other angles. This led to the model making a further approximation that the probablitiy of reversal should either be 1 or 0 with an energy barrier

$$\Delta E/k_B T \approx 20 \quad (3.12)$$

This energy barrier gives three regimes for the AF grains. If $\Delta E > 20 k_B T$ then the grain is assumed to be stable in the initial state and if $\Delta E < 20 k_B T$ then it is unstable. The third regime occurs when the energy of the opposing state is $2N_s a_s^2 \sigma_d - \Delta E < 20 k_B T$ at which point both states are unstable and the grain is said to be superparamagnetic.

This model shares similar success to that of the model of Fulcomer and Charap in its ability to predict the thermal behaviour of exchange bias however it is strictly applicable only to systems with AF grains of sufficient size to support a domain wall. Furthermore a number of assumptions made are clearly not valid such as the temperature independence of the interfacial moments. Although both the models of Stiles and McMichael [85–87] and

Fulcomer and Charap [77, 78] are relatively complementary, the fundamental assumptions do not match i.e. a unidirectional anisotropy is assumed in the former with a multidirectional one used in the latter. As such, a coherent model that is able to explain both regimes of mono- and multi-domain grains is required. The York Model of Exchange Bias is the first model to achieve this and is that used in this work.

3.8 The York Model

In the models and experimental work described previously it can be seen that exchange bias is affected by a thermal activation process. However in the vast majority of the experimental work and in particular those carried out at room temperature, thermal activation of the sample during the time of the measurement is neither considered nor accounted for. This is reflected in the theory where attempts to model certain behaviour thought to be fundamental to exchange bias are in fact due to the sample changing in the time of the measurement. A good example of this is the training effect where a decrease in H_{c1} is observed when cycling multiple hysteresis loops [13]. With the development of the York Protocols the training effect is found to occur in the first loop only [4, 89]. This is due to the concept of measuring at a temperature at which no thermal activation occurs in the AF, T_{na}. Above T_{na} the relaxation time of some portion of the distribution of AF grains is shorter than that of the measurement time leading to changes in the AF ordering and therefore H_{ex}/H_c. Below T_{na} reproducible measurements can be made which lead directly to the developement of the York Model of Exchange Bias.

The success of the York Model has shown that the AF consists of an ensemble of grains distributed in size. These are single domain in the typical case of sputtered thin films with grains 5-20nm in diameter. In single domain particles a magnetic transition will occur via thermal activation across an energy barrier $\Delta E{=}K_{AF}V_{AF}$ [77, 78] where V_{AF} and K_{AF} are the volume and anisotropy of the AF grain. The critical volume below which thermal activation will be observed is dependent on the temperature and time of the measurement. This relaxation time τ is given by the Néel-Arrhenius law

$$\tau^{-1} = f_0 e^{\left[\frac{K_{AF}V_{AF}(1-H^*/H_K^*)^2}{k_B T}\right]} \tag{3.13}$$

where f_0 is the attempt frequency which is has been measured to be $1 \times 10^{11}\text{s}^{-1}$ [60], k_B is Boltzmann's constant and T is the measurement temperature. The field H^* is the exchange field from the F layer that acts to lower ΔE whilst H_K^* is a pseudo-anisotropy field in the AF similar to that of ferromagnetic single domain particles. The values of H^* and H_K^* are not known however the ratio H^*/H_K^* is assumed to be small. This assumption has been shown to be the case for most F/AF systems used in applications [59, 90]. It should be noted that K_{AF} is temperature dependent due to it being magnetocrystalline in origin. This temperature dependence is of the form

$$K_{AF}(T) = K_{AF}(0)(1 - T/T_N)^n \tag{3.14}$$

where n is unity due to the proportionality $K_{AF} \propto [m_{AF}(T)/m_{AF}(0)]^3$ with the approximation $m_{AF}(T) \propto (T/T_N)^{1/3}$ where m_{AF} is the moment of one of the AF sub-lattices [86].

One of the major issues with the calculation of K_{AF} is that it is unclear to what extent the interfacial coupling, which in the York model is described by the dimensionless variable C^*, moderates the value of H_{ex}. Therefore unless the state of order in the AF and the interface is carefully controlled K_{AF} cannot be calculated. The York Protocols which are described in detail in Chapter 5 can be used to measure the median blocking temperature $\langle T_b \rangle$. This is defined as the point at which the AF is set so that equal fractions of the grain volume distribution are in opposite orientation. The importance of $\langle T_b \rangle$ is that $H_{ex} = 0$ and so not only does the contribution due to the AF grain volume distribution cancel but also that of C^*. This allows for the calculation of K_{AF} at the temperature of $<T_b>$ which from equation 3.13 is given by [4, 47]

$$K_{AF}(< T_b >) = \frac{ln(tf_0)}{V_m} K_B < T_b > \tag{3.15}$$

where V_m is the median grain volume. Once K_{AF} is known it may be calculated at any temperature using equation 3.14. Using these equations Vallejo-Fernandez et al. found the value of K_{AF} in $IrMn_3$ (at 295K) to be $(5.5 \pm 0.5) \times 10^6 \text{ergs/cm}^3$ in films of thickness $\geq$ 4nm with a decrease to $(4.7 \pm 0.5) \times 10^6 \text{ergs/cm}^3$ occuring for layers $\leq$ 3nm. This behaviour was attributed to a lack of crystallisation in the grains [4, 47]. It is noted in the work that the value of K_{AF} is an effective value. This is due to the assumption in the

York Model that the AF easy axes are aligned. This will not be the case in polycrystalline materials as depending on the texture of the layer this could range from fully disordered in three dimensions to aligned within the plane of the film. Evidence of this is shown in the work of Aley et al. where a variation in the measured value of K_{AF} is observed with the (111) texture in $IrMn_3$ [17]. It is important to note that if there is a grain size dependence of the interfacial order then C^* may not cancel at $<T_b>$.

A final aspect of the model is that there is no granular exchange in the AF. Intergranular exchange can work to lower the overall ΔE of the system however there is no evidence of this in the case of AF grains in polycrystalline thin films. In a polycrystalline F layer intergranular exchange occurs via RKKY coupling where each grain must possess a large moment in order to polarise the conduction electrons. This coupling is reduced or even eliminated if the grain possesses an AF boundary e.g. in the case of Co alloy recording media with a CoCr boundary [38]. It is therefore expected that AF/AF coupling will not occur via RKKY coupling. Furthermore from crystallographic studies using TEM it is clear that the grain boundaries in the films used in this work are amorphous and as such direct exchange will not occur [4]. This gives an indepedendent and single domain AF grain model similar to that of Fulcomer and Charap [77].

3.9 The Effect of the AF Grain Volume Distribution

As the anisotropy in an AF is magnetocrystalline it is constant across the film and so ΔE for each grain will be dictated by its volume. Furthermore for high K_{AF} materials such as those used in industry, it is not possible to field cool from above T_N withough causing significant interlayer diffusion. Therefore the process through which the AF is set is thermal activation across a distribution of energy barriers. A schematic of the distribution of energy barriers to reversal for a sample measured at a temperature $T_{ms}>T_{na}$ after setting at a temperature T_{set} over a time t_{set} is shown in figure 3.9. In such a situation the distribution of AF grains is not fully set during the setting and field cooling stage. As such the grains with $V>V_{set}$ are not aligned with the F layer. Furthermore at temperatures above T_{na} a certain fraction of grains with $V<V_C$ are thermally active analagous to that of superparamagnetic particles [77]. It is therefore only those grains whose volume is within the window $V_C<V<V_{set}$ that contribute

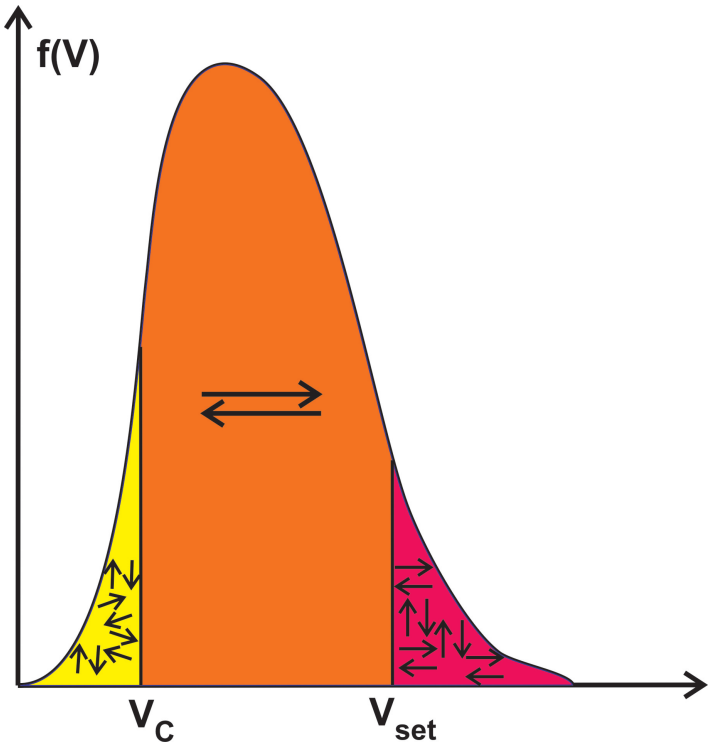

Figure 3.9: Schematic diagram of the AF grain volume distribution with the threshold volumes V_C and V_{set} when measured at T_{ms}>T_{na} after setting at T_{set} for a time t_{set} [4].

to H_{ex}. This can be expressed by the equation [4]

$$H_{ex}(H_{set}, T_{set}) = H_{ex}^{i} C^{*}(H_{set}, T_{set}) \int_{V_c(T_{meas})}^{V_{set}(T_{set})} f(V) dV \tag{3.16}$$

The limits of this integral can be calculated using equation 3.13. In the case of the experimental results of Vallejo-Fernandez et al. [4, 91] shown in figure 3.10 a) the lower bound due to the thermally active grains of volume V_C is given by

$$V_C = \frac{ln(t_{ms} f_0) k_B \times T_{ms}}{K_{AF} T_{ms}} \tag{3.17}$$

where t_{ms} is the measurement time at a temperature T_{ms}. To carry out a measurement at T_{na} for a given AF grain t_{ms} must be less than the relaxation time τ which is controlled by T_{ms}. Therefore either T_{ms} or t_{ms} must be minimised. As these measurements were carried

out by VSM t_{ms} is limited to 1800s. As such T_{ms} must be chosen to ensure τ of the smallest grain is greater than t_{ms}. The second limit due to the unset grains V_{set} is given by

$$V_{set}(T) = \frac{ln(t_{set} f_0) k_B \times T_{set}}{K_{AF} T_{set}} \tag{3.18}$$

where the value of t_{set} is the setting time at a temperature T_{set} prior to field cooling. As opposed to before τ of the largest AF grain must be minimised to be significantly shorter than that of t_{set}. This is done by maximising both T_{set} and t_{set} however these are limited to reduce damage to the sample through interdiffusion and for the setting process to remain a practical length. Using the limits t_{ms}=1800s, T_{ms}=293, t_{set}=5400s and T_{set}=498K Vallejo-Fernandez et al. [4,91] calculated the intergral in equation 3.16 in order to predict the lateral grain diameter and AF layer thickness dependence of H_{ex}. These calculations (lines) along with the experimental results (points) are shown in figure 3.10 b). As can be seen the fit to the results is superb with the values of H_{ex} being scaled along the ordinate by the interfacial coupling constant C^* which is a dimensionless value of value between 0 and 1.

A further prediction of the York model is that the wide distribution of AF grain volumes and therefore ΔE leads to a $ln(t_{set})$ dependence of the AF order. This is similar to the

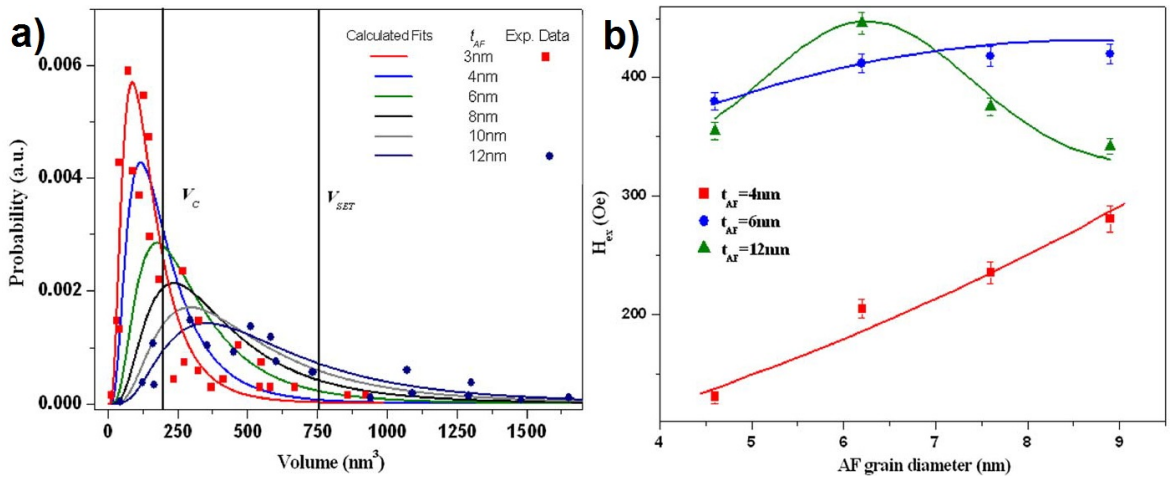

Figure 3.10: Measured a) grain volume distributions for samples of different AF layer thickness with calculated volume thresholds and b) AF thickness and grain diameter dependence of H_{ex} where the lines are calculated using equation 3.16 [4].

effect observed in a F system where a wide distribution of energy barriers leads to a $ln(t)$ dependence of M [92]. Like in the F case it is the order parameter P_{AF} that controls H_{ex} which follows a $ln(t)$ law. This setting process has a time depedence coefficient $S = (dP_{AF}/dlnt_{set})$ that can be written as [58]

$$S(T) = 2P_S k_B T f[V_P(T)] \tag{3.19}$$

$$V_P(T) = \frac{ln(t_{set} f_0) k_B T}{K_{AF}(0)(1 - T/T_N)} \tag{3.20}$$

where P_S is the saturation value of the AF order and $f(V_P)$ determines the critical value of the distribution of energy barriers V_P which is determined by the temperature dependence of K_{AF}, the grain volume distribution and t_{set}.

This prediction was confirmed by Vallejo-Fernandez et al. [4,59] where the time dependence of a sample at different temperatures was measured as shown in figure 3.11. A key difference in this experiment to those done previously is that the sample was initially set at a temperature of 498K for a time 5400s in a negative field of -1kOe. This was done to ensure a known initial state of the AF. Once this initial state was set the system was heated to an aligning temperature T_{al} in a positive field of 1kOe for a time t_{al}. At the end of each

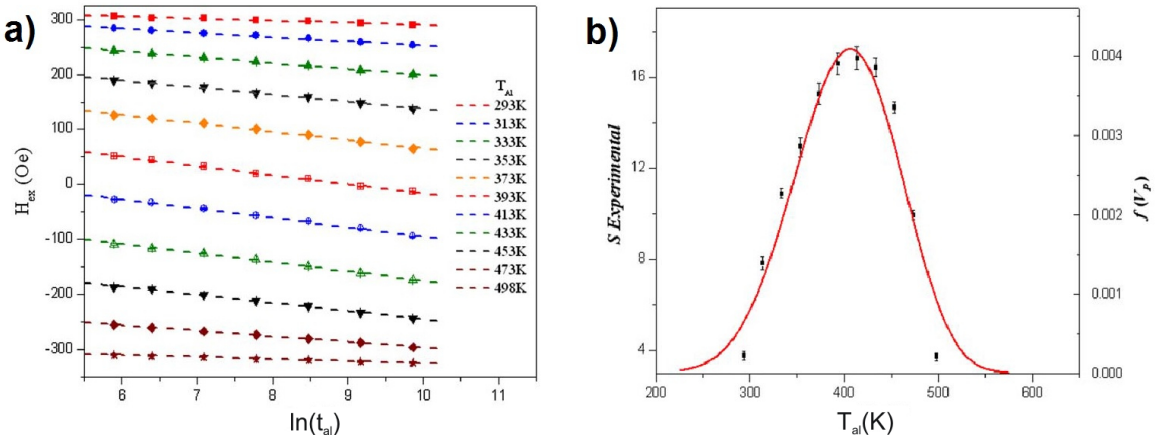

Figure 3.11: Measurement of the a) time dependence of H_{ex} in $ln(t_{al})$ and b) time dependence coefficient S with the calculated values (line) [4, 59].

aligning process the sample was cooled to T_{na} and measured from negative saturation to ensure the training effect was removed. This measurement was done for a wide range of temperatures $(293K \geq T_{al} \leq 498K)$ where it was found that the time dependence of H_{ex} was linear in $ln(t_{al})$ for all values of T_{al}. The value of S was determined from the slope of H_{ex} vs. $ln(t_{al})$ in figure 3.11 a) and plotted with respect to T_{al} the result of which is shown in figure 3.11 b) (points). This was compared to the calculated values (line) as obtained using equations 3.19 and 3.20. Again the fit is excellent with the calculation scaled due to the proportionality sign in equation 3.18.

It is the success of these calculations when compared with experiment that prove the validity of the York Model. However this model only covers the situation of polycrystalline films of grain sizes less than ∼20nm.

3.10 Interfacial Effects

Modelling of the behaviour of the interface in exchange bias systems has had very little success despite the advances made. This is due to the complexity and variation of the interface within a given sample let alone across many. However there are a set of 4 key results that give a strong indication of the possible mechanism of the interface. Again a number of theories have attempted to explain these which will be covered in brief.

3.10.1 Spontaneous Freezing of Interfacial Spins

The first of the results is the low temperature increase in both H_{ex} and H_c. This occurs at T_{ms}<50K where an increase in both H_{ex} and H_c in excess of 100% is observed [46,88,93]. In previous studies where T_N was low, eg. 290K in CoO, this increase could not be distinguished from thermal activation of the AF grains. However as can be seen in figure 3.12 for samples where T_{na}>200K there is a clear plateau between the high temperature thermal activation of the AF and low temperature increase in H_{ex}. This indicates that the lower temperature behaviour is a seperate effect to that of the thermal activation of the bulk AF grains and as such is attributed solely to the interface.

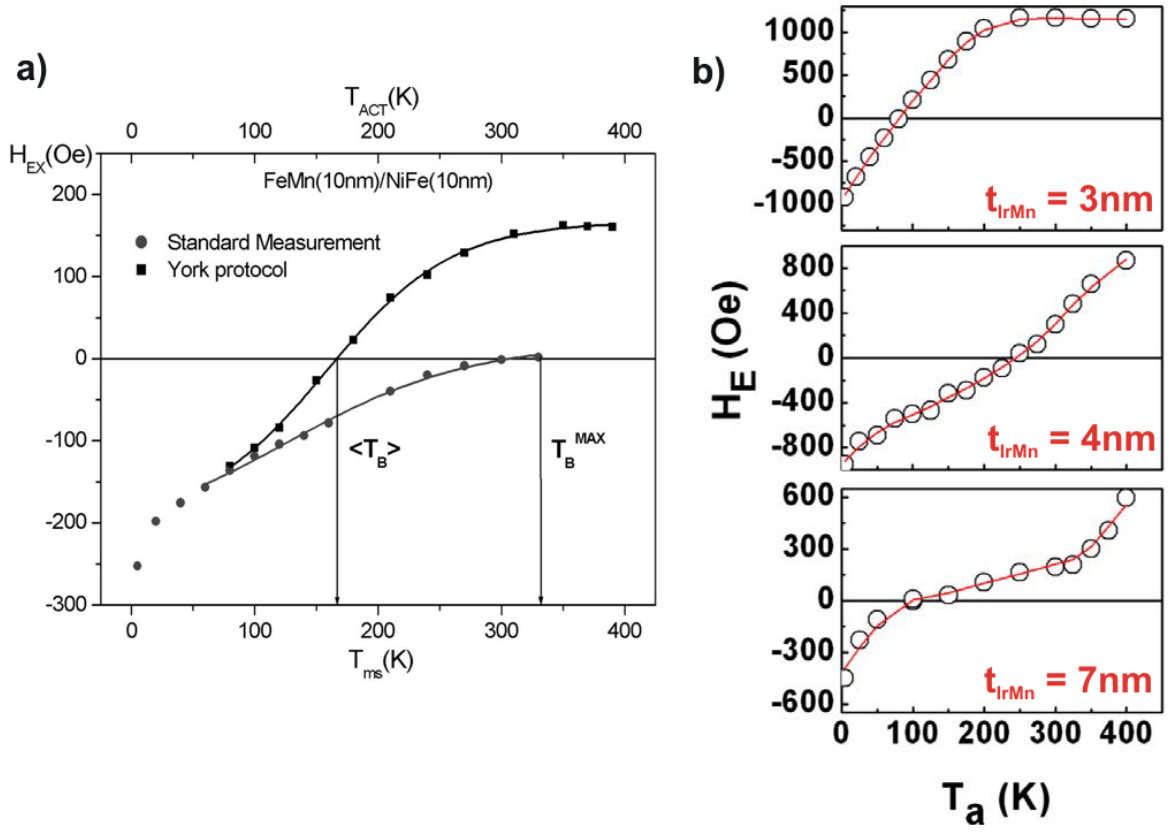

Figure 3.12: Experimental results obtained independently by a) Fernandez-Outon et al. [93] and b) Baltz et al. [46].

Whilst there are a number of theories for this behaviour they all share the similar premise that this transition temperature is due to the freezing of the uncompensated interfacial spins. In the work of Takano et al. [88] they attributed this increase to thermoremanent moments at the interface. These moments were thought to be low freezing temperature spins which exhibited weak coupling to those in the centre of the AF. Takano et al. proposed that it was the density of these spins which was controlled by the structure of the AF that dictated the strength of the exchange bias. From this work Berkowitz et al. came to the conclusion that exchange bias is moderated by the uncompensated interfacial spins. This was further confirmed in the works of Fernandez-Outon et al. [93] and Baltz et al. [46]. Through the use of the York Protocols by Fernandez-Outon et al. the higher and lower temperature behaviours were confimed to be independent. Furthermore the shape of the increase in

H_{ex} with decreasing temperature implies that this effect is not a phase transition but more analagous to that of a blocking temperature distribution in a spin glass [93].

3.10.2 Setting Field Dependence of H_{ex}

The second result is the setting field dependence of H_{ex}. During the setting and field cooling process an increase of ∼20% in H_{ex} is observed when the setting field H_{set} is increased from that sufficient to saturate the F layer, 1kOe in CoFe, to up to 20kOe as shown in figure 3.13. As the orientation of the AF moment is set via direct exchange with with the F layer an increase in field above saturation of the F should have no effect on the order of the AF. Furthermore if $\langle T_b \rangle$ is measured for each value of H_{set} as shown in figure 3.14 no change is observed. This is consistent with there being no change in the setting of the AF grain volume distribution but in the ordering of C^* only. This along with the low temperature dependence of H_{ex} implies that the uncompensated interfacial spins form clusters which order ferromagnetically. O'Grady et al. [4] proposed that this ordering follows a Langevin

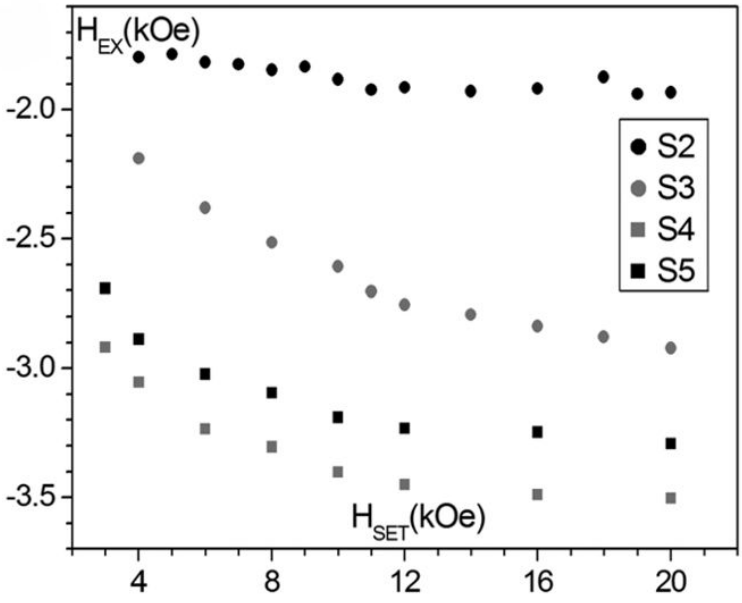

Figure 3.13: Experimental results showing the setting field dependence of exchange bias [25].

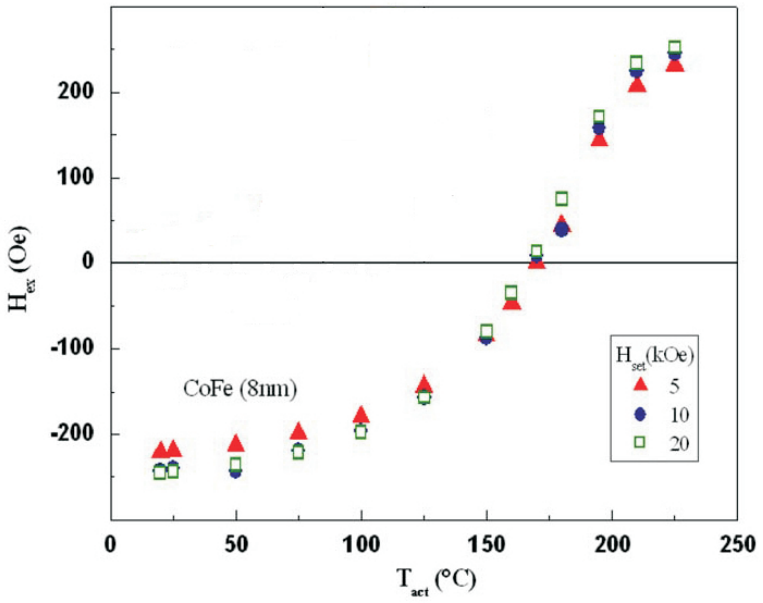

Figure 3.14: Experimental results showing the change in the distribution of T_b with setting field [25].

function $L(a_L)$ of the form

$$H_{ex}(H_{set}, T_{set}) \propto H^i_{ex} L_{a_L} \quad \text{with} \quad a_L = \frac{N\mu_B(H_{set} + H^*_s)}{k_B T_{set}} \tag{3.21}$$

with the assumption that the coupling between the F and AF layers is linearly dependent on the order of the interfacial spins. In this equation H^*_s is the exchange field experienced by the interfacial spins and N is the number of spins within the cluster. The values of both H^*_s and N are unknown and difficult to measure. If the diameter of these clusters tracks that of the AF grains than it can be assumed that they will contain in the order of 10-50 spins however this will vary greatly depending on interface roughness and furthermore could be H^*_s dependent. The value of H^*_s itself is difficult to ascertain as it will depend on the coupling of the F layer to the cluster, AF to cluster and cluster to cluster exchange interactions the strengths of which are unknown. Furthermore the F to cluster and cluster to cluster dipole interactions will play some part in the ordering of the system as shown by the H_{set} dependence of H_{ex}. Although this conceptual model may explain the effect of the interface on H_{ex} the mechanism through which H_c increases is not clear.

3.10.3 The Trilayer Experiment

For the third experiment a trilayer of CoFe(12)/IrMn(5)/CoFe(8) (nm) was deposited and thermally activated following the York Protocols [94]. The sample was initially set in a positive field sufficient to saturate both F layers at a temperature of 483K. A negative field of -150 Oe sufficient to saturate only the thicker F layer was then applied and the sample heated, field cooled and measured with increasing temperatures up to 483K. The results of this measurement are shown in figure 3.15 where there is only thermal activation of the thicker F layer until a critical temperature of 414K is reached.

These results show clearly that the state of the order at the interface is not only controlled by the exchange interaction with the F layer but that it is independent of the bulk of the AF. Furthermore the results showed there to be a distribution of energy barriers for the interfacial spins. It was this distribution that leads to variations in the exchange coupling across the interface.

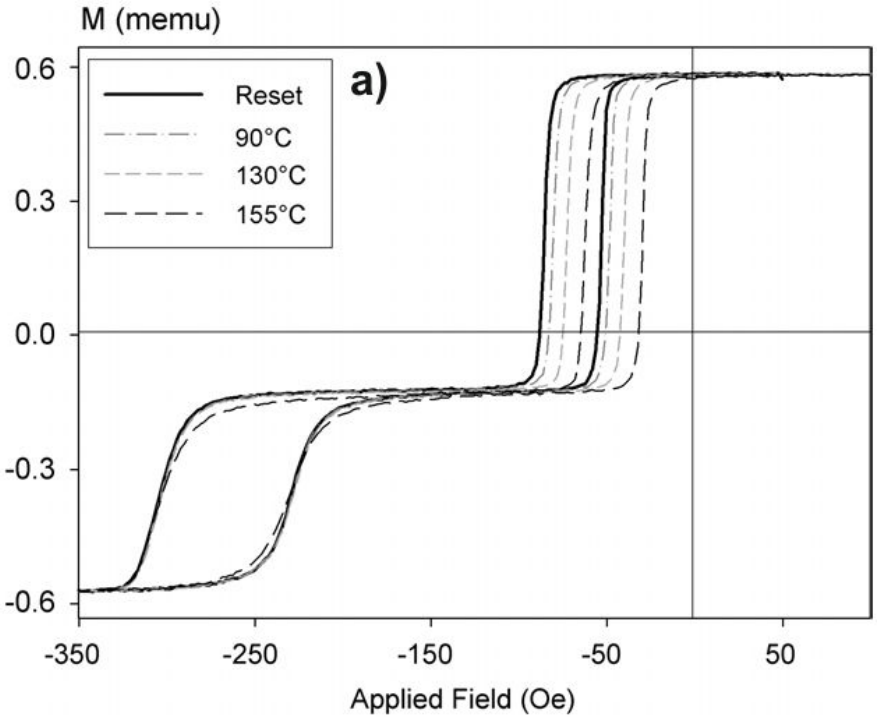

Figure 3.15: Trilayer experiment showing the independence of the interface during thermal activation [94].

3.10.4 The Training Effect

The fourth experiment involves the training effect and the well known increase in H_c. As the training effect is a change in the first coercivity on reversal from positive to negative saturation its behaviour could provide some clues to that of H_c. Hoffmann [95] proposed that the training effect was due to competing easy axes in the AF. This lead to the AF sublattices aligning perpendicular post-annealing. Upon reversal a spin flop process occurs as the AF moments align anti-parallel leading to a change in the coupling through the course of the measurement. This process is shown schematically in figure 3.16. This thought is similar to that of Baltz et al. [46] where the increase in H_c is thought to be due to thermally active AF grains lagging behind the F layer. Both of these theories require that some portion of the AF be active over the course of the measurement. As was demonstrated by the York model this cannot occur when measuring at T_{na}.

A variation of the trilayer experiment was carried out by Kaeswurm et al. [27]. In this work it was hypothesised that if the interfaces were truly seperate then the training effect could be independently 'triggered'. The sample was set as in the previous trilayer experiment and from positive saturation the field was reversed to -300 Oe sufficient to reverse the thicker F layer which is shown by the black line in figure 3.17. The sample was then brought back to positive saturation and two loops measured with a negative field sufficient to reverse both layers, the grey and dotted lines respectively. It was again found

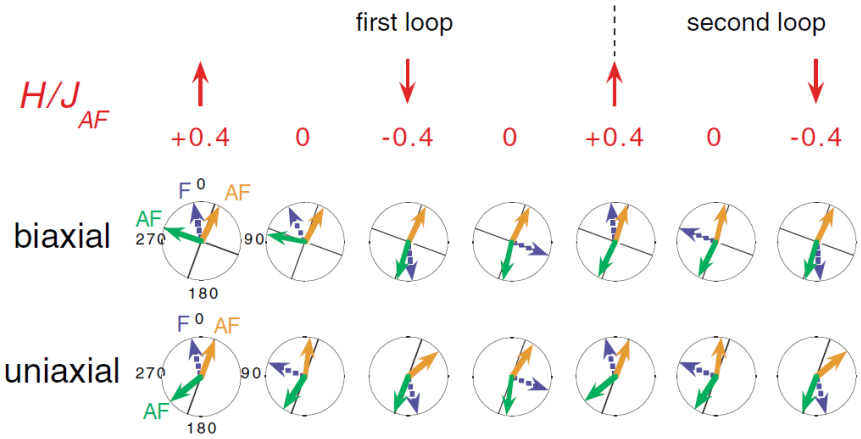

Figure 3.16: Schematic showing the spin flop process during the first and second loop where the solid lines indicate the AF magnetic anisotropy axes [95].

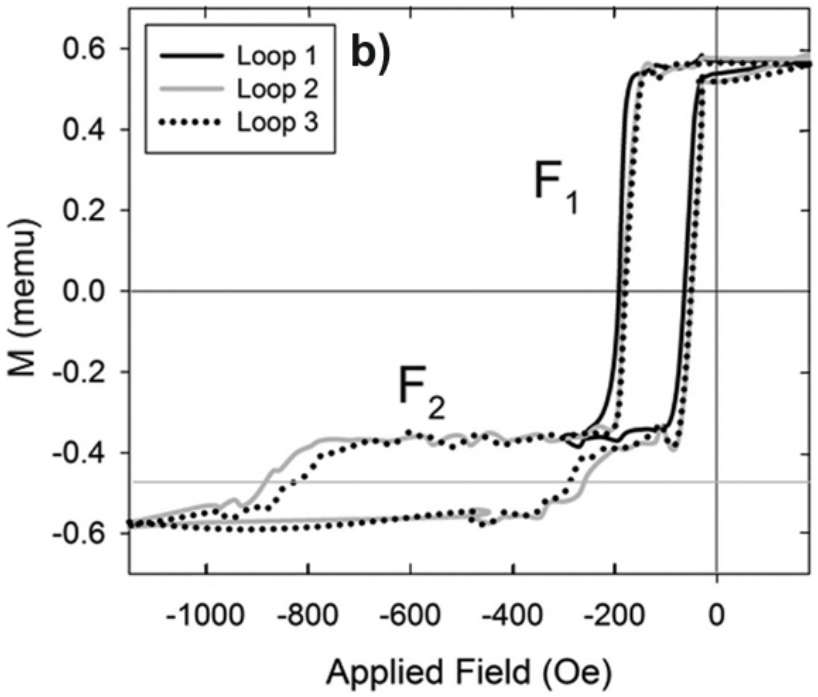

Figure 3.17: Trilayer experiment showing the controlled 'activation' of the training effect [27].

that the training effect occured only once the F layer had reached negative saturation to that at which it was originally set. This proves that not only do the interfacial spin clusters behave as independent entities but also the training effect is solely due to changes at the interface. From this work it could also be hypothesised that the increase in H_c is a solely interfacial effect related to the interfacial 'stiffness'.

3.10.5 Outstanding Issues

Using the above results a conceptual model may be formed. In this model the interface consists of frustrated spins which interact with their neighbours to form clusters. These clusters are thought to behave similar to that of superparamagnetic particles the ordering of which affects the stiffness of the coupling between the F and AF a schematic of which is shown in figure 3.18.

Despite the large number of results certain key measurements are still lacking. If the

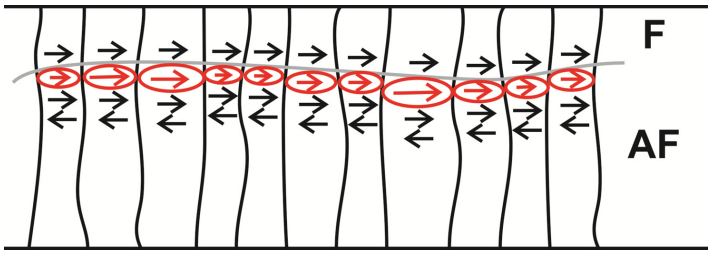

Figure 3.18: Schematic of the conceptual spin cluster model

interface does indeed behave as that of superparamagnetic particles no significant measurement can be made unless they are carried out at temperatures sufficiently low to ensure the clusters are blocked. Furthermore the setting process of the AF via the F layer is not fully understood as well as the effect of texture on the interface.

The aim of this work is to attempt to provide some answers in regards to both the setting process and effect of texture on the interface. Furthermore as the lateral dimensions of read heads approach that of less than 50 grains the effect of local variations in orientation and interface will become increasingly important. As such a study into the change in H_{ex} and T_b in sub-100nm elements has been carried out.

3.11 Strong Domain Wall Pinning Model

At the onset of this project the York Model of exchange bias had been broadly accepted for explaining most known phenomena as it had been used by Seagate and Western Digital to redesign their read head design. However by definition the model is restricted to that of single domain AF grains that reverse through coherent rotation. As detailed throughout chapter 3 there are significant bodies of work on single crystal films and epitaxially sputtered large grain films. Vallejo-Fernandez et al. [96] produced an extension to the York Model in an attempt to interpret the data and in part to provide a comprehensive understanding of defects and impurities in thin films where the structure is unlikely to be that of single domain AF grains.

The SDWP model is based on a similar concept to that of the domain state model. In it the AF can form domains the walls between which become pinned by defects in the

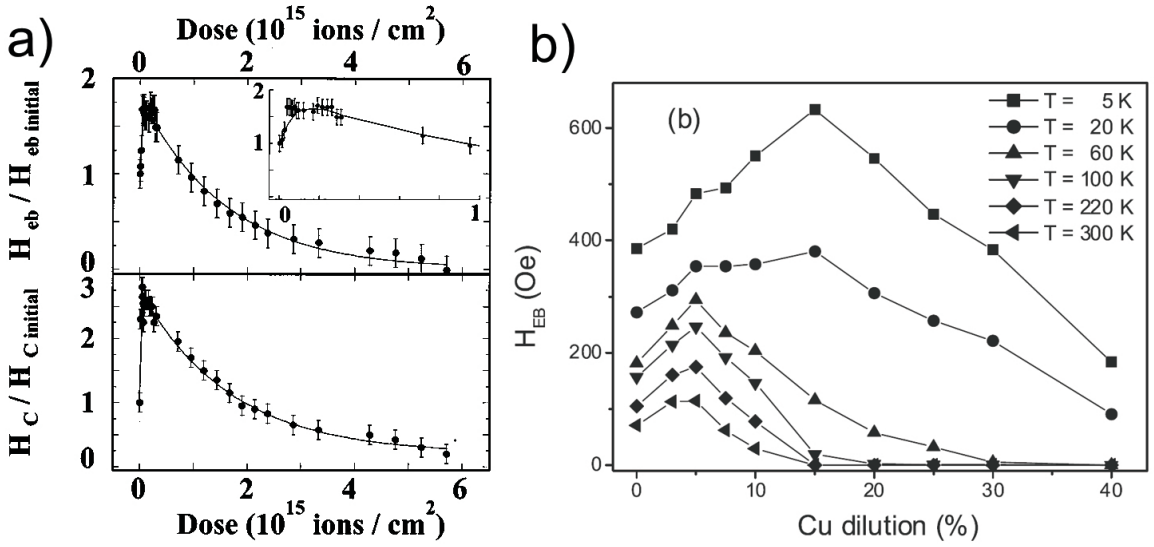

Figure 3.19: Results for a) He ion doping and b) Cu doping of exchange biased bi layers [97, 98].

film. This hypothesis was formed following the works of Mougin et al. [97] and Fecioru-Morariu et al. [98]. In the former it was found that when an exchange biased film was irradiated with He ion radiation H_{ex} increased by 100% with increasing dose from 10^{13} to 0.3×10^{15} ions/cm^2. However with higher doses approaching 5.5×10^{15} ions/cm^2 H_{ex} decreased to zero as shown in figure 3.19 a). In the latter copper dilutions were added to the AF layer during deposition. The change in H_{ex} with the dilution percentage was found to be dependent on the measurement temperature however the trend of an initial increase and then decrease was still observed as shown in figure 3.19 b). In the work of Aley et al. [99] a rapid decrease in H_{ex} was seen with increasing copper dilution which appears to be in conflict with the previous two works. However in the work of Aley et al. the AF grain size was between 5.7 and 6.4nm whilst in the work of Fecioru-Morariu et al. the diameters ranged from 43-65nm. This led to the development of the SDWP model where defects in the AF lead to the formation of increasingly smaller domains down to the critical size for a single domain entity.

In the SDWP model both the copper and He ion dopants were considered to be defects in the AF and therefore equivalent. A key difference of the SDWP model is that multiple

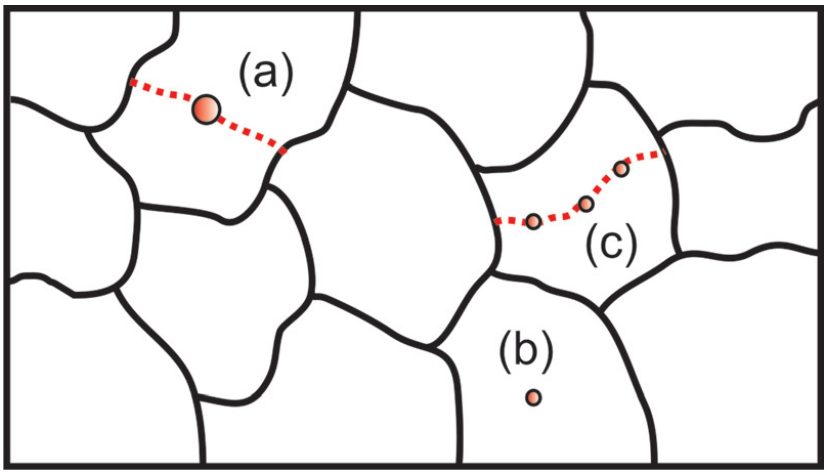

Figure 3.20: Schematic of the AF microstructure [96, 100].

domains will form only in grains above a certain critical diameter unlike in the domain state model where creation of domains is dependent on defects to lower the wall formation energy. The critical diameter for the transition from a single to multi-domain grain is currently unknown however in the case of the SDWP model this was assumed to occur at 20nm. The domain wall width in an AF is also not known however it is thought to be thin compared to that of in a F and also field dependent. In the case of the SDWP model the domain wall width is not considered [96, 100].

In the SDWP model the single domain grains behave as in the standard York model where thermal activation occurs over an energy barrier. The multi-domain grains instead reverse via domain wall processes which leads to a reduction in their contribution to H_{ex}. Defects are then added to the system with a distribution of pinning strengths which is assumed to be lognormal in shape. A schematic of the AF microstructure is shown in 3.20. With the addition of these impurities three situations occur. The first (case (a)) is when an impurity has a pinning strength $>30k_BT$ which is able to pin a domain wall in the AF. This leads to the grain breaking into smaller domains which may not be large enough to support formation of further domains. The second (case (b)) is when the pinning strength of the impurity is $<30k_BT$ and so is not able to pin a domain wall therefore having no effect on the magnetic structure of the grain. The final (case (c)) occurs when there are multiple impurities of pinning strength $<30k_BT$ but with a total $>30k_BT$. This leads to pinning of the domain wall and formation of smaller 'grains' as in case (a) [96, 100].

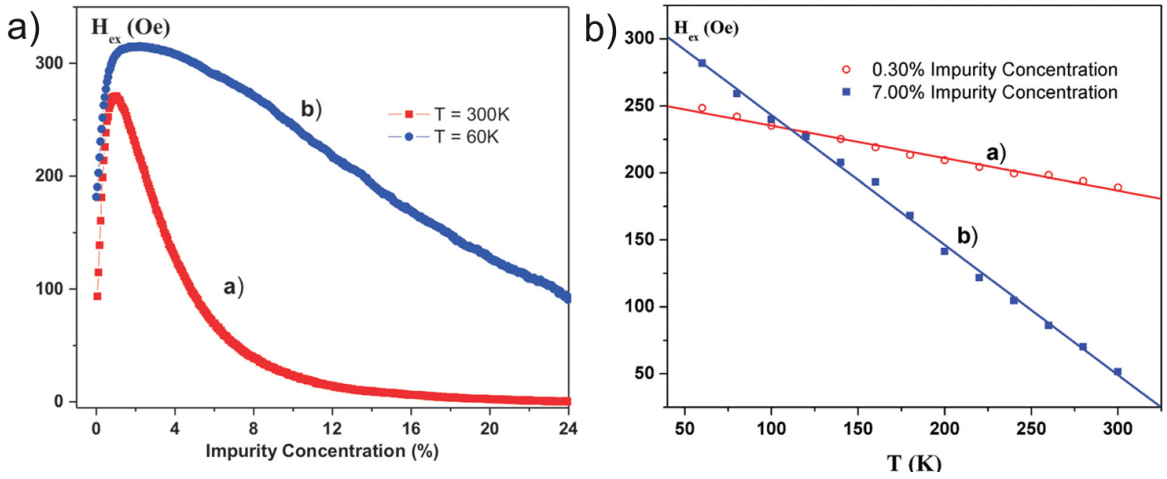

Figure 3.21: Temperature a) and impurity dependence b) of H_{ex} calculated using the SDWP model [96, 98].

The value of K_{AF} was expected to decrease with increasing concentration of impurities due to the loss of crystallinity. In the case of the SDWP model when the concentration of impurities exceeds 5% K_{AF} is reduced by 50% as this increases above 30% K_{AF} further reduces to 10% of the initial value [96, 100]. Values were taken from the experimental work as shown in figures 3.19 a) and b). Using these Vallejo-Fernandez et al. was able to predict the results using the SDWP model as shown in figures 3.21 a) and b). The fit of the theory to the experiment results is excellent. In this explanation at low concentrations the large multi-domain grains are broken up into smaller single domain grains which above a certain critial diameter are thermally stable due to the pinning of the domain wall. With increasing concentration of defects these pseudo-grains break up into smaller and smaller grains and so become thermally active which leads to a decrease in H_{ex}. This is reflected in the experimental results for both temperatures studied.

Although previous theories have successfully modelled each of these effects independently no single model has managed to accout for as many effects as the York and SDWP models. It is for this reason that the York Model is solely used in this work. A current flaw with the model is that it only applies to temperatures above 50K. This is due to the unknown behaviour of C^* which is a partial aim of this work.

Chapter 4

Sample Fabrication

The use of magnetic materials is far reaching from fundamental research to widespread applications in commercial devices. As such there are a large number of methods required for creating the desired structures all of which require control down to the atomic scale. This is easily split into two categories: fabrication of thin films and the patterning of these films.

4.1 Methods of Thin Film Deposition

Metallic thin films vary from single crystal, epitaxially grown metals to polycrystalline alloys of nanometer scale roughness. Such a wide range of films is due to the almost equally wide range of deposition techniques. At the beginning of the spectrum there is Molecular Beam Epitaxy (MBE) where metals are sublimated via electron beam or high temperatures. For true MBE, Ultra High Vacuum (UHV) of $<1\times10^{-9}$mbar are required. A UHV environment is needed to prevent contamination due to the very low deposition rates (<0.1nm/s) which limits the method's application in industry [101].

A further issue with MBE grown films is the mechanism of magnetisation reversal. As the films are single crystal the reversal processes are domain wall driven and thus dictated by pinning due to film defects e.g. dislocations or substrate roughness. Such defects are prohibitively difficult to control leading to an undesirable unpredictability in any commercial

device. Normally MBE grown films would be used for single crystal soft materials. However sputtering, which will be covered in detail later, produces sufficiently soft materials for application.

At the other end of the spectrum there is Pulsed Laser Deposition (PLD) where alloys are deposited through ablation by laser. A particular advantage of PLD is the ability to deposit oxides as well as alloys whilst maintaining the stoichiometry of the target material. PLD has far faster depositon rates ($>$10nm/s) than that of MBE. However micron sized paticles of ablated material deposit on the film surface leading to contamination and wide grain size distributions which limits its viability for application in industry [102].

Near the middle of this spectrum is Ion Beam Deposition (IBD) which is similar to MBE however the electron gun is replaced by an external ion source. Due to the requirement of a gas for generation of the ions the operating pressure is typically 1×10^{-4} to 1×10^{-5}mbar. A common form of IBD is sputtering. Sputtering occurs when a solid target is bombarded with high energy ions which leads to high deposition rates (1-10nm/s) and atomically flat growth of high purity polycrystalline materials. It is this method which is predominently used in industry and therefore solely used for the samples produced in this work [103].

4.1.1 Sputter Deposition

There are several types of sputtering system that are used for the deposition of thin films. DC diode sputtering was the first system developed [103]. In this system a DC voltage of several kilovolts with a series resistance of 1-10kΩ is applied across a pair of planar electrodes. The chamber containing these electrodes is kept at an Ar^+ pressure of 0.1 mbar leading to the initiation of a glow discharge. The plasma facing side of the cathode is covered with the target material whilst the other side is water cooled. The Ar ions generated in the glow discharge are accelerated towards the cathode causing sputtering of the target material and deposition on the substrates which are placed on the anode [103].

If the metallic target of the DC sputtering system is replaced by an insulator the glow discharge cannot be sustained due to the buildup of a surface charge of positive ions. By changing the power supply to be AC the glow discharge can be maintained. In an AC diode

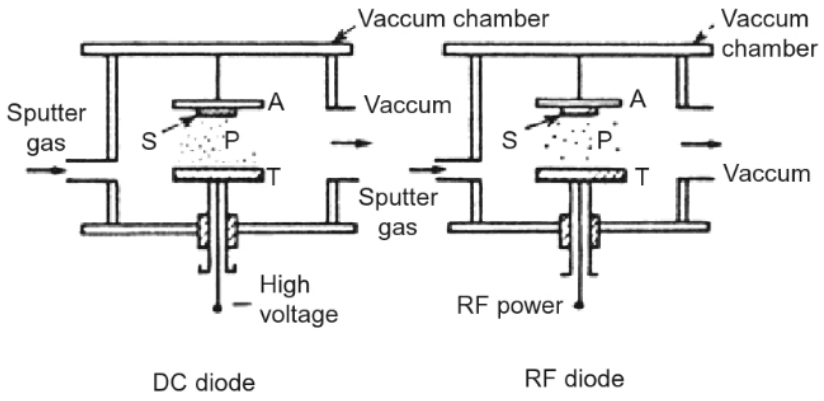

Figure 4.1: Schematic diagram of DC and RF diode sputtering systems [103].

sputtering system the cathode current density i_s is given by

$$i_s \cong CdV/dt \tag{4.1}$$

where C is is the capacitance between the discharge plasma and the target and $dVdt$ is the time variation of the target surface potential. This shows that an increase in the frequency of the applied voltage leads to an increase in the cathode ion currents. In practice the frequency used is 13.56MHz which leads the method to be called RF sputtering [103]. It is important to note that the RF electric field increases the collision probability between the secondary electrons and gas molecules allowing for a decrease in the required Ar pressure to 1×10^{-3}mbar. A schematic diagram of both DC and RF sputtering systems is shown in figure 4.1 [103].

It was the desire for low-pressure sputter deposition which led to the development of the magnetron. It was found that with the addition of a strong transverse magnetic field (3-10kOe) cathode sputtering was enhanced. This was due to an increase in the ion current density at the cathode by up to an order of magnitude with an associated increase in depostion rate. This increase in the plasma density is due to electrons in the plasma spiralling around the field lines leading to further ionisation events. Furthermore Ar pressures of only 10^{-5}-10^{-3} mbar were required to initiate a glow discharge [103]. The lower operating pressure meant that the sputtered particles could travel across the discharge

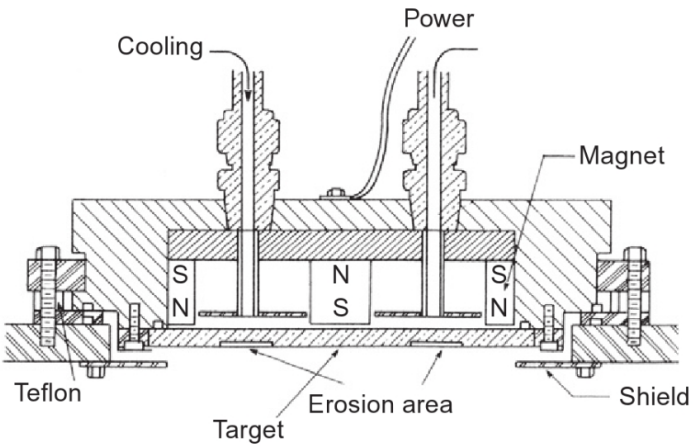

Figure 4.2: Schematic diagram of commercialised magnetron cathodes as produced by Canon Anelva [103].

space without collisions giving a deposition rate R_{dep} of

$$R \cong k\omega_0/t \tag{4.2}$$

where ω_0 is the amount of sputtered particles, k=1 or k=r_a/r_c depending on use of a planar or cylindrical sytem respectively and r_c and r_a are the cathode and anode radii. Generally deposition rates of the order of 1-10nm/s are observed. This combination of high deposition rates at low pressures has led to magnetron sputtering as being the deposition method of choice for industry [103]. An example of a commercialised magnetron cathode is shown in figure 4.2.

However magnetron sputtering has a number of limitations. If the desired target is magnetic the field lines of the magnetron are confined within the material. This gives the requirement of very thin targets when sputtering from a magnetic material e.g CoFe. Furthermore the glow discharge generated is concentrated in the region of high magnetic field from the cathode magnets. This leads to the creation of a circular glow discharge which gives non-uniform etching of the target material often referred to as a "racetrack". This severly limits the lifespan of the cathode target [103]. In order to overcome this prohibitively complex magnet configurations are required. Due to the deposition of large quantities of magnetic materials, as well as the use of $IrMn_3$ which is of high value, a permutation of the magnetron system has been used in this work. This system is called High Target Utilisation

Sputtering (HiTUS) [104].

4.1.2 High Target Utilisation Sputter Deposition

The majority of the problems associated with traditional diode/magnetron sputtering is the requirement of the target to be on the cathode in the region of plasma generation. By generating the plasma remotely the deposition conditions can be varied regardless of target material [105].

In HiTUS deposition the gas plasma is generated in a side arm through the interaction of the electrons with a 13.56 MHz RF field which is inductively coupled from a 3-turn antenna. A co-axial DC magnetic field of 50 Oe is applied so that a portion of the electrons generated at the antenna location are accelerated towards the sputter chamber. These have sufficient energy to be at or near the optimum required for sputter gas ionisation. The chiral motion of the electrons about the magnetic field lines leads to long path lengths resulting in a 'cascade' electron generation process. This leads to a continuous 'tube' of plasma generation leading into the sputter chamber. This plasma 'tube' is easily steered onto the targets using a secondary DC magnetic field of 500Oe [105].

The plasma ions generated by the side arm are of an energy not sufficient to cause

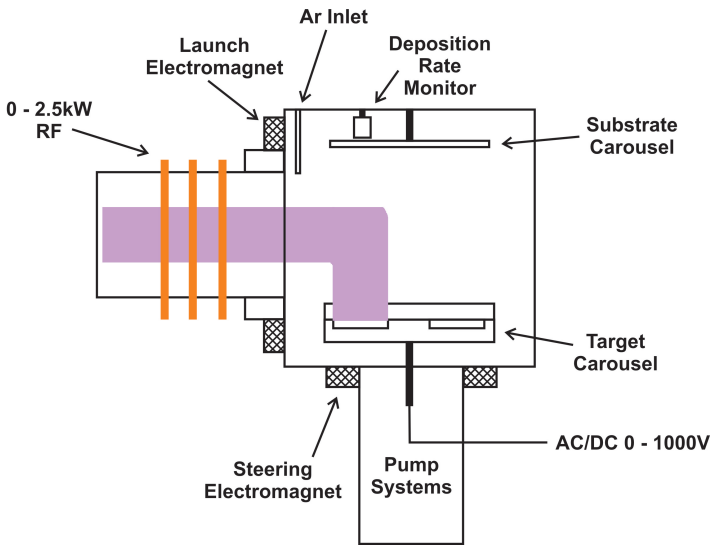

Figure 4.3: Schematic diagram of the HiTUS chamber.

sputtering of the target. This is solved through application of a DC or RF bias of 1-1000V on the target. The resulting electric field gives the Ar^+ ions sufficient energy for sputtering to occur. As this bias voltage is not required for the generation of the plasma it can be varied without affecting the plasma density. Furthermore the plasma density ($<10^{12}$ cm^{-3} to 10^{14} cm^{-3}) can be varied independently of the target bias voltage through control of the RF power (up to 2.5kW) and the operating pressure (1.3×10^{-3} to 4.0×10^{-2} mbar). This allows for control of the deposition rate via the bias voltage for a given plasma density [104]. A schematic of this system is shown in figure 4.3.

The lack of a required magnetic field under the target has two implications: Firstly it allows for the use of thick ferromagnetic targets. Secondly as over 90% of the target surface is sputtered the composition can be varied by drilling holes in the target and adding pegs of high purity metals. This system developed in York allows for rapid variation of composition, grain diameter and crystal quality [44]. An example of a standard and composite HiTUS target is shown in figure 4.4.

The geometry of the system allows for a flexible array of substrates to be used. Firstly since there is 30cm gap between the substrate and target there is no re-sputtering from the deposited substrates. Furthermore this spacing means that there is sufficient intermixing of sputtered material so that multiple different substrates can be deposited upon simultaneously with identical material. This allows for deposition on both silicon substrate and carbon coated copper TEM grids, eliminating the need for sample thinning for structural analysis. Secondly as the substrates are far from the plasma the operating temperature is very low at $< 100^{\circ}\ C$ [104, 105].

Figure 4.4: Image of a standard (left) and composite (right) HiTUS target.

Layer	Thickness (±0.5nm)	Deposition Rate (Å/s±0.5%)	Ar Pressure (mTorr)
Cu	5	2.3	3.5
NiCr	6	0.8	3.5
$IrMn_3$	10	1.5	3.5
CoFe	5	1.1	3.5
Ta	5	0.6	3.5

Table 4.1: Summary of HiTUS deposition conditions.

The HiTUS system used in this project contained 8 targets and 6 substrate positions. This allowed for the growth of up to 6 samples of varying structure, grain diameter and composition without breaking vacuum. The thickness of the deposited films were measured using a water cooled quartz crystal oscillator deposition rate monitor with a thickness accuracy of 0.5%. The deposition rate monitor was placed within 5 cm of the substrate. These thicknesses were confirmed via X-ray Reflectivity (XRR) measurements along with measurements of the interfacial roughness.

This flexibility allowed for selection of the bias voltage and Ar pressure in order to optimise the layer structure. A series of samples were deposited for the basic layer structure of X(x)/IrMn(10) (nm) where X was Cu and NiCr of thicknesses x=5 and 6nm respectively across a range of bias voltages from 200-900V and Ar pressures 1-4mTorr. The ideal RF power and bias voltage was found to be 1.75kW and 900V respectively with the remaining conditions shown in table 4.1.

4.2 Nanofabrication

Over the past decade the bit size in a HDD has decreased down to a bit width and length of 50 and 20nm respectively. In order to resolve these bits the read head must be of comparable dimensions. Furthermore for Magnetic Random Access Memory (MRAM) to be competitive the storage stack must be <50nm in diameter. This requires the ability to fabricate large arrays (>8 in) of these nanostructures accurately. On top of the technical requirements the

method of choice must be economically viable.

The wavelength of light used in photolithography is that of the extreme Ultraviolet (UV) range from 440 - 130nm. Despite this apparent limitation photolithography is still used for the fabriction of the current generation of semiconductor devices with a node size of 24nm using near field optics. However the size, density and proximity of structures required for magnetic data storage is still beyond the capabilities of modern production line photolithography. Furthermore the current method of imprinting the lithographically defined pattern into the metallic film is ion beam etching. Etching causes an array of damage to the structures from ion implantation [23], grain growth [24] and edge damage [28, 46, 106]. These issues have lead to the rapid development of a number of different methods of patterning high density, highly regular, sub 50nm metallic structures.

One of the more exotic methods of fabrication is block copolymers. Block copolymers consist of two or more different monomer units strung together into long chains. The immiscibility of the monomers causes them to self-organise into highly ordered lattices with unit cells between 10-100 nm. An example of this involving a chaining of polystyrene and Polymethylmethacrylate (PMMA) (PS-b-PMMA) was used by IBM in 2004 to fabricate a flash memory with 20nm Si crystals [107]. This method has also been used by HGST in an attempt to produce bit patterned media [108]. Due to the ability to produce small features ($<$20nm) at high densities ($\sim$1011/cm^2) this method is being actively researched. However polymer self-assembly is limited to a set of pattern geometries restricting its applications [107]. Standard lithography particularly electron beam lithography has been the sole method used in this work.

Lithography involves the transfer of a master pattern onto the surface of a hard material e.g. silicon substrate. This master pattern can range from a physical object such as chrome on a quartz mask to a Computer Aided Design (CAD) written directly. This pattern is transfered into a photo or electron sensitive resist material using the approriate radiation. The lithographic process is a varied and complex one depending on the required final pattern. As such the focus of this section will be the process required for the fabrication of large arrays of sub 500nm dots using e-beam lithography.

4.2.1 The Lithographic Process

The lithographic process is multi-stepped and dependent on the final desired structure. The initial and vitally important step is the removal of contaminants from the substrate surface. Contaminants range from solvent stains to dust/smoke particles. To reduce particulate contamination the entire lithographic process is carried out in a clean room. In a clean room the number of particulates, temperature ($\pm$0.1°C), humidity (0.5%), air pressure, vibration and lighting are carefully controlled. In the case of this work a class 100 clean room was used where the number gives the amount of particles of diameter 0.5μm or greater per cubic foot [107].

To remove solvent and oil stains the substrate is sonicated in an acetone bath and then sequentially rinsed in 2-Propanol (IPA) and Deionised (DI) water. To remove water bound to the substrate surface it is given a dehydration bake at 180°C for 30-60mins and cooled in a dry environment. To remove any remaining hydrocarbons the substrate is placed in a Ultraviolet Ozone (UVO) cleaner where it is exposed to UV radiation of wavelength 184.9 and 253.7nm. The residual hydrocarbons are excited by the UV radiation to produce molecular oxygen (184.9nm) and ozone (253.7nm). The products of this excitation react with the oxygen to form more simple molecules which desorb from the substrate surface whilst the ozone is continually formed and destroyed. After this the substrate is ready for deposition of the resist [107].

There are a number of methods for depositing resist however in the case of this work spin coating was used. The first step is the dispensing of the resist onto the wafer which is held onto a vacuum chuck. The substrate is spun at 500rpm during dispensing enabling the spread of the liquid over the surface. Once dispensed the substrate is spun at 1500-6000rpm for from 10s to a few minutes until the desired resist thickness is obtained. The combination of spin speed and time is dependent on the resist/substrate used and the thickness desired. The final polymer thickness t_{res} obtained after spinning is given by the empirical expression

$$T_{res} = \frac{K_c C^{\beta} \eta^{\gamma}}{\upsilon^{\alpha}} \tag{4.3}$$

where C_P is the polymer concentration in g/100ml of solution, η is the intrinsic viscocity, ω_v is rpm and K_c is the overall calibration constant. Once the three exponential

factors $\alpha/\gamma/\upsilon$ have been measured t_{res} can be predicted for different molecular weights and concentrations of a given polymer/solvent system. The thickness of the photoresist is a critical parameter for successful and uniform pattern transfer. After the resist is spun it must have a uniform thickness of $\sim$1μm with a reproducibility of $\pm$1nm whilst being chemically isotropic. This is vital for accurate pattern sizes and development times [107].

The final step before exposure of the resist is a soft bake at 75-85°C. This is done to remove any remaining solvent in the resist as well as any stresses in the film. At this point the resist coated substrate can then be placed into the exposure system. The substrate must be aligned to the mask with a precision a fraction of that of the minimum feature size. Once aligned the sample is exposed using the desired radiation for a length of time required to deliver a sufficient dose D_e (J/cm^2) to cause one of two reactions: polymer chain scission or cross-linking. It is these reactions that are the key difference between a positive and negative resist the details of which will be discussed in the following section and are shown schematically in figure 4.5 [107].

After exposure the resist must be developed. The process of development is the dissolution of the unpolymerised resist that makes up the latent image formed during exposure and turns it into a relief image that acts as a mask for any future additive or subtractive

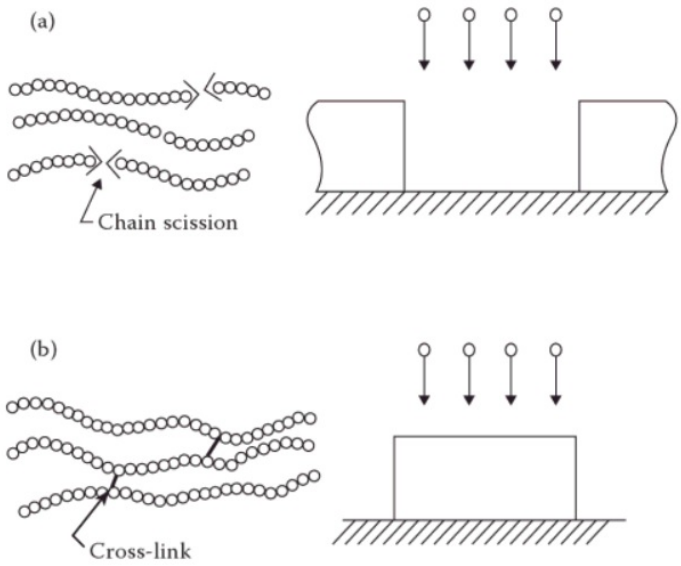

Figure 4.5: Schematic of a) polymer chain scission (positive resist) and b) cross-linking (negative resist) [107].

steps. The type of developer used depends on whether a negative or positive resist has been used. Typically a positive resist is developed in an aqueous alkaline solution whilst a negative resist will be developed in an organic medium. The final step following development and before any material can be deposited is a postbake. During postbaking the patterned sample is heated to 120°C for a long period of time (e.g. 20mins). This removes any residual solvent or developer. Furthermore the process anneals the resist improving interfacial adhesion where damage may have occured due to developer penetration or resist swelling. At this point the sample is now patterned and ready for the deposition of material.

4.2.2 Resists

The choice of resist whether it be positive, negative, single or double layer all play an important part in both the final resolution and quality of the end structure. The main components of a resist are a polymer and a casting solvent. The polymer is what changes structure during exposure whilst the solvent facilitates spin coating of the resist onto the substrate [107]. As mentioned previously it is the reaction during exposure that differentiates a positive from a negative resist.

When exposed to suitable radiation a positive resist undergoes scission of the main and side polymer chains. This leads to the exposed resist becoming more soluble in a developing solution e.g. NaOH. As such when the metallic film is deposited on the patterned resist it is the material in the cleared trench that makes the desired structure [107]. Material deposited on the resist that has not been dissolved during development is removed in a process called lift-off. During lift-off the patterned substrate with deposited film is put into a solvent that will dissolve the remaining resist e.g. acetone. Consquently when this resist is removed any material deposited on top is taken with it leaving the desired structure. An example of when lift-off fails is shown in figure 4.6a).

One of the major advantages of positive photoresists is that as the process of exposure is scission the obtainable resolution is very good. However the process of lift-off leads to a number of problems. During film deposition material will deposit on the walls of the developed trench. This side wall growth gives a minimum size of the desired structure limited to that of two times the thickness of the deposited film. This is because the thickness of the material deposited on the walls is of the same scale as that of the trench causing it to close

up. Another issue of side wall growth is known as 'bunny ears'. This occurs during lift-off when the side wall material remains on the patterned structure leading a rim to form. An example of this can be seen in both figures 4.6a) and b).

There are two methods for overcoming these issues. The first is to use a double layer resist in which a first layer is spin coated and soft baked to be followed by the coating of second layer. The bottom resist will require much less exposure than that of the top layer. This leads to the top layer defining the structure whilst the bottom layer is 'undercut' preventing side wall growth and the formation of 'bunny ears'. An example of structures made using a double layer resist are shown in figure 4.6c).

The second method is to use a negative resist with etching to create the structures. When a negative resist is exposed the polymer is strengthed by random cross linkage of main chains or pendant side chains. This leads to the exposed resist becoming less soluble in the

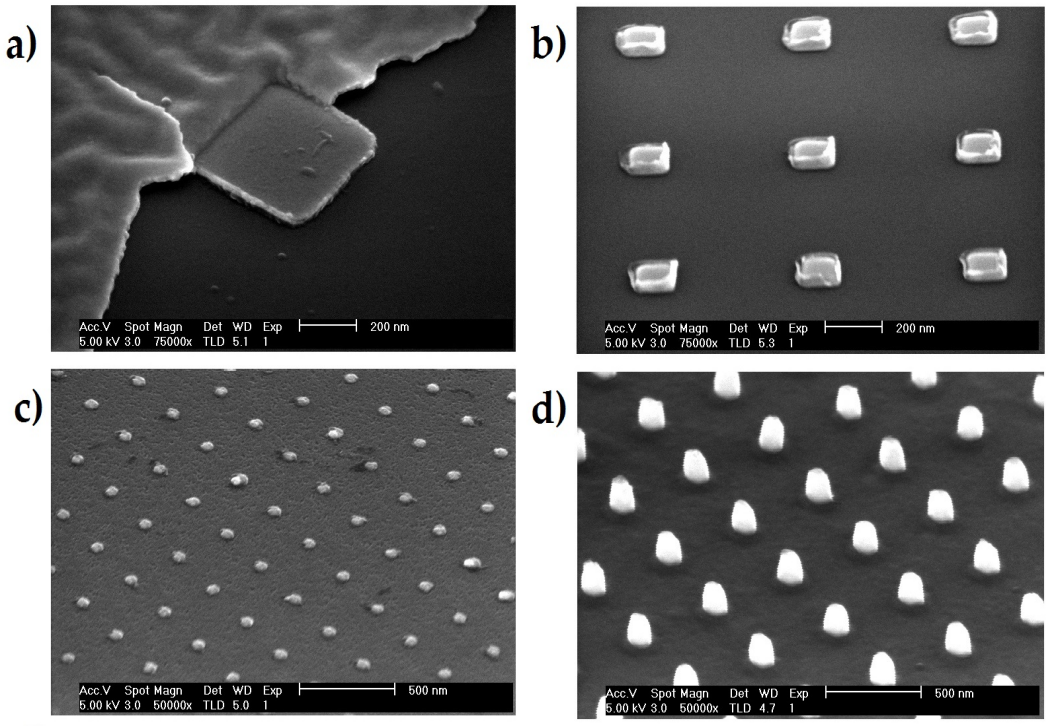

Figure 4.6: Example SEM images of a) poor lift-off for a single layer resist, b) 'bunny ears' formed due to lift-off from a single layer resist, c) lift-off using a double layer resist and d) an etched negative resist.

developing solution e.g. IPA. In this case the metallic film will have been deposited on the substrate before spinning and exposure of the resist. The patterned sample is then etched using a plasma where the remaining resist protects the metallic film underneath. After etching it is only the protected film that remains leaving the desired structure. An example of an etched film can be seen in figure 4.6d) where the white pillar is the protective resist 'cap'. One of the major disadvantages to negative resists is that the resolution is limited by the chain length of the polymer used. Furthermore etching can cause significant film damage due to ion implantation [23], grain growth [24] and edge damage [28, 46, 106].

4.2.3 Electron Beam Lithography

In e-beam lithography exposure is carried out using what is essentially a modified Scanning Electron Microscope. During exposure an electron beam of a given diameter is scanned in a raster across the resist exposing only the areas as defined in the programmed CAD. The total exposure time t_{exp} for a given area A_{exp} on the substrate is given by

$$T_{exp} = \frac{QA_{exp}}{I} \tag{4.4}$$

where I is the beam current and Q is the charge density or dose (D_e). Therefore to obtain short exposure times I should be as high as possible. By knowing the beam half-angle α_b and spot size d_s the current I can be calculated using

$$I = \beta_s \left(\frac{\pi d_s^2}{4} \right) \pi \alpha_b^2 \tag{4.5}$$

where β_s is the source brightness. Using these equations it is possible to estimate the substrate exposure time. For a typical sample used in this work the exposure time for the total array is of the order of 6-12 hours depending on dot size and spacing. It is therefore important to maximise I through both α_b and β_s to obtain reasonable exposure times. Furthermore the obtainable resolution will be controlled by d_s. These are all controlled via the electron source and optics used [109]. An in depth covering of electron guns and optics is presented in section 5.1.

An important consequence of exposure unique to e-beam lithography is the proximity effect. The proximity effect is the exposure of the resist by electrons backscattered from the substrate. This leads to exposure of the resist in a larger area than that of the spot size and without compensating can lead to larger features than expected. Furthermore this 'background' is not constant but varies depending on the designed pattern e.g. the centre of the patterned substrate will receive a larger dose than that of the edges. The proximity effect can be compensated for by varying the beam current depending on which area is being exposed [107, 109]. The only time the proximity effect does not occur is in the case of electron transparent substrates e.g. SiN membranes. Exposure times with such substrates can be significantly longer. Furthermore the fragility of the membrane requires that special care be taken during the application of the resist [24].

Chapter 5

Experimental Techniques

The development of new magnetic materials for applications in devices requires an understanding of their physical properties. This is particularly the case for both read heads and MRAM as the lateral sizes of their sensor/storage stacks have decreased below 50nm. This is because as the structure size has decreased the dispersion in device to device characteristics has increased. This is due to the now dominant effects of the grain size distribution, crystal orientation/quality and layer-layer interface. Therefore in order to continue to improve the state of the art a number of techniques are required to measure the structural and magnetic properties of these materials and how they interact with eachother.

5.1 Structural Characterisation

The magnetic properties of a system are defined by the crystal sizes, structures and orientations of the materials used [34]. The measurement of these properties is not straightforward and there is no single piece of equipment that can measure all three accurately over a macroscopic area. The two main pieces of equipment used for these measurements are the Transmission Electron Microscope (TEM) [110] and X-ray Diffractometer (XRD) [111]. The TEM and XRD take advantage of the diffraction of sub-1nm wavelength radiation through a crystal lattice with the key difference between them being the probe size of the incident radiation. In a TEM the spot size is sub-20nm which allows for direct probing of the

crystal size, structure and orientation. However when carrying out magnetic measurements the contribution of the whole sample is measured and will not reflect that of the region observed using TEM. In XRD the probe size is on the order of 2-8 mm which means the measured properties are the average across the system. However distinguishing the contributions from each layer and obtaining a sufficient amount of data for quantitative analysis is time consuming and for disordered polycrystalline films is nearly impossible.

5.1.1 Transmission Electron Microscopy

The operation of a TEM is analagous to that of a projection light microscope operated in transmission mode. The key difference between electron and light microscopy is the source of contrast [110, 112]. In electron microscopy there are two major sources of contrast: mass-thickness and diffraction. The mass-thickness contrast is governed by Z-ratio dependent scattering which is analagous to and often called Rutherford scattering. This is where low angle ($< 0.5°$) scattering occurs due to interaction with the atomic nuclei. The number of electrons scattered is dependent on the proton number Z and the thickness of the film. In the case of work on magnetic thin films most of the elements used are the 3d metals while the film thicknesses tend to be sub-10nm and uniform and so the mass-thickness contrast is negligible. However in this work $IrMn_3$ is used. Whilst Ir has a proton number of 77 its concentration is low at 20-25% whilst the film thickness is still sub-10nm allowing for dismissal of the mass-thickness contrast [112].

Diffraction contrast requires a crystalline material where electrons can be diffracted and caused to interfere constructively and destructively in certain directions [110, 112]. This leads to a specific angle of diffraction known as the Bragg angle θ_B

$$n\lambda_e = 2dsin\theta_B \tag{5.1}$$

Where λ_e is the wavelength of the incident electrons and d is the lattice spacing. These sources of contrast originate from how the electron interacts with the material being imaged. When an electron passes into a material there are three possibilities: the electron will transmit without interaction, the electron will scatter elastically or the electron will

scatter inelastically. It is the elastically scattered electrons that provide both the mass-thickness and diffraction contrasts. In the case of TEM it is the transmitted and elastically scattered electrons that are used to form the image [110].

To form the image a complex system of lenses and aperatures are used. In a TEM the lenses are electromagnetic and consist of a copper coil wound around the optical axis. In order to ensure the magnetic lens acts as a 'thin lens' iron yokes and pole pieces are used to focus the field. This field acts as a converging lens where an electron travelling down the optical axis of the microscope will feel no force. However an electron at an angle θ off axis with velocity v entering the field B will feel a force F

$$F = evBsin\theta \tag{5.2}$$

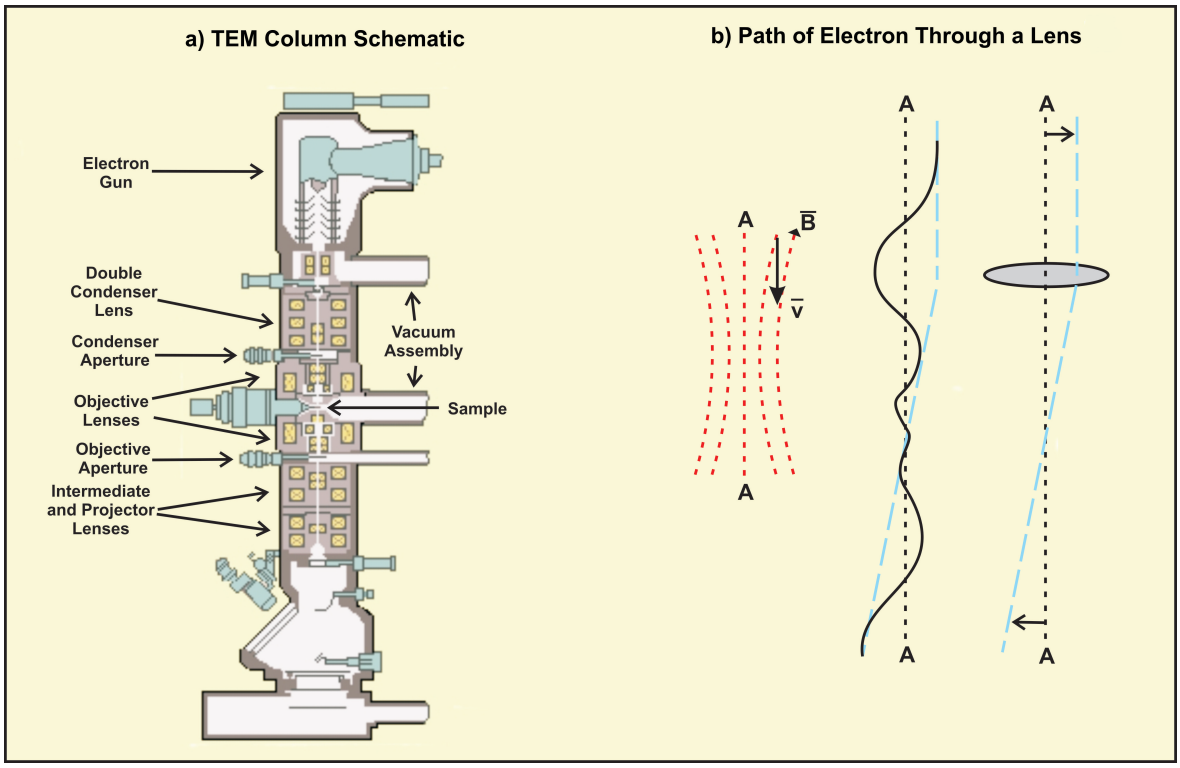

Figure 5.1: Schematic of a) a TEM column with optics and b) the path of an electron through an electromagnetic lens [113].

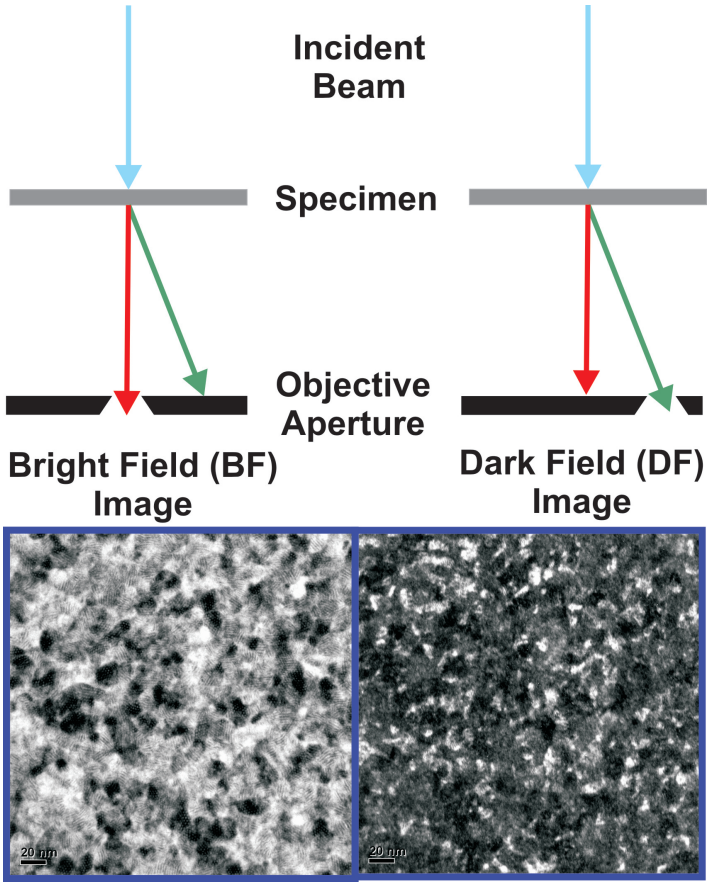

Figure 5.2: Schematic of the objective aperature setup for BF and DF imaging with example pictures from the same area in the respective modes. [112].

This force is perpendicular to both v and B causing a helical motion of the electron about the optical axis. Once the electron has a circumfrential component of velocity it feels a force as in equation 5.2 pulling it towards the optical axis. As seen in equation 5.2 the strength of the lens can be varied by changing B which is done by changing the current through the electromagnet. This allows for easy variation of the magnification and focus of the images and diffraction patterns [110, 112]. Schematics of a TEM column and the path of an electron through a lens are shown in figure 5.1.

Apertures are used to form different images by selecting electron beams and thus manipulating the image contrast. A key example of this is in Bright Field and Dark Field (DF) imaging. Through use of the objective aperture the electrons that are imaged can be chosen to be either those that are transmitted or diffracted only. As can be seen in figure 5.2 this

leads to a difference in contrast and information. Depending on the chosen electrons only certain crystal orientations will be observed [112].

Another important component of electron microscopes is the electron gun. The typical construction consists of three parts: the filament, Wehnelt cap, and the anode. Electrons produced by the filament are accelerated through the application of a voltage between the filament and the anode. The thermionic emission filament is one of the most common where a LaB_6 'needle' is heated to the point of electron emission. Electrons produced via thermionic emission have a wide spread of energies ($\sim$0.5-3.0eV) and therefore wavelengths [110]. As monochromatic electrons are ideal modern sources use field emission guns. Field emission guns consist of a single crystal tungsten filament etched to a 100nm wide point. An electric field of $\sim 10^9 \mathrm{Vm}^{-1}$ is applied across the tip to overcome the work function. As the temperatures required are significantly lower the energy spread is much less ($\sim$0.2-0.3eV) [110, 112]. In the case of this work the JEOL 2011 TEM used for this work a LaB_6 thermionic emission gun was use.

These principles apply to all systems which utilise an electron optical system and there is little difference in fundamental design. This carries across to e-beam lithography and as such all the above considerations apply when considering the probe size and electron dose.

5.1.2 Scanning Electron Microscopy

It is the inelastically scattered electrons that are used for imaging in the Scanning Electron Microscope. These electrons are deflected loosing a significant portion of their energy leading to the generation of secondary electrons, X-rays and photons. It is therefore quite common to find up to four detectors in an SEM chamber including one for the deflected, or back-scattered, electrons [110].

In an SEM the electrons are generated as described previously and focused into a spot which is scanned in a raster across the surface of the sample. Generally two sets of deflection coils are used to scan the beam so that the pivot point is on the optical axis in order to reduce the effect of lens aberrations. The diameter of the scanned spot is the major factor in controlling the resolution of the microscope and is controlled using a double condensor lens system. The first condensor lens sets the spot size by demagnifying the cross-over of

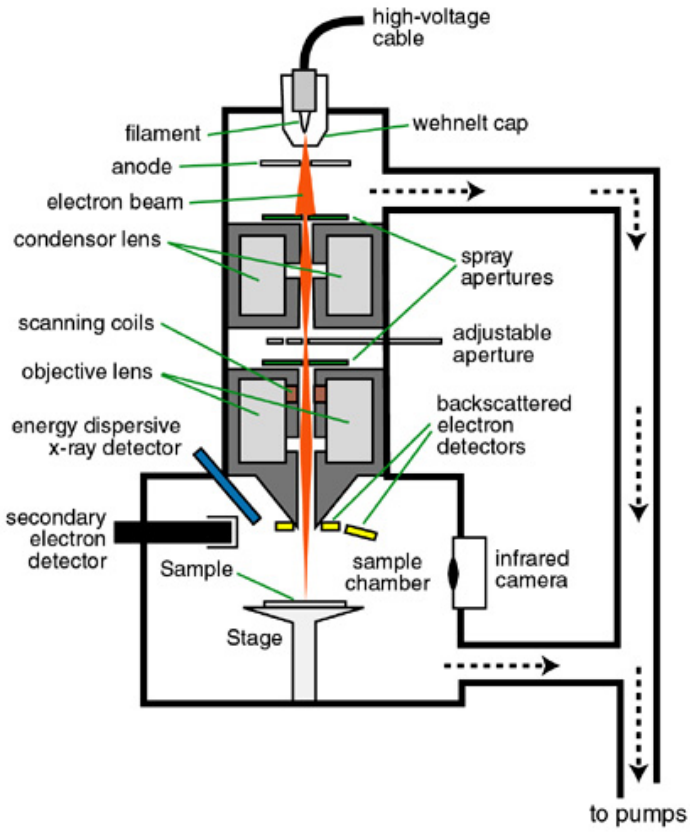

Figure 5.3: Schematic of the ray path in an SEM [114].

the gun producing a fine beam. The second condensor lens is controlled to ensure that the final cross-over occurs at the sample surface and is often referred to as the focus. Thus fine adjustments to the spot size can be made by changing the sample height and therefore the settings of the second condensor. In the case of the SEM used for this work the working distance was 5mm to obtain as small a spot as possible. A schematic of a SEM column and beam path is shown in figure 5.3 [110].

5.1.3 Measurement of the Grain Volume Distribution

In polycrystalline materials the magnetic properties of the system are highly dependent on the grain volume distribution [115]. The growth processes in granular systems are known

to follow a lognormal distribution which is defined as

$$f(D)dD = \frac{1}{(\sqrt{2\pi})\sigma D} e^{-\frac{((lnD)-\mu)^2}{2\sigma^2}} dD \tag{5.3}$$

where D is the particle diameter with μ and σ as the mean and standard deviation of ln$D$ respectively [116]. To calculate σ for a given number n of measured diameters the following equation is used

$$\sigma = \left[\frac{1}{n}\Sigma(lnD)^2 - \left(\frac{1}{n}\Sigma lnD\right)^2\right]^{1/2} \tag{5.4}$$

and the median diameter D_m is given by

$$D_m = e^{\mu} \tag{5.5}$$

To measure the grain diameter a number of Bright Field (BF) images are taken from the sample using a JEOL 2011 TEM. The diameter is measured only for those grains that satisfy the Bragg conditions i.e. giving a dark image. This is controlled through optimisation of the diffraction contrast to obtain a BF image which is done using the objective aperature as described in chapter 5.1. In this case the grains measured are those that appear black. An advantage of measuring in the BF over the DF is that the contribution from all grains is measured. Whereas when measuring in the DF a contrast is obtained only from grains of the specific targeted crystallographic orientation. A typical BF image is shown in the inset of figure 5.4 which is an example of a measured grain diameter and calculated lognormal distribution [110].

To measure the diameters of these grains an equivalent circle method is used. A circle of known diameter is matched against a grain so that the areas are equal. This diameter is then measured and the grain recorded to prevent repeat measurements. The measured diameters are then sorted into a histogram with typically 20 - 40 bins depending on σ, and plotted. Using the above three equations the lognormal distribution is calculated using the measured values of μ and D. The calculated lognormal distribution is then plotted against the measured diameters. A minimum of 500 grains are measured to ensure good statistics

[116]. An example of this measurement along with the calculated lognormal distribution are shown in figure 5.4.

5.1.4 X-ray Diffraction

The diffraction of X-rays is very similar to that of electrons however there are a few key and useful differences. The most obvious is the area over which diffraction is observed where in electron microscopy it is a small local region whereas in X-ray Diffractometer it is the full sample that is measured. In this way information not only on the crystallinity but orientation, mosaicity and lattice strain across the full sample can be obtained. Although lattice strain may be observed in a TEM it is often hard to observe due to strain induced by sample preparation. Furthermore as the diffracted X-rays are spread over a large three dimensional space individual spots can be scanned to a high resolution allowing for quantitative analysis

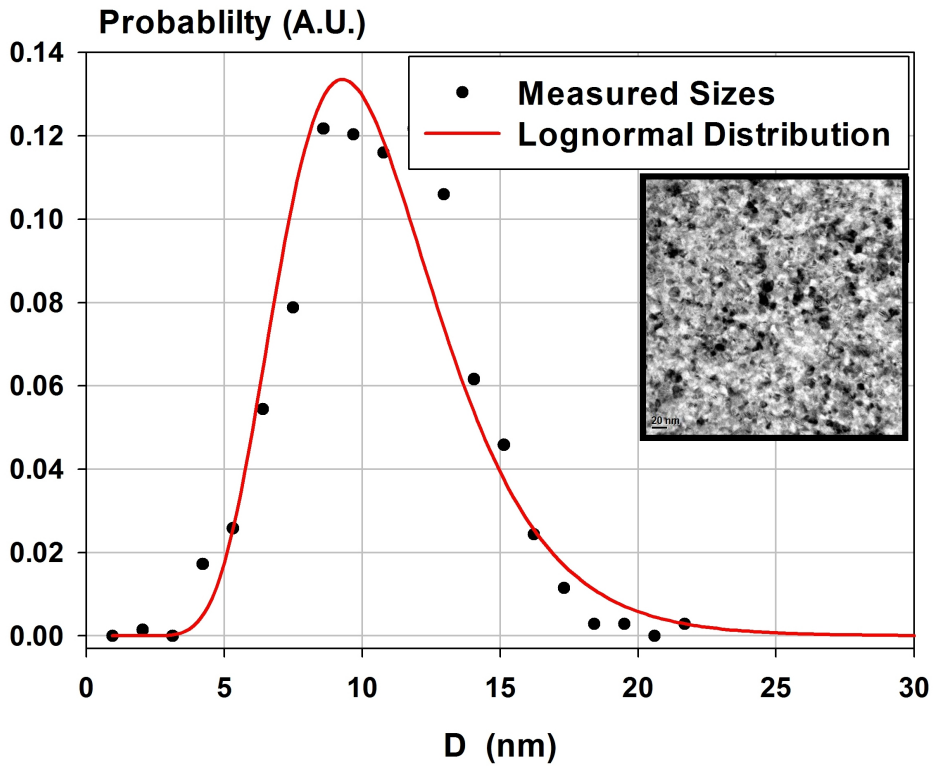

Figure 5.4: Example of the measured grain diameters with the plotted lognormal distribution and inset BF TEM image inset.

of these features.

To understand what is being measured by a XRD there must be an understanding of the reciprocal lattice and its translation to the angle between the sample and the incident and diffracted X-rays. Take a crystal with lattice planes of interplanar spacing d_{hkl}. These can be represented by a vector g_{hkl} which lies normal to the corresponding lattice with a magnitude of $1/d_{hkl}$. This vector is known as the reciprocal lattice vector the end of which is called the reciprocal lattice point. These reciprocal lattice points correspond to the lattice planes in a crystal and as such form a regular lattice reflecting this and is known as the reciprocal lattice.

The X-ray beam diffracted by the lattice planes corresponds to the reciprocal lattice vector using the equation:

$$k_g - k_o = g_{hkl} \tag{5.6}$$

where k_g and k_o correspond to the wave vectors of the scattered and incident X-ray beams respectively. Given that the X-ray beams are represented as a vector whose magnitude is is given by λ_X the equation can be rewritten as.

$$2d_{hkl}sin\theta = \lambda_X \tag{5.7}$$

which is the Bragg condition for diffraction. Therefore the sum of the two vectors k_g and k_o, the scattering vector k_s, corresponds to g_{hkl} when the diffraction condition is met. This is shown in figure 5.5a). Thus by controlling the direction and magnitude of k_s the reciprocal space may be mapped. How the X-ray vectors and k_s correspond to the reciprocal lattice is shown in figure 5.5 b).

To map the reciprocal lattice as well as its orientation/dispersion an XRD requires a goniometer with four rotation axes, three for rotating the sample and one for rotating the counter. This allows for the movement of k_s through three dimensions and is called a four-circle goniometer. These axes are: the rotational axis which corresponds to the incident angle of X-rays (ω), the rotational angle of the X-ray counter with respect to the incident X-ray beam (2θ), the rotational axis which is perpendicular to the scattering plane (χ) and

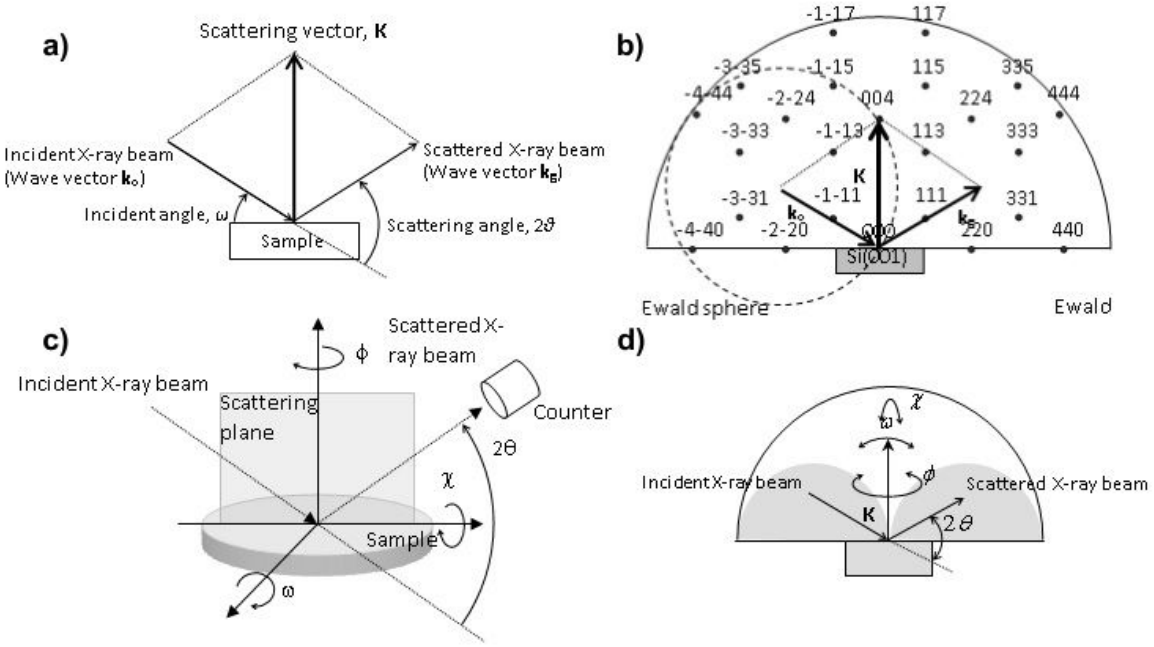

Figure 5.5: Schematic showing a) the definition of the scattering vector k_s and b) how it corresponds to the reciprocal space followed by c) the four circles of rotation and d) how they compare to the reciprocal space [117].

the in-plane rotation of the sample (ϕ). These are all shown schematically in figure 5.5 c). The angle χ can be replaced by allowing rotation of the X-ray counter in the plane of the sample ($2\theta_\chi$) and is used for full 3D mapping without significant change to the sample position. The relationship of these rotation axes on the movement of k_s in reciprocal space are shown in figure 5.5 d). The grey hemispheres represent the forbidden regions where the incident or diffracted beam would have to pass out the bottom or edge of the sample. To observe this region both χ and ϕ must be used to move the lattice points.

A further advantage of the 1.1Å wavelength of X-rays is that for most materials the refractive index is <1. As the refractive index is less than in atmosphere below some critical angle θ_c total internal reflection will occur. This is typically in the order of θ_c=0.2°-0.5° and is defined by the density of the material. When the angle of the incident X-rays exceeds θ_c refraction occurs leading to a decrease in the reflectivity in the order of the power of -4 [117].

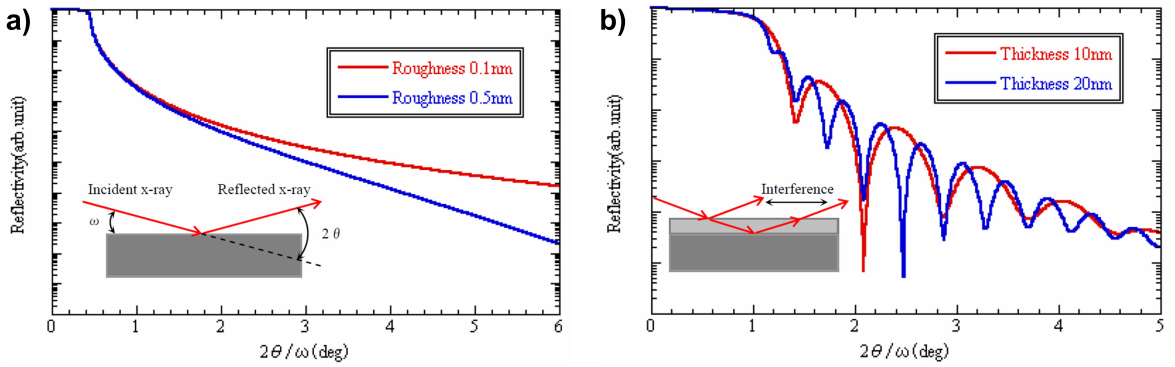

Figure 5.6: Example reflectivity profiles of a) Si substrate with a surface roughness of 0.1 and 0.5nm and b) Au film of thickness 10 and 20nm deposited a Si substrate [117].

In order to measure a reflectivity profile the reflected X-ray intensity is measured with respect to 2θ. An example reflectivity profile is shown in figure 5.6 a) where the surface roughness of a Si substrate is varied from 0.1-0.5nm. The roughness at the surface or the interfaces between deposited layers leads to scattering of the X-rays. This gives an increase in the attenuation of the profile with incident angle. When a layer is deposited on the substrate interference occurs between the X-rays reflected from the substrate-film and film-air interfaces leading to angle dependent constructive/destructive interference. An example of such a profile for Au layer of different thickness deposited on Si is shown in figure 5.6 b). As can be seen the film thickness affects the period of the profile where the thicker the film the shorter the period. In general the amplitude of the profile is defined by the difference in film densities and the degree of roughness. Therefore through measurement of the reflectivity profile the thickness, density and interface roughness of thin films can be measured [117].

5.1.5 Texture in Polycrystalline Thin Films

As shown in Chapter 3 the texture of the AF plays an important part in the thermal stability of the exchange bias. There are a number of steps that must be taken in order to fully confirm whether a layer is textured and at what orientation.

The first step towards measuring the texture and orientation of the layers is the $\theta/2\theta$

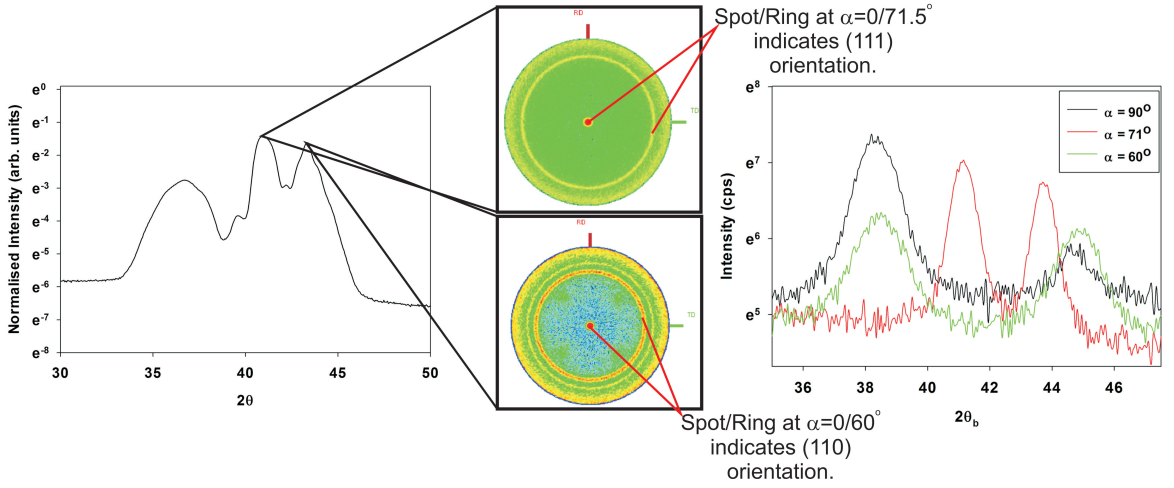

Figure 5.7: Example of a $\theta/2\theta$ scan along with two pole figures about the indicated peaks and the deconvoluted profile obtained through measurement of θb with χ and ϕ fixed.

scan. This moves the scattering vector k_s 'up' reciprocal space measuring only the lattice planes parallel to the sample surface giving an idea of crystallinity and orientation. To measure the type of structure e.g. fully disordered polycrystalline, fibre textured or single crystal, a pole figure scan must be carried out. This is done by fixing k_s with ω and 2θ and rotating χ and ϕ measuring the distribution of the targeted plane in three dimensions. A completely disordered polycrystalline material will give an even intensity distribution. A fibrous textured film has characteristic rings at specific angles of χ dictated by the targeted plane and the crystal structure. In the case of a perfect single crystal these rings turn to spots where not only χ but also ϕ are defined. These axes and how they translate to reciprocal space are all shown in figure 5.5. An example $\theta/2\theta$ scan and two pole figures about independent peaks both displaying evidence of fibrous textured polycrystalline films of differing orientation are shown in figure 5.7.

In order to confirm the orientation of a given layer a θb scan must be carried out. This is when the x-ray emitter, detector and the sample are all driven to a specific χ and ϕ. The emitter and detector are then moved so that the length of k_s varies whilst maintaining its orientation via χ and ϕ. By doing this only layers with the targeted orientation will give a peak. This can lead to a deconvolution of a complex $\theta/2\theta$ profile an example of which is shown in figure 5.7.

5.2 Magnetic Characterisation

There are two main types of magnetic characterisation, closed and open coil systems. Closed coil systems such as a B-H loop tracer and AC susceptometer are useful for susceptibility and low-field hysteresis loop measurements. In the measurement of exchange bias large fields in the order of kOe are required in order to saturate the F as well as to detect the offset loop. This requires the use of open coil detection systems where large electromagnets can be used. The two main open coil systems used are the Alternating Gradient Field Magnetometer (AGFM) and Vibrating Sample Magnetometer (VSM).

5.2.1 Alternating Gradient Force Magnetometer

The AGFM takes advantage of the force F_M felt by a magnetic sample in a non-uniform magnetic field. When the moment m of a sample is uniform the force felt by the sample in a position varying field is given by

$$\bar{F}_M = \bar{m} \cdot \bigtriangledown \bar{H} \tag{5.8}$$

The field gradient $\bigtriangledown H$ is superimposed on the uniform field applied by the electromagnet using a pair of current carrying coils. In order to measure the force felt by the sample in this gradient it is attached to a probe. The sample probe consists of a glass sample holder attached to two quartz legs the ends of which are glued to opposite sides of a piezoelectric bimorph. When a force is applied on the sample the piezoelectrc bimorph is stressed generating a voltage. If the applied field gradient is varied with a given frequency then the force and therefore measured voltage will changed accordingly. The use of an alternating gradient gives a number of advantages. Firstly the gradient can be tuned to the resonant frequency of the system, often between 100 and 1000Hz, giving a large increase in the amplitude of the measured voltage. Secondly the use of an alternating signal means a lock in amplifier can be used. The sensitivity of such a setup allows for a noise base of $\times 10^{-8}$emu whilst having a fast aquisition time e.g. a hysteresis loop from 1000 to -1000 Oe in 10 Oe steps takes typically 2 mins [118, 119].

Despite the clear advantages of the AGFM there are a number of important limitations. First of all any variation in the resonance of the system will cause drift in the measurement. This complicates greatly any measurement involving a change in temperature [119]. Secondly due to the sensitivity of the system acoustic noise such as that from vacuum pumps can cause significant drift and spikes in the measured signal.Thirdly the field gradient can lead to discrepencies in H_c. For example if a 5mm square sample is measured a gradient of 1Oe/mm will lead to a 5Oe difference in applied field across the sample. To overcome this field gradients of 0.1Oe/mm or less may be used. However this leads to a decrease in F_M and consequently the sensitivity of the system. For this work an optimum field gradient of 0.1Oe/mm was used. Finally the total mass of the system, sample plus glass holder, must be $<$100mg otherwise the signal amplitude is negligible. These limitations mean that the AGFM is used for quick, high resolution measurements of the hysteresis loop prior to in depth measurement using a VSM.

5.2.2 Vibrating Sample Magnetometer

The VSM measures the magnetisation of a sample by taking advantage of Faraday's law of induction. This is done by vibrating a sample between a pair of detection coils and measuring the induced voltage. This occurs due to a time varying flux passing through the detection coils. The total flux ϕ_F passing through the coils of area A_c at any one time is given by

$$\phi_F = B_m \cdot A_c = (H + M) \cdot A_c \tag{5.9}$$

where B_m is the flux density, H is the external applied field and M is the magnetisation of the sample. The emf ϵ induced by this flux is given by

$$\epsilon = -N\frac{d\phi_F}{dt} \tag{5.10}$$

where N is the number of turns in the detection coil and $d\phi_F/dt$ is the rate of change of ϕ_F over time. By substituting equation 5.9 into 5.10 and integrating over time the voltage

induced is

$$\int \epsilon \cdot dt = -NA_c \cdot M \tag{5.11}$$

As H is non-varying with respect to the detection coils it is only M that contributes to $\int \epsilon \cdot dt$.

An advantage of the VSM over other methods such as the B-H loop tracer is that it gives a measurement of the moment m of the sample. For this to be measured accurately regular calibration of both H and m must be carried out. Calibration of H is done through comparison to two reference points: 1) at a field as measured by a secondary standard Bell 9900 Gaussmeter 2) at zero by placing the probe in a zero field shield. The VSM's gauss probe is first placed in the zero field shield to establish the 0 point. The power supply is then set in increments up to 10kOe and the field calibrated against the reading from the Bell 9900 gaussmeter. For calibration of m palladium foil is used as it is a Pauli paramagnet and therefore has a well defined moment at any applied field. This allows for traceability of the moment back to the error in the applied field. A further advantage of palladium is that it does not corrode and so will not change over time. Another commonly used metal for calibration is nickel however it is not a suitable for calibration as it provides only a single point of calibration when at saturation M_s. Furthermore nickel is prone to corrosion and the process for removing oxides e.g. an acid etch will change the amount of material and therfore the value of m. To calibrate m a 5mm square palladium foil of known mass is placed onto a sample rod that has been cleaned in 1% hydrochloric acid for 30mins. The sample rod is then placed into the VSM and centered between the coils. The field is then set at 10kOe and the moment of the palladium entered. This process is repeated for a second palladium calibration sample cut into a circle of 5mm diameter. This is to ensure calibration for commonly used sample geometries.

An example of a basic VSM is shown in figure 5.8. The VSM sensitivity was of vital importance for this work. This was due to the requirement to measure large arrays of nanostructures where there was a loss of up to 75% of the volume of the thin film. This reduces a typical signal of 100μemu by up to an order of magnitude. Furthermore there are a number of issues associated with measurements at temperatures $<$50K. As can be seen in the schematic there are three main techniques employed to improve the Signal to Noise

Ratio (SNR).

The major limitation to the SNR is vibrational noise. As the detection coils are highly sensitive to variation in flux any vibration of the coils will lead to a change in signal. This vibrational noise is reduced in a number of ways. Firstly by utilising coil pairs connected anti-parallel any flux change equally present in both coils will be eliminated. Through use of a Digital Signal Processing (DSP) lock-in amplifier most remaining signals due to vibration will be eliminated. However any mechanical coupling between the detection coils and the sample head can lead to signals that cannot be easily removed. Typically the detection coils are attached to the faces of the pole pieces with the electromagnets placed on vibration dampers in an attempt to decouple the sample head from the coils [120]. Issues can arise when utilising a cryostat for low temperature measurements. This is because the cryostat is suspended from the sample head and any contact with the detection coils can be detrimental. This is controlled through careful alignment of the cryostat and coils.

In order to remove any other erroneous sources of noise e.g. external vacuum pumps, the sample head contains a second set of detection coils between which a reference sample

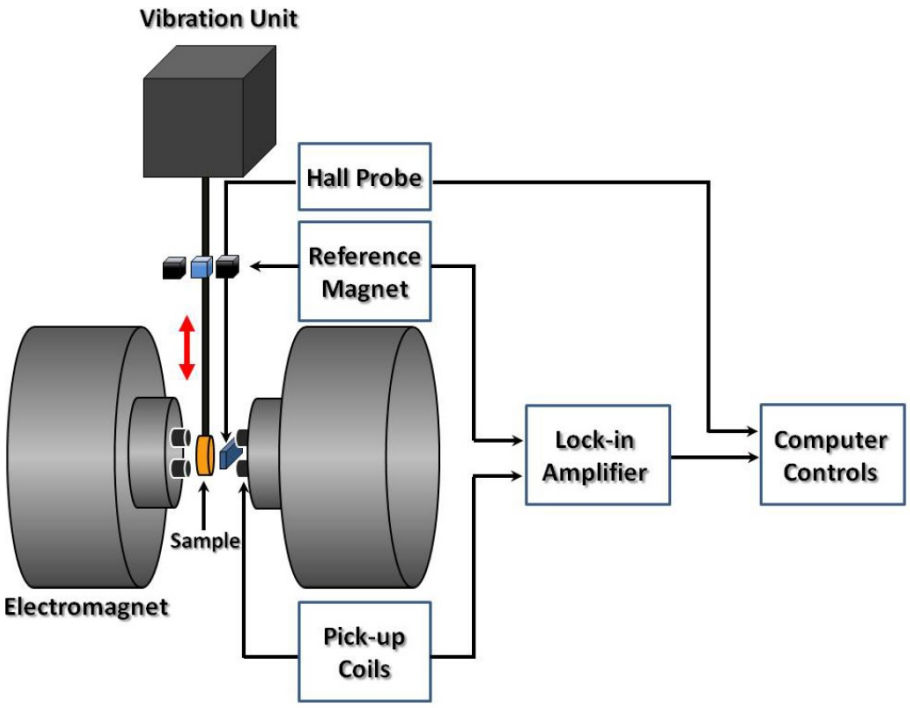

Figure 5.8: Schematic diagram of a VSM.

is driven. As this reference is vibrated by the same driver the phase and amplitude of the voltage from both the reference and detection coils are directly related. Through comparison of these voltages the measurement can be made independent of variations in vibration frequency and magnetic field uniformity. A further source of noise was found to be due to the buildup of a static charge on the sample rod. This gives rise to a phantom time varying moment where random discharges lead to large jumps in signal. This was eliminated by setting up an anti-static fan so as to blow onto the sample rod. Taking these issues into account a modern VSM can obtain a sensitivity of 1μemu [120–122].

5.2.3 The York Protocols

When measuring an exchange biased material the result is due to a number of different contributions: the strength of the F-AF coupling, the thermal stability of the AF and the magnetic order of the AF. Seperating these different contributions is a difficult task which requires careful experimental protocols.

The most simple of these issues to address is the order of the AF. As mentioned previously this is traditionally done by field cooling from above the T_N of the AF. However in the case of systems with technological applications e.g. a TMR read head with the AF $IrMn_3$, this is not possible. This is due to $IrMn_3$ having T_N=690K at which diffusion between the layers in the stack will occur. However for polycrystalline $IrMn_3$, field cooling from temperatures as low as 300K can result in ordering of the film. This setting process occurs due to thermal activation across the energy barrier

$$\Delta E = K_{AF} V_{AF} [1 - H^*/H_K^*]^2 \tag{5.12}$$

of the AF grains as shown previously in chapter 3 [4].

The ease of setting the AF leads to both the solution and cause of thermal instability in the AF. In order to measure H_{ex} and H_c reproducibly there must be no change in the order of the AF in the time it takes to perform a measurement [4, 77]. To overcome such issues the magnetic and thermal history of the AF must be controlled. To ensure a controlled and systematic variation of the order in the AF a set of protocols were developed within the group and are as follows [4]:

The first step is to set the order of the AF in a reproducible manner. The sample is heated to a maximum temperature T_{set} at which interfacial diffusion does not occur. This is done whilst applying a field H_{set} sufficient to cause saturation of the F layer. This state is held for a time t_{set} which is system dependent. For this work a t_{set} of 3600s was chosen due to the linear behaviour of H_{ex} in lnt_{set}. After 3600s the change in H_{ex} with t_{set} is <1% which gives reproducibility in the value of H_{ex} [4].

The second step is to ensure that no thermal activation occurs in the AF during the time of the measurement. With the sample in the setting state as described above it is then cooled with a field H_{set} applied to a temperature at which there is no thermal activation of the AF grains (T_{na}). The point of T_{na} is determined by first cooling to a trial T_{na} and taking a measurement. A field -H_{set} is then applied at this temperature for a length of time e.g.1800s and then a loop measured. If any change in the loop is observed a new, lower T_{na} must be used. These protocols are shown schematically in figure 5.9 [4]. Once the sample has been set and field cooled to T_{na} controlled and reproducible measurements of H_{ex} may

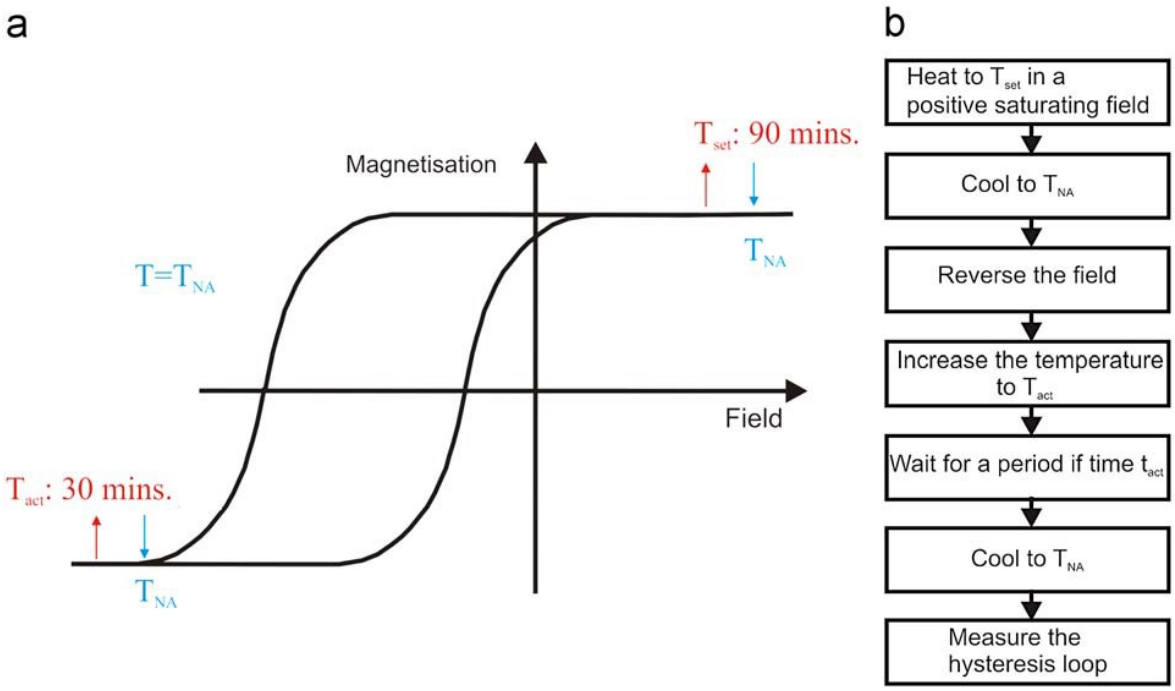

Figure 5.9: Schematic of the York protocols [4].

be carried out. Through careful variation of H_{set}, T_{set} and T_{na} the different interactions in an exchange biased material can be probed independently.

5.2.4 Measurement of the Blocking Temperature Distribution

The blocking temperature (T_b) of an exchange biased material is traditionally defined as the temperature at which H_{ex} goes to zero. In a polycrystalline material each grain has its own value of T_b and as such the AF is characterised by a distribution of T_b, $f(T_b)$. Thus it is possible to thermally activate the AF in a controllable fashion. This is carried out by first setting the AF at a temperature T_{set} and then cooling to T_{na} in a field H_{set}. In this state a field of -H_{set} is applied and the sample heated to an activation temperature $T_{act} < T_{set}$ for a time $t_{act} < t_{set}$. The sample is then field cooled to T_{na} and a loop measured. This process is repeated in increasing steps of T_{act} until T_{act}=T_{set} [4].

This process of controlled activation and reversal leads to a gradual change in H_{ex}. This is caused by heating with the F reversed which leads to a change in order of the AF from the initial state to the reverse orientation as shown in figure 5.10. The amount of reversal

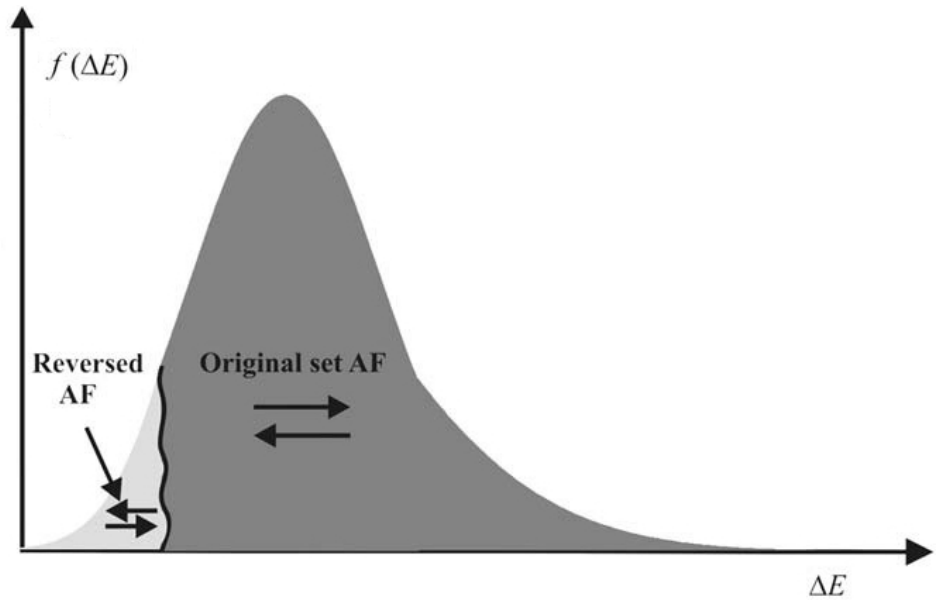

Figure 5.10: Schematic diagram of the controlled reversal of the distribution of AF energy barriers [4].

that occurs is a function of T_{act} and exchange field from the F layer. The value of H_{ex} at a given T_{act} will then be proportional to the fractions of the AF grains oriented in opposite directions [4].

$$H_{ex} \propto \int_{T_{act}}^{\infty} f(T_b) - \int_{0}^{T_{act}} f(T_b)\,\mathrm{d}T_b \tag{5.13}$$

This proportionality is valid assuming the strength of the interfacial coupling given by the prefactor C^* is independent of the orientation of an AF grain which has been shown to be the case [4].

From this it can be seen that when H_{ex}=0 there are equal fractions of the AF volume distribution which are oriented in opposite directions. Therefore this measurement is at the point of the median blocking temperature $\langle T_b \rangle$. This point only corresponds to the median AF grain volume V_m when the distribution is fully set and stable over the course of the measurement. It is important to note that as this is a volume effect it has a squared dependence on the radius of the grain. For example a change in grain diameter from 10nm to 9nm leads to a 20% change in the grain volume. Therefore for a full measurement of the distribution of T_b the grain size distribution should be known.

5.2.5 Measurements of Interface Properties

The measurement of the distribution of T_b gives the bulk dependence of the AF as described by the volume integral in the equation

$$H_{ex}(H_{set}, T_{set}) = H_{ex}^{i} C^*(H_{set}, T_{set}) \int_{V_c(T_{meas})}^{V_{set}(T_{set})} f(V) dV \tag{5.14}$$

Therefore for a full theoretical understanding the strength and behaviour of the interfacial coupling C^* must be known. As mentioned in chapter 3 C^* is a dimensionless variable of a value between 0 and 1. This is taken to be an average of the interfacial coupling across the sample whereby for a perfect sample where C^*=1 there would be an intrinsic value of H_{ex} as given by H_{ex}^{i}. However the isolation and measurement of the properties of the interfacial coupling between the F/AF is a complex and difficult task. Before any attempt to

measure these is made the above protocols must be used to ensure that any change is not due to thermally active AF grains or the activation of unset grains. As mentioned in section 3 there are three major measurements that give information about the interface: the H_{set} dependence of H_{ex}, the low temperature dependence of H_{ex} and the training effect. The measurement of these are complex and a lack of attention can render them indecipherable.

The most simple of these measurements is the H_{set} dependence of H_{ex}. To measure this effect a setting time t_{set} and temperature T_{set} must be selected to ensure reproducible setting of the bulk of the AF grain volume distribution. The sample is then set, field cooled and measured after increasing values of H_{set}. It is important to note that the training should either be removed or measured due to it having a potential H_{set} dependence. Care must be taken during sample fabrication and any following steps to ensure the AF is fully disordered before the measurement is started. This can be an issue if a magnetic field is applied to the sample during growth or if there is any significant substrate annealing after deposition of the F layer. This is because the remanence of the F can be sufficient to set the AF even if no external field is applied. An 'unsetting' of the AF is not a simple task and requires AC field cooling.

The training effect is measured by setting and field cooling the sample defined by the York Protocols and once at T_{na} measuring two loops. The training effect is thus defined as the change in H_{c1} which is the first point of reversal to negative saturation -M_s. Initial reports of this effect noticed changes in H_{c2} as well as a continual but decreasing change with further repeat loops [5]. This has since been attributed to thermal activation of unstable AF grains [4, 27]. As such if these effects are observed a careful measurement of T_{na} should be carried out and the measurement routine modified accordingly. It is very important to ensure that post field cooling the field is not taken to a point where the sample begins to reverse before measurement of the first loop. This is because the training effect is thought to be field dependent and therefore unpredictable changes may occur that give an inaccurate measurement of its magnitude. It is important to note at this point that the training was removed from all measurements where it was not being measured e.g. the measurement of the distribution of T_b. This is done by carrying out a field sweep from H_{set} to -H_{set} and back.

The measurement of the low temperature (sub-100K) dependence of H_{ex} is a complicated matter. This is partially because there is a change in both the H_{set} dependence

of H_{ex} and the training effect with decreasing temperature. Furthermore the information obtained will be highly dependent on the measurement protocols used. For example one method is to field cool the sample to 4.2K and measure a loop. Then the temperature is progressively raised whilst measuring loops at specific points. This type of measurement is similar to that of the blocking temperature distribution and could give information on the interfacial clusters analagous to that of the temperature decay of remanence. However if the clusters behave more like the AF grains it could be prudent to follow a routine similar to that of the measurement of $\langle T_b \rangle$ whilst using T_{meas}=4.2K. This complication is similar to that which lead to the development of the York Protocols. Part of this work was to characterise the interface in exchange biased materials and as such the results and validity thereof will be covered in chapter 6.

Chapter 6

Interfacial Effects in Exchange Bias

As discussed in chapter 3 the York Model has been used to successfully model the AF volume dependence of exchange bias in polycrystalline film [4]. An extension to a strong domain wall pinning model for single crystal thin films based on defects or inclusions has also been successful [96]. However the mechanisms behind the behaviour of the F/AF interface are complex and a number of attempts to model the system have had limited success. This is due in part to the wide variety of measurements reported for a diverse number of systems.

A conceptual model was developed following key experimental results described in detail in chapter 3 i.e. the setting field dependence of H_{ex}, spontaneous spin freezing and the trilayer experiment. The hypothesis is that the frustrated spins at the interface form into clusters which behave in a manner analagous to a fine particle system. The strength of the coupling between the F and AF layers is dictated by the ordering of these entities. By measuring the behaviour of H_{ex} due to changes that occur only at the interface some knowledge of the ordering of these clusters can be obtained. Any model of the interface must explain all these effects as well as providing insight into other effects such as training and the coercivity of exchange biased systems.

Through the use of the York protocols as described in chapter 5 a series of experiments can be designed which remove any contribution due to unset or active AF grains in the distribution allowing for the contribution due to the interface to be measured. However the F/AF system is complex and seperating out effects due to the crystallinity of the F and AF layers as well as the coupling between them is challenging.

6.1 Seed Layers and Texture

The magnitude of H_{ex} and H_c as well as their dependence on temperature are known to be controlled by the texture and crystallinity of the AF [17, 41, 123, 124]. The use of a seed layer to control the crystal quality, orientation and grain size dispersion in thin films is well established across multiple fields. In the case of exchange biased films the crystalline quality and texture will not only influence the magnetic properties of the AF but also the F layer. In order to measure the change in the structure of the AF due to the use of seed layers any change in the F layer must also be measured.

In the work of Aley et al. [17] 3 samples of structure X(5)/IrMn(10)/CoFe(3)/Ta(10) (nm) were deposited where X is a seed layer of Cu, Ru or NiCr. The texture of the $IrMn_3$ layer was measured using a XRD. It was found that the sample grown on the NiCr seed layer had a strong (111) texture in the plane of the film whilst those deposited on the Cu seed layer had a poor texture. The system deposited on Ru gave a texture intermediate between NiCr and Cu seed layers. The blocking temperature distributions of the samples were measured and it was found that the median blocking temperature $\langle T_b \rangle$ was equal to 367, 186 and 477K for the samples grown on the Cu, Ru and NiCr seed layers respectively. The grain diameter distributions were also measured and the median grain diameter D_m were found to be 10.7, 6.0 and 3.9nm for the samples grown on the Cu, Ru and NiCr seed layers respectively. Aley et al. then used the York Model to calculate the effective AF anisotropy K_{AF} as described in chapter 3 and reproduced below

$$K_{AF}(< T_b >) = \frac{ln(tf_0)}{V_m} K_B < T_b > \tag{6.1}$$

K_{AF} was found to be 0.28×10^7, 0.94×10^7 and 3.3×10^7 ergs/cc for the samples grown on the Cu, Ru and NiCr seed layers respectively. This work showed a clear variation in the effective K_{AF} and therefore thermal stability of the AF with the (111) texture in $IrMn_3$.

Building on the work of Aley et al. [17] the structures X(x)/IrMn(10)/CoFe(5)/Ta(5) (nm) were deposited on Si(100) substrate where X is a seed layer of NiCr or Cu of thickness 6 and 5nm respectively. For each structure four samples were deposited the first of which was just a seed layer and thereafter seed plus AF, seed, AF and F and finally the full stack. A $\theta/2\theta$ scan was carried out for each of these samples in an attempt to observe the quality

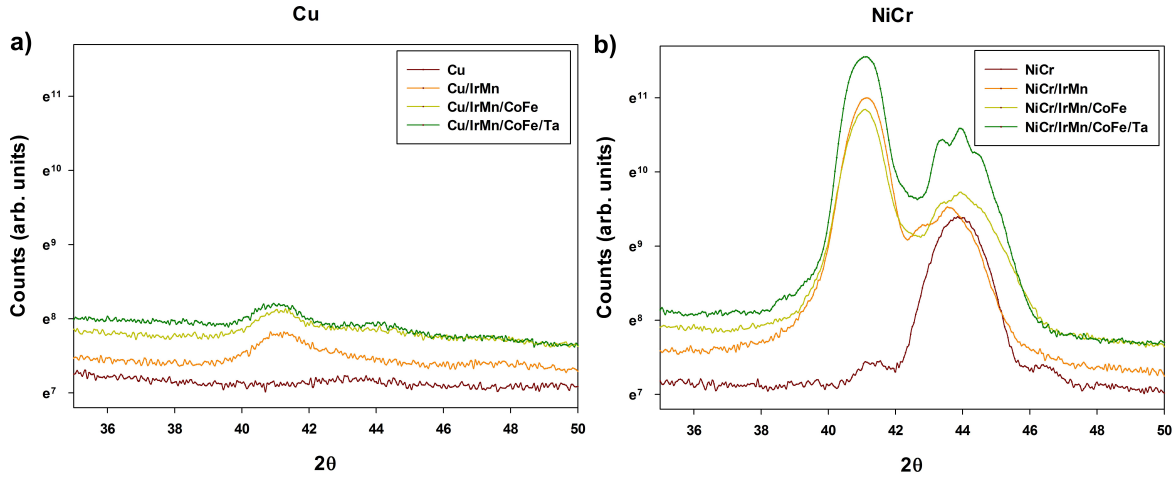

Figure 6.1: $\theta/2\theta$ scans of the samples deposited on a) a Cu seed layer and b) a NiCr seed layer.

of each material in turn and the effect of the seed layer on those that followed. From the work of Aley et al. it is expected that a Cu seed will give a weak texture and a NiCr seed a strong (111) texture in the $IrMn_3$ layer.

Figure 6.1 a) shows the $\theta/2\theta$ scans obtained for the samples based on a Cu seed layer. As can be seen no Cu peak is obtained within the range of measurement at the expected angles of 35.08° and 43.32° for the (110) and (111) planes respectively. The only peak obtained is that for $IrMn_3$ (111) at a 2θ angle of 41.43°. A pole figure measured around the $IrMn_3$ (111) peak confirms that the film has no observable texture within the resolution of the equipment as shown in figure 6.2 a). There is a variation in the X-ray intensity detected in the pole figure with increasing angle α_{pf} however this is due to a widening of the beam profile on the sample as the gun/detector geometery is varied.

The $\theta/2\theta$ scans for the samples based on a NiCr seed are shown in figure 6.1 b). A distinct set of peaks is obtained with NiCr (111) at 43.63°, $IrMn_3$ (111) at 41.43° and a potential CoFe (110) peak at 44.83°. In the scan of the sample that is just a NiCr layer two shoulders are observed either side of the main (111) peak. These are most likely due to X-ray reflection indicating a low roughness growth and a strong fibrous texture. A pole figure measured around the $IrMn_3$ (111) peak confirms the strong fibrous texture as shown in figure 6.2 b) by the ring at an α_{pf} of 19.5° and a strong centre spot.

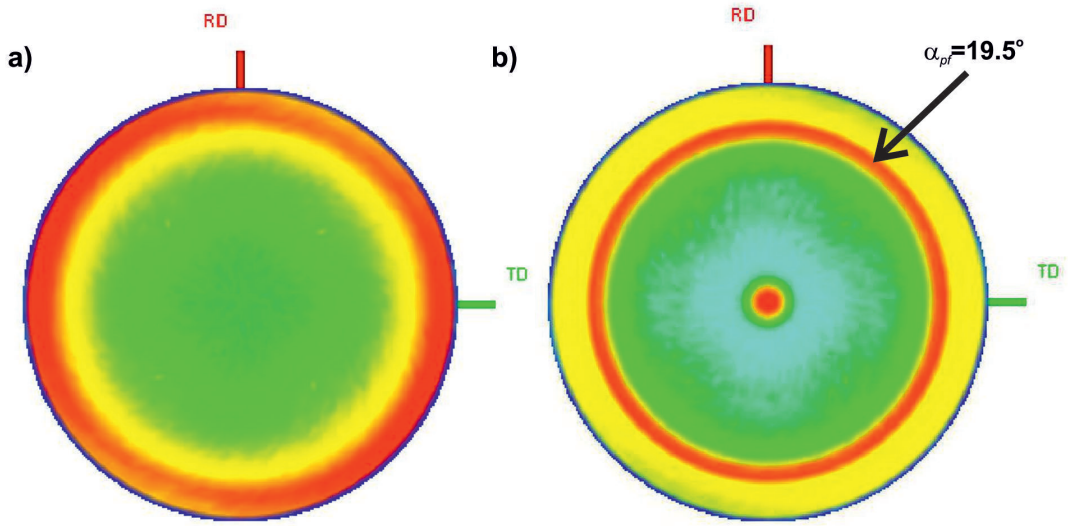

Figure 6.2: Pole figure scans about the $IrMn_3$ (111) peak at 41.43° for the samples deposited on a) a Cu seed layer and b) a NiCr seed layer.

The results for the texture induced in the $IrMn_3$ layer are what was expected following from the work of Aley et al. [17] with a Cu seed giving no texture and a NiCr seed giving a strong fibrous (111) texture in the $IrMn_3$. However in previous works it was found that when a 5nm NiCr film was deposited on an oxidised Si wafer no texture develops in the NiCr layer [17, 123]. In thin film growth a (111) texture is favoured by FCC crystals when deposited on an amorphous film due to the minimisation of the surface energy [125]. It was for this reason that Aley [17] and Peng [123] thought that NiCr provided a strong (111) texture in the $IrMn_3$. However if this were the case a strong (111) texture in the $IrMn_3$ grown on the Cu seed layer would be expected. Furthermore it is clear from the XRD data taken in this work that a strong (111) texture is obtained for the NiCr seed layer. As such the texturing of the $IrMn_3$ layer must be due to the strong (111) texture in the NiCr layer.

Both NiCr and Cu are FCC with atomic spacing along the (111) plane (a_{111}) of ∼2.52Å and ∼2.55Å respectively and so should match to a similar degree to a_{111} in $IrMn_3$ of 2.67Å. However typical deposition rates for NiCr and Cu are 0.9Å/s and 1.9Å/s respectively which would lead to a difference in layer roughness and grain size. X-ray reflectivity measurements were carried out on the NiCr and Cu seed layer samples in order to measure any change in

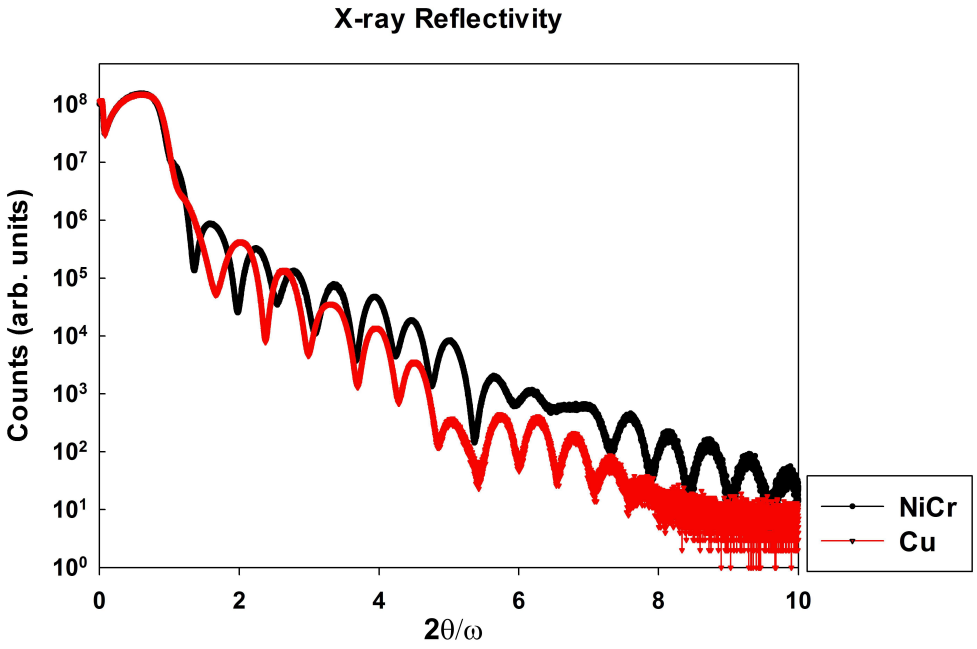

Figure 6.3: X-ray reflectivity measurements of the full stacks NiCr/IrMn/CoFe/Ta and Cu/IrMn/CoFe/Ta showing a difference in roughness for identical growth conditions.

layer roughness. As can be seen in figure 6.3 there is a clear difference in profile attenuation between the NiCr and Cu seed layers. This gives an interlayer roughness for the sample grown on the NiCr seed of ∼0.3nm and for the Cu seed of ∼1.0 nm. Despite the similar lattice missmatch with $IrMn_3$ of -4.5% and -5.6% for both Cu and NiCr respectively and therefore suitability of seeding growth along the (111) plane this difference in roughness and the associated quality of the depositon shows NiCr to be the superior seed layer.

Layer	Deposition Rate (Å/s±0.5%)	a_l (Å±1.25%)	a_{111} (Å±1.25%)	Lattice Missmatch with $IrMn_3$ (111)
Cu	1.9	3.61	2.55	-4.5%
NiCr	0.9	3.56	2.52	-5.6%
$IrMn_3$	1.4	3.77	2.67	0%
CoFe	0.5	2.85	2.02	-24%

Table 6.1: Summary of key values for crystal and texture analysis.

As shown in the summary of these results in table 6.1 NiCr and Cu can be used to vary the texture of the (111) plane in $IrMn_3$. However a large difference in sputter rates could lead to a variation in grain growth which would affect the texture obtained in the seed layer. Furthermore the interlayer roughness is also changed which could be some reflection of the grain size of the film and will have an impact on the magnetic properties obtained due to the interfacial nature of exchange bias.

6.2 Seed Layers and AF Grain Size

The seed layer not only affects the texture but also establishes the grain diameter distribution of the subsequent layers. The reflectivity data in figure 6.3 implies that the median grain diameter D_m will be smaller for the samples grown on the NiCr seed layer and larger for those on the Cu seed layer. This would fit with the results obtained in the work of Aley et al. [17].

To measure this effect two pairs of samples were deposited. These samples were of structure X(x)/CoFe(3)/Ta(5) and X(x)/IrMn(10)/CoFe(3)/Ta(5) (nm) where X is a seed layer of NiCr or Cu of thicknesses x=7.5 and 5nm respectively. The first pair of samples were deposited as a control in order to confirm whether the change in magnetic properties is due to a variation in the CoFe layer irrespective of the exchange bias. The second pair were designed to compare the effect of exchange bias films deposited on NiCr and Cu seed layers both magnetically and structurally .

The measured grain diameter distributions for these samples are shown in figure 6.4. For the CoFe and IrMn/CoFe samples grown on a Cu seed layer the median grain diameters D_m were 7.3 and 7.7nm respectively. This is an $\sim$5% increase in D_m which is also matched by a change in the standard deviation σ from 0.33 to 0.35. This change in both D_m and σ is consistent with an increase in sample thickness due to the addition of 10nm of $IrMn_3$ [125–129]. A similar change is observed between the CoFe and IrMn/CoFe samples grown on a NiCr seed layer with $D_m = 8.8$ and 10.2nm respectively.

One key to the York Model and this work is that grain growth is columnar which at first appears to contradict these results. However for the Cu/CoFe and NiCr/CoFe films the total layer thicknesses are 13 and 15.5nm respectively. When compared to the median

diameter D_m of each sample it is clear the grain structure will have only just coalesced. On addition of a 10nm layer of $IrMn_3$ the thickness of the films will have effectively doubled moving the evolution of the grain structure from the coalescing to thickening regime and as such a small change in D_m is fully expected [126]. In the case of the full exchange biased stack it is a reasonable assumption to expect the IrMn/CoFe layers to be columnar.

Both Cu and NiCr should be suitable seed layers for the growth of (111) in-plane textured $IrMn_3$, however this is not the case. It was thought the lack of a texture in the sample grown on a Cu seed layer in comparison to that grown on NiCr must be due to a difference in the mechanism of grain growth. From the measured grain diameters of 7.7 and 10.2nm for the samples grown on the Cu and NiCr seed layers respectively there is clearly some difference in grain growth during deposition. In sputtering of polycrystalline films growth typically follows a process of nucleation, growth, impingment and coalescence [126]. This process is complex where the final grain size is dictated by substrate temperature at deposition, diffusivity of the material, deposition rate and thickness. Furthermore texture selection of

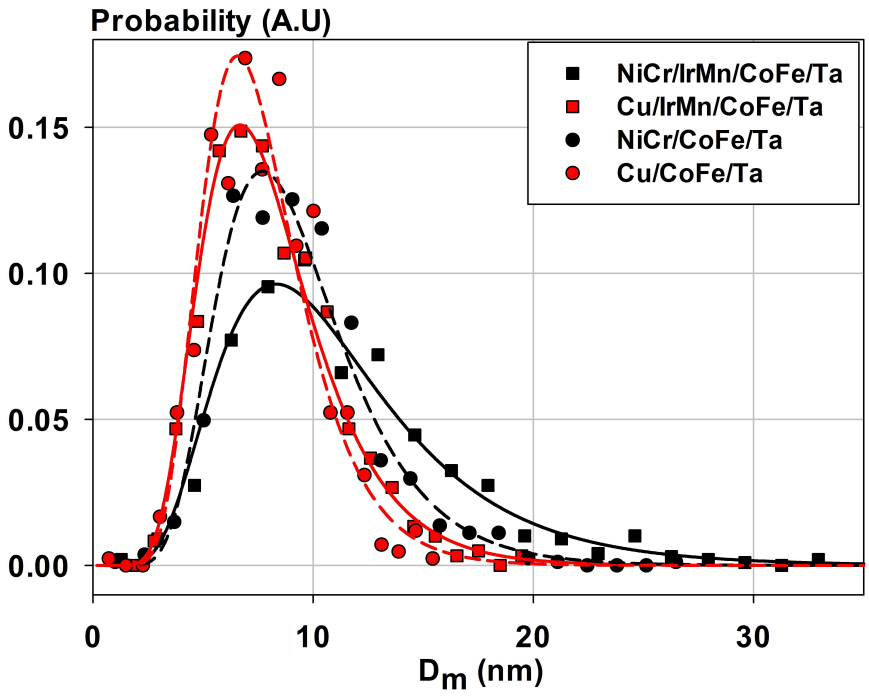

Figure 6.4: Grain diameter distributions for the CoFe systems grown on seed layers of Cu and NiCr both with and without $IrMn_3$ where the lines are the calculated lognormal distributions.

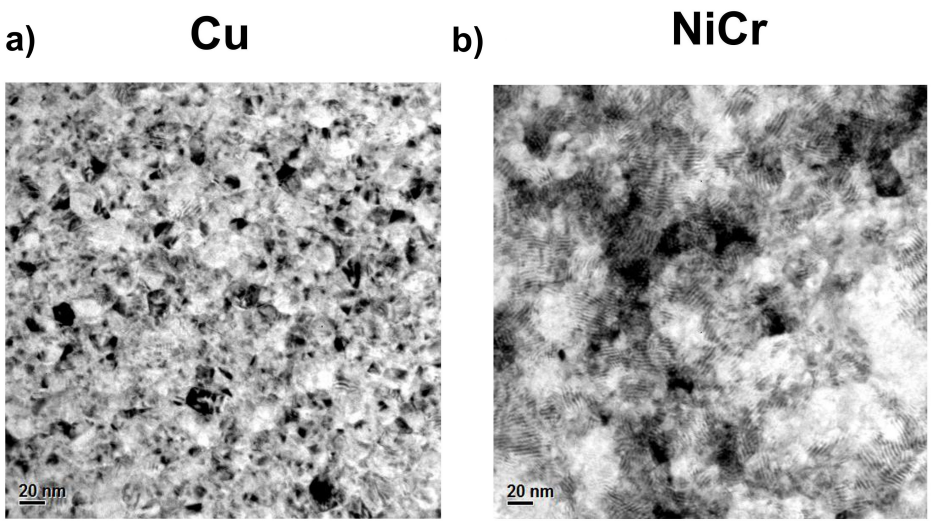

Figure 6.5: Typical TEM images obtained for the samples grown on the a) Cu and b) NiCr seed layers.

the films occurs due to a combination of preferred growth and minimisation of the surface energy [128, 129].

It is not the aim of this work to define the key differences in the mechanisms of grain growth for the Cu and NiCr layers, however a few details are known which lead to a hypothesis. In the case of the Cu seed layers the deposition is fast at 1.9Å/s with a known diffusivity of 5.9×10^{-13}m^2/s. For the NiCr seed layers the deposition rate is 0.9Å/s with a diffusivity 1.6×10^{-13}m^2/s [130]. Furthermore the temperature of the substrate during growth was 320K which was ∼20% of the melting temperatures of both NiCr (T_{mp}=1665K) and Cu (T_{mp}=1360K). Given that the grain sizes were ∼50% of the total film thickness the growth type is likely that of non-equiaxed columnar grains [128]. Although work has been published from the same deposition tool showing large grained, equiaxed columnar films

Structure	D_m (±0.5 nm)	σ (±0.02)	V_m (nm^3)
Cu/CoFe	7.3	0.33	420±50
Cu/IrMn/CoFe	7.7	0.35	470±50
NiCr/CoFe	8.8	0.36	610±70
NiCr/IrMn/CoFe	10.2	0.45	820±90

Table 6.2: Summary of key results from the measured grain size distribution.

these had undergone an ex-situ annealing step leading to secondary grain growth [126, 131]. In non-equiaxed columnar films coalescence of the grains is a competition between stress and crystal energy, the mechanism of which is dictated by the mobility of the grain boundaries. In the case of the Cu seed layer where the diffusivity and the deposition rate are large, the dominant mechanism will be that of minimisation of stress through grain boundary movement leading to randomly oriented small grains [125, 126]. In the case of the NiCr seed layer the deposition rate and diffusivity are 50% and 25% of that in the Cu based system and so the dominant growth mechanism is that of minimisation of crystal energy through texture selection whereby growth is favoured along the (111) plane leading to a large grain textured film [128, 129].

A table of key results is shown in table 6.2 along with typical TEM images shown in figure 6.5. It is worth noting at this point that even though the difference in D_m between the samples grown on a Cu seed vs. a NiCr seed is $\sim$22.5% exchange bias is a volume effect [4]. As such it is the median volume V_m that is important and in this case were found to be 470nm^3 and 820nm^3 for the samples grown on the Cu and NiCr seed layers respectively. The objective sought by changing the seed layer was to change the texture and therefore the effective K_{AF} of the $IrMn_3$ layer as in the work of Aley et al. [17]. However it clear that this change in texture is probably due to a change in the grain growth process during deposition. This leads to a change not just in the texture of the $IrMn_3$ layer but also the interfacial roughness and grain diameter all of which will affect the magnetic properties of the films.

6.3 Seed Layers and Anisotropy of $IrMn_3$

To understand the contribution of the AF anisotropy to the F magnetisation reversal the effect of structural variations and any magnetic/thermal processes must be seperated out. It has been established that deposition of CoFe on Cu and NiCr seed layers gives a difference in grain diameter of $\sim$20% whilst the effect on the crystallinity was difficult to observe via XRD due to the low thickness of the layer. While the difference between the NiCr and Cu a_{111} of 2.52Å and 2.55Å respectively with that of the CoFe of 2.02Å is large enough so as not to give rise to preferential growth, the (110) plane has a spacing of 2.85Å which

has less of a missmatch at 11.6% with the NiCr (111) plane. Therefore it is reasonable to assume that given the previous texture and grain size data CoFe, will grow with a weak (110) in-plane texture in the sample grown on the NiCr seed layer and not for that grown on the Cu seed layer.

With the change in crystallographic and granular structure of the CoFe layer somewhat understood, progress may be made into measuring the changes due solely to exchange bias. However this first requires the breaking down of the setting process of the AF into its various components. The following procedure was used:

1. The CoFe samples grown directly on the seed layer were measured first in order to provide a control sample.
2. IrMn/CoFe samples were then measured as deposited (i.e. without setting) in order to obtain the effect of disordered $IrMn_3$.
3. IrMn/CoFe samples were then annealed in zero field at a temperature T_{set}=498K for a time t_{set}=1800s and then cooled to T_{ms}=173K and a loop measured.
4. The IrMn/CoFe samples are then annealed in a field H_{set}=5kOe at T_{set}=498K for t_{set}=1800s and then cooled to T_{ms}=173K and two loops measured in order to observe the training effect.

Measuring at T_{ms}=173K ensured that both samples were at T_{na} which was confirmed by holding the sample at reverse saturation for 1800s and ensuring that the loop was unaltered when remeasured. Through these measurements it was expected that the evolution of the hystesis loop from that typically expected for CoFe would be observed.

6.3.1 Effect of the Easy Axes Distribution of $IrMn_3$

The first step in the procedure was to measure the Cu/CoFe and NiCr/CoFe samples. This is because of the well-established relationship between seed layer grain size and the magnetic properties of CoFe [132–137]. An increase in the coercivity of the CoFe is expected between

the samples grown on the Cu and NiCr seed layers following the increase in D_m from 7.3 to 8.8nm and change in texture from polycrystalline to fibrous (110).

The results for the CoFe grown on the Cu and NiCr seed layers are shown by the black curves in figures 6.6 a) and 6.6 b) respectively. The loops are characteristic of a typical CoFe film displaying strong intergranular exchange coupling. However the values of H_c observed are 43 and 290Oe for the CoFe grown on Cu and NiCr respectively which is an increase of a factor 6.7. In the works of Vopsaroiu et al. and Platt et al. [132–134] an increase in H_c was observed with grain size whilst in the work of Jung et al. [135–137] a decrease in H_c was observed when the CoFe layer was deposited on a Cu seed layer. Growing the sample on a Cu seed layer changed the texture in the CoFe layer from (100) to (110) and decreased the grain size from 50nm to $\sim$9nm. This decrease in H_c was thought to occur due to the grain size of the CoFe being less then the exchange length L_{ex} given by

$$L_{ex} = \sqrt{\frac{A_{es}}{K_1}} \tag{6.2}$$

where A_{es} is the exchange stiffness and K_1 is the anisotropy constant of the F layer [138]. However this model [138] and the related experiments [132–137] do not predict or show as large a change in H_c with grain size as that found in this work. Therefore the change in H_c

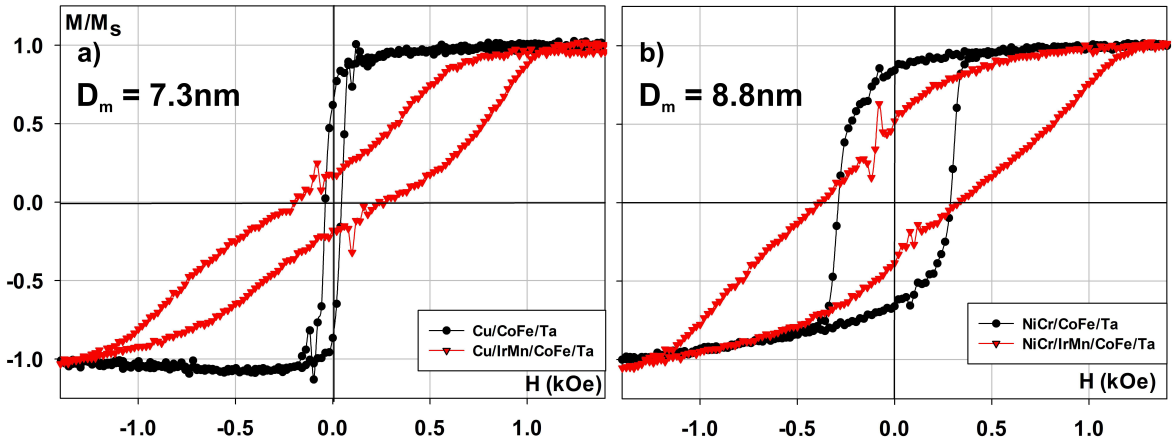

Figure 6.6: As deposited loops for the samples a) Cu/CoFe and Cu/IrMn/CoFe and b) NiCr/CoFe and NiCr/IrMn/CoFe.

cannot be explained by the grain size alone.

The process of magnetisation reversal in these samples is domain wall nucleation and motion as seen by the black loops in both figures 6.6 a) and 6.6 b) where the Cu/CoFe sample has weaker domain wall pinning than in the NiCr/CoFe sample. The median grain diameters for the samples grown on the Cu and NiCr seeds were 7.3 and 8.8nm with standard deviations of 0.33 and 0.35 respectively as shown in table 6.3. A change in grain diameter and standard deviation of 1.5nm and 0.03 can not account for a difference in H_c between the Cu/CoFe and NiCr/CoFe samples of 43 and 290Oe respectively. Furthermore the film roughness was found to be greater for the samples deposited on a Cu seed layer which would be expected to generate stronger domain wall pinning. The cause for the difference in the magnitude of H_c is therefore not due to any change in the granular structure or roughness and is not immediately obvious. However the change could be due to a distribution of the magnetocrystalline easy axes. In the case of the CoFe deposited on the NiCr seed layer there is a strong (110) in-plane texture. In a BCC material such as CoFe the magnetocrystalline easy axis lies along the $<100>$ direction which for this film will point out of plane. Therefore there will be a wide distribution of domain wall pinning sites. For the sample grown on the Cu seed layer where there is poor texture a large percentage of the CoFe grains will be (100) in-plane. The magnetocrystalline easy axis will therefore be in-plane decreasing the number of domain wall pinning sites.

The second step in the procedure was to measure the as deposited (unset) Cu/IrMn/CoFe and NiCr/IrMn/CoFe samples shown by the red hysteresis loops in figures 6.6 a) and 6.6 b) respectively. From these loops it is clear that the CoFe couples strongly to the $IrMn_3$ layer and that the anisotropy of the $IrMn_3$ has a significant effect on the CoFe. In the case of

Structure	H_c ($\pm$2.5Oe)	H_{ex} ($\pm$2.5Oe)	M_r/M_s	D_m ($\pm$0.5nm)	σ ($\pm$0.02)
Cu/CoFe	43	0	0.75	7.3	0.33
Cu/IrMn/CoFe	210	10	0.19	7.7	0.35
NiCr/CoFe	290	0	0.75	8.8	0.36
NiCr/IrMn/CoFe	350	10	0.45	10.2	0.45

Table 6.3: Results for the seed/CoFe and as deposited seed/IrMn/CoFe samples.

the sample grown on the Cu seed layer H_c increases from 43Oe for just Cu/CoFe to 210Oe for Cu/IrMn/CoFe. This is acompanied by a decrease in squareness from 0.75 to 0.19. The shape of the loop is due to the CoFe coupling to the randomly orientated $IrMn_3$. As shown in the previous sections the texture in the $IrMn_3$ is poor and so the magnetocrystalline anisotropy along the $<111>$ direction will be distributed in three dimensions. Therefore from saturation, reverse domains will form easily due to the CoFe coupling to some AF grains which are orientated in directions other than that of the saturating field. Due to the intergranular coupling in the CoFe thin film it will attempt to reverse via domain wall motion. However the number of pinning sites and their strength is large leading to a significant increase in H_c.

In the case of the sample grown on the NiCr seed layer H_c increases from 290Oe for NiCr/CoFe to 350Oe for NiCr/IrMn/CoFe again accompanied by a decrease in squareness from 0.75 to 0.45. The loop obtained is similar to that of the sample grown on the Cu seed layer. This is due to the strong (111) in-plane texture induced in the $IrMn_3$ by the NiCr seed layer giving a two dimensional in-plane random distribution of the magnetocrystalline anisotropy directions. This modifies the loop through an additional 2D randomly distributed unidirectional anisotropy on top of the CoFe cubic anisotropy. In this case those AF grains oriented in directions other than that of the saturating field provide nucleation sites for reverse domains whilst an equal and opposite number maintain magnetisation leading to

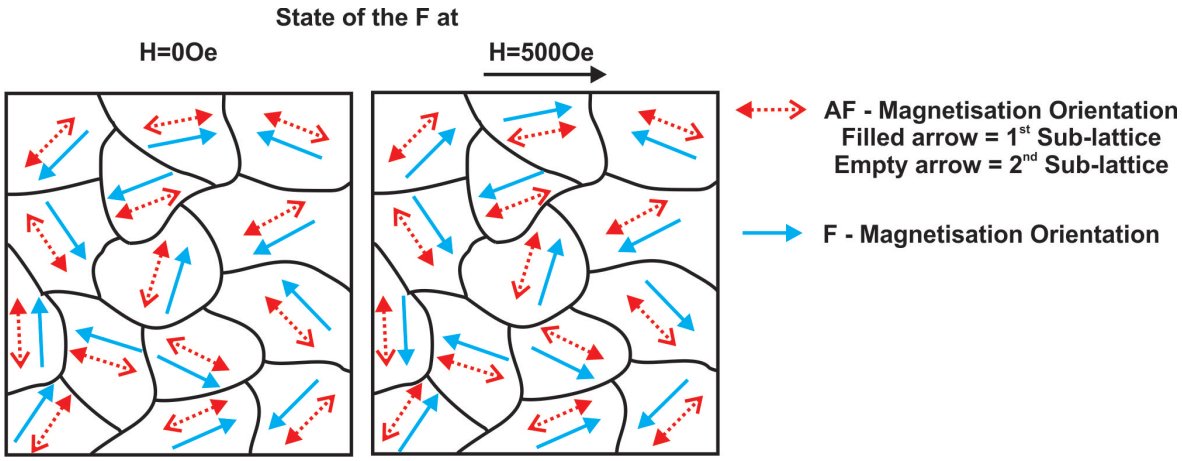

Figure 6.7: Schematic diagram of the state of the AF as deposited and the orientation of the F moments at H=0 and H=500Oe

a squarness of near 0.5. However H_c is little changed as the number of pinning sites will not have increased significantly. A schematic diagram showing the state of the F and AF magnetisation orientations in this system at fields H=0Oe and H=500Oe is shown in 6.7 along with a summary of the key results in table 6.3.

6.3.2 Effect of Setting

The third step was to anneal the samples in zero field however these graphs have been omitted. This is because during the annealing process the F layer had some degree of magnetisation leading to a partial setting of the AF that was irreproducible. Some attempts to 'demagnetise' the AF and F layers was made however this required a combination of AC demagnetisation and annealing/cooling which still led to irreproducible results. This confirms that the remanent magnetisation in the F layer is sufficient to at least partially set the AF. This is a convenient demonstration that the AF is at least partially set through the exchange interaction with the F layer and not the external applied field.

The fourth and final step of the procedure was to set the samples in a 5kOe field at a temperature T_{set}=498K for a time t_{set}=1800s. Two hysteresis loops were then measured to determine H_{ex} and the magnitude of the training effect ΔH_{c1}. The hysteresis loops for the sample grown on the Cu seed layer are shown in figure 6.8 a) displaying a loop shift of H_{ex}=630Oe for loop 1 and 605Oe for loop 2. The increased coercivity is also maintained from the as deposited measurement with H_c=230Oe for loop 1 and 195Oe for loop 2. Interestingly the magnitude of H_c for the set loops is similar to that obtained for the as deposited loop where H_c=210Oe.

The hysteresis loops for the sample grown on the NiCr seed layer shown in figure 6.8 b) have loop shifts H_{ex}=350 and 340Oe for loops 1 and 2 respectively. This is less than that obtained for the sample grown on the Cu layer despite what might be expected from a sample with a better (111) texture in the $IrMn_3$ layer. However this is because the $IrMn_3$ grown on the NiCr seed has a higher effective anisotropy K_{AF} than that of the sample grown on the Cu seed layer as shown in the work of Aley et al. [17]. Furthermore V_m for the sample grown on the NiCr seed layer was measured to be (820$\pm$90)nm^3 which is twice that of (470$\pm$52)nm^3 obtained for the sample grown on the Cu seed layer. Therefore the

lower value of H_{ex} is probably due to some unset fraction of the AF where

$$H_{ex}(T_{ms}) \propto \int_{V_C(T_{ms})}^{V_{set}(T_{ms})} f(V)dV \neq 1 \tag{6.3}$$

In order to have fully set the larger grains in the distribution sufficient energy to overcome the energy barriers to reversal for the larger grains must be applied [4]. However the temperatures required to do this would lead to significant interlayer diffusion and therefore degradation of the film. The distribution not being fully set could also explain the large coercivities of H_c=450 and 445Oe obtained for loops 1 and 2 respectively. It is the remaining unset grains which create addition pinning sites giving a lower effective 'squareness' to that in the sample grown on the Cu seed layer and a coercivity greater than that of the as deposited sample of H_c=350Oe.

The observed changes in H_{ex} and H_c between loops 1 and 2 is due to the training effect [80,95]. Before the development of the York Protocols the training effect was observed over multiple loops to follow a trend of the form

$$H_{ex} - H_{ex\infty} \propto \frac{1}{\sqrt{n_l}} \tag{6.4}$$

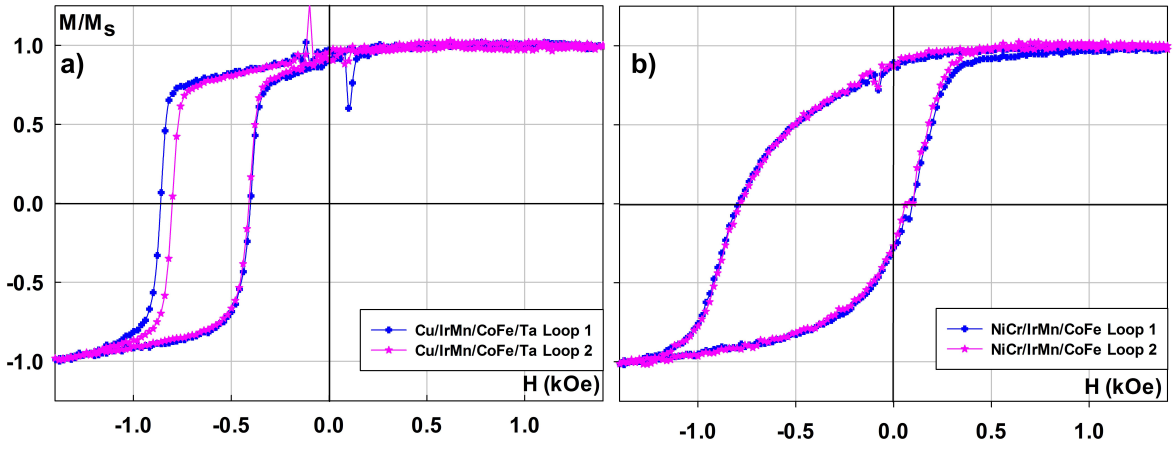

Figure 6.8: The first and second loop measured after annealing of the a) Cu/IrMn/CoFe and b) NiCr/IrMn/CoFe samples.

where $H_{ex\infty}$ is the value of H_{ex} measured after a number of consequent loops $n_l \Rightarrow \infty$ [80, 139, 140]. However this was an artifact due to thermal activation of the AF layer over the course of the measurements [27, 95]. Furthermore when measured at T_{na} the training effect is observed only as a change in the first reversal of the loop to negative saturation ΔH_{c1}. For the Cu/IrMn/CoFe and NiCr/IrMn/CoFe samples ΔH_{c1} was found to be 60 and 10Oe respectively. For the sample grown on the NiCr seed layer this change is almost within error. Given the samples are measured at T_{na} no change in H_{c2} is expected. For the sample grown on the Cu seed layer a 10Oe change is observed and although this is also almost within error there could still be a small active portion of the AF due to the lower effective anisotropy of the AF as shown in the work of Aley et al. [17]. A summary of these results is shown in table 6.4.

The origin of the training effect derives from the order and disorder in the spin clusters as described in the conceptual model of chapter 3.10 and reproduced schematically in figure 6.9 [27, 56]. On setting, the clusters are aligned analagous to that of a Thermoremanent Magnetisation (TRM) state [88]. A TRM state occurs when field cooling materials such as spin glasses which in the works of Baltz et al. [46] and Fernandez-Outon et al. [45] have been shown to behave in a manner similar to that of the interface in exchange biased systems. During the first field reversal after setting, some of the interfacial clusters are expected to reverse with the F layer and so disorient with respect to the initial TRM state. At negative saturation these clusters are now in an Iso-Thermalremanent Magnetisation (IRM) state. When returned to positive saturation H_{c2} derives from reorientation of some or all of the clusters. Hence at positive saturation some of the interfacial spin clusters will remain disoriented as no thermal annealing is now undertaken. This reduction of spin cluster

Structure	H_{ex} ($\pm$2.5Oe)	H_c ($\pm$2.5Oe)	H_{c1} ($\pm$2.5Oe)	H_{c2} ($\pm$2.5Oe)	M_r/M_s
Cu/IrMn/CoFe Loop 1	630	230	-860	-400	0.81
Cu/IrMn/CoFe Loop 2	605	195	-800	-410	0.80
NiCr/IrMn/CoFe Loop 1	350	450	-798	100	0.69
NiCr/IrMn/CoFe Loop 2	345	445	-788	100	0.69

Table 6.4: Summary of key results for the set seed/IrMn/CoFe samples for the first and second loops.

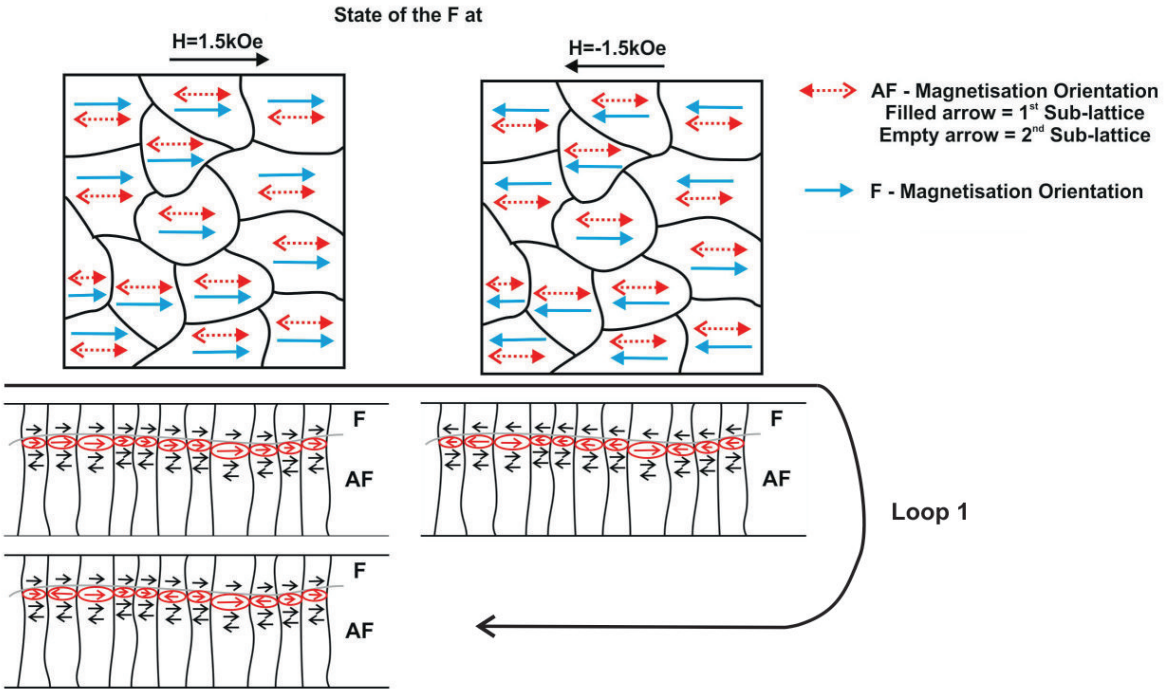

Figure 6.9: Schematic diagram of the state of the AF,F and interface moments during measurement of the first loop post field setting.

ordering leads to a decrease in H_{c1} in the subsequent loops and hence training. This gives a new definition of H_{c1} and H_{c2} different from that which applies to a classical ferromagnet. In a typical ferromagnetic material the reversal processes are symmetric. However in an exchange biased material first loop reversal is asymmetric due to the setting process giving H_{c1} and H_{c2} as being due to different processes. Therefore the coercivities observed are a manifestion of the energy barriers present in the spin clusters the ordering of which moderates the interfacial coupling. This is expressed in the York Model by the variable C^* in the equation

$$H_{ex}(H_{set}, T_{set}) = H_{ex}^{i} C^*(H_{set}, T_{set}) \int_{V_c(T_{meas})}^{V_{set}(T_{set})} f(V) dV \tag{6.5}$$

From the data in figure 6.8 a) and b) there is clearly some correltation between the type of seed layer used and various phenomena in the resulting hysteretic behaviour. In summary

the following facts are known:

1. For the sample grown on the NiCr seed layer perfect (111) in-plane texture appears to result for the $IrMn_3$ according to the X-ray data (6.2). This will result in a 2-D random distribution of easy axis directions in the $IrMn_3$. This orientation is known to give the AF grains a very high value of K_{AF} [17].

2. For the sample grown on a Cu seed layer the X-ray data indicates a 3-D random distribution of easy axis directions in the $IrMn_3$ (6.2). This results in a modest value of K_{AF} for the $IrMn_3$ grains.

3. The first 2 loops for the sample grown on NiCr give a rounded loop with H_{c1} of -798Oe and H_{c2} of 100Oe giving H_c=450Oe. No training is observed and the loop is not fully square (M_r/M_s=0.69).

4. For the sample grown on Cu H_{c1}=-800Oe, a similar value to that for the sample grown on the NiCr however H_{c2} is now -410Oe. Significant training of ΔH_{c1}=60Oe is observed. The loop is now almost perfectly square (M_r/M_s=0.81).

These key parameters are summarised in table 6.4. As mentioned above the samples were measured at T_{na} and hence the properties observed cannot be due to changes in the bulk of the AF grains and must be due to changes in the interfacial spin clusters. It is now possible to construct a hypothesis describing the behaviour of the clusters in terms of the variation of their anisotropy, which derives from the AF anisotropy, and the effect of cluster-cluster interactions. Consider a 1-D chain of spin clusters as shown in figure 6.10

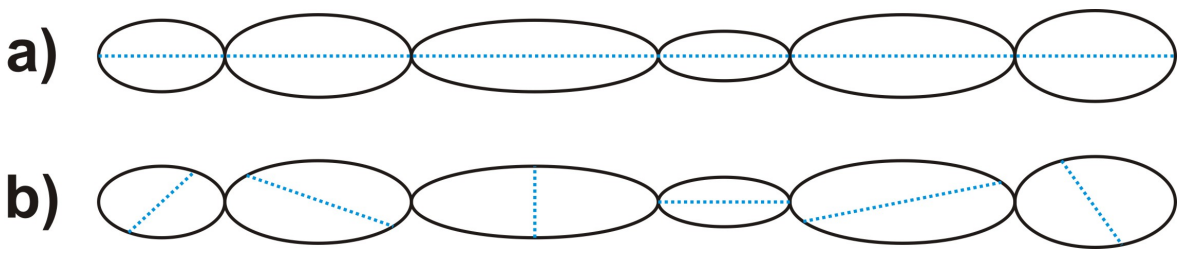

Figure 6.10: Schematic diagram of the cluster easy axis in a 1-D chain for a) in-plane and b) randomly ordered easy axis.

where in a) the easy axes lie exclusively along the chain. In b) the easy axes now are now randomly distributed in orientation. The clusters behave as Stoner-Wohlfarth particles and are interacting. If this hypothesis is correct there should be a large change in the H_{set} and T_{ms} dependence of H_{ex}, H_c and the training effect with seed layer.

6.4 The Setting Field Dependence of H_{ex}

The magnitude of H_{ex} is known to change with H_{set} as described in detail in chapter 3.10 [25, 26]. From the previous experiment it is thought that the interfacial clusters in a highly textured F/AF film behave similar to that of a 2-state system whilst a poor texture gives a biaxial system with a distribution of anisotropies. This should be reflected in the H_{set} dependence of H_{ex}, H_c and ΔH_{c1}. If this is the case then H_{ex} will give some indication of the order of the clusters whilst H_c and the training will be representative of their initial/final order after field cooling and following reversal at low temperature. Therefore in the case of interfacial spin clusters in a film with good in-plane texture an increase in H_{ex} with H_{set} is expected with little change in H_c and no training with the opposite occuring in films with

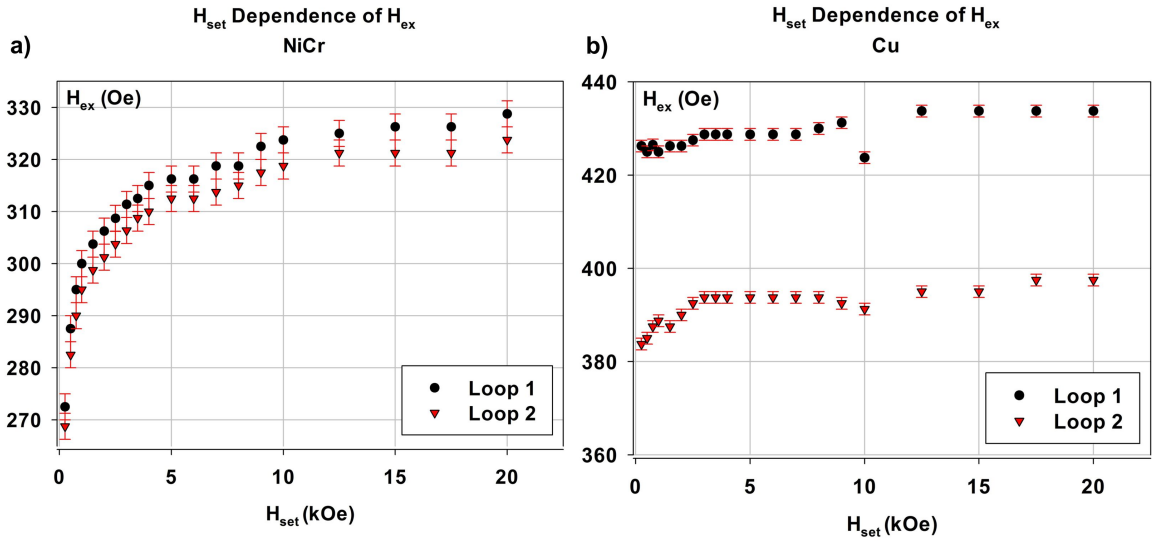

Figure 6.11: The H_{set} dependence of H_{ex} for the samples grown on a a) NiCr and b) Cu seed layer.

a poor in-plane texture.

To test this two new samples of structure X(x)/IrMn(10)/CoFe(3)/Ta(5) were deposited where X were the seed layers NiCr and Cu of thicknesses x=7.5 and 5nm respectively. To measure the samples they were first annealed with the conditions H_{set}=250Oe, T_{set}=498K for t_{set}=1800s and then cooled in field to T_{ms}=173K. Two hysteresis loops were then measured in order to observe the training effect. This process was repeated in steps of H_{set} up to 20kOe. After annealing and field cooling care was taken to ensure that the F layer did not undergo any reversal before measurement of the first loop. This was done in order to preserve the initial spin state of the interface.

The H_{set} dependence for the NiCr/IrMn/CoFe sample shown in figure 6.11 a) gives a similar behaviour to that reported by Fernandez-Outon et al. [25, 26]. Taking H_{ex} at 250Oe and 20kOe a change of 55Oe is seen following a trend similar to that described by the Langevin function as discussed in chapter 2.2 and reproduced below to the first term [34, 141]

$$L(a_L) = \frac{a_L}{3} = \frac{\mu_m H}{3k_B T} \tag{6.6}$$

Identical behaviour is seen for both loops 1 and 2 within error. There is no change observed in H_c and ΔH_{c1} with H_{set} as shown in figures 6.12 a) and 6.13 a). A small ΔH_{c1} of 10Oe is also seen which is identical to that of the sample measured in the previous section. This result shows that the sole change in the interfacial clusters is that of an increase in ordering.

In the case of the Cu/IrMn/CoFe sample as shown in figure 6.11 b) a change in H_{ex} of only 10Oe is seen for the first loop from H_{set}=250Oe to 20kOe. The behaviour of loop 1 is different from that of loop 2 where the change in H_{ex} with H_{set} is 15 Oe with a shape more similar to that of the sample grown on the NiCr seed layer. This difference between the two loops is because the first loop takes into account the clusters with H_K out of plane. In the second loop the clusters with anisotropy out of plane are disoriented and do not contribute emphasising the increased ordering for the clusters with H_K in the plane of the film.

The change in H_c and ΔH_{c1} with H_{set} for the sample grown on a Cu seed layer are shown in figures 6.12 b) and 6.13 b) respectively. A change in H_c of 5 and 10Oe was

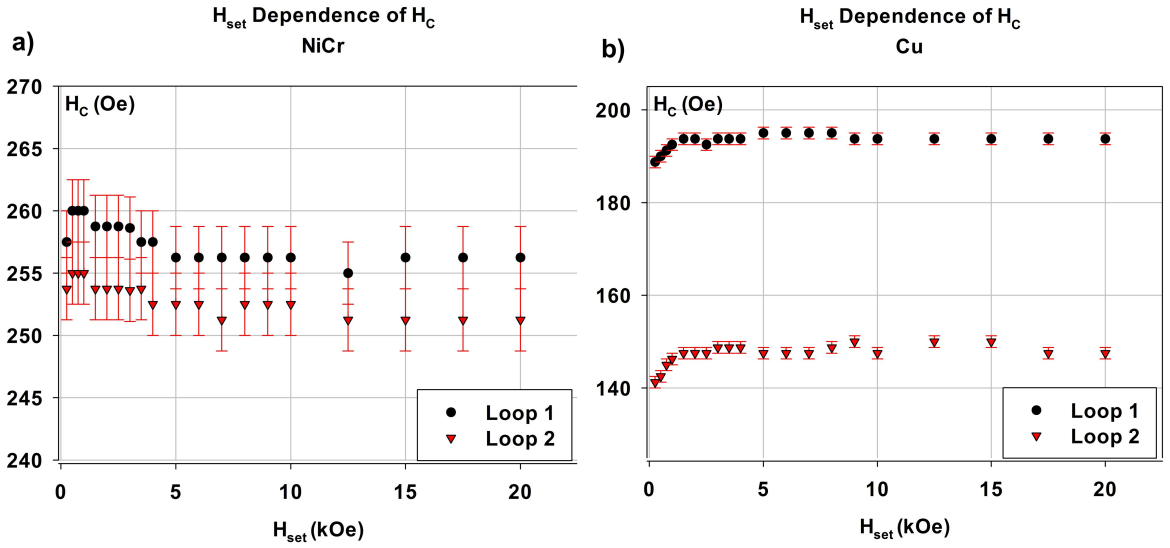

Figure 6.12: The H_{set} dependence of H_c for the samples grown on a a) NiCr and b) Cu seed layer.

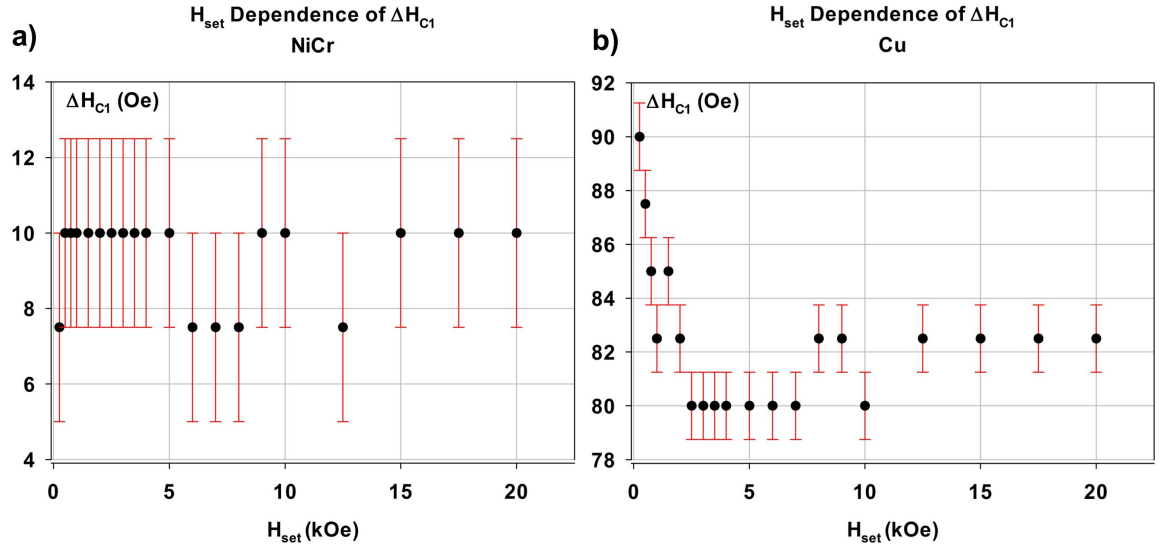

Figure 6.13: The H_{set} dependence of training in H_{c1} for the samples grown on a a) NiCr and b) Cu seed layer.

measured for loops 1 and 2 respectively. Whilst the change in loop 1 is within error the change in loop 2 is ∼7.5% of the total value of H_c. Coupled with a change of 10Oe in ΔH_{c1} with setting field this implies that there is some increase in the stiffness or stability of the clusters. This increase in the order of the interfacial spin clusters could be due to some of the clusters with H_K in-plane that are otherwise disorderd, perhaps by neighbours clusters with H_K out of plane. In the sample grown on a Cu seed layer the increased ordering of the clusters with H_K in-plane works to increase the stability of the neigbouring clusters giving an increase in H_c and a decrease in ΔH_{c1}.

A summary of these results are shown in table 6.5. Clearly there is an H_{set} dependence of H_{ex}, H_c and ΔH_{c1} which varies depending on the state of the interface. In this experiment the interface was controlled by changing the texture of the $IrMn_3$, and by extension CoFe, layers from full disordered to in-plane (111) and (110) texture respectively. It is clear that in the strongly texture films, in this case those grown on a NiCr seed layer, that the interface is significantly stiffer showing a larger dependence on H_{set} and less prone to change during the course of the measurement. The opposite has been found to be true for the samples with poor texture, in this case those grown on a Cu seed layer, where there is no significant increase in interfacial order with H_{set} and large changes are observed during the course of the measurement i.e. ΔH_{c1}. This has been confirmed to not be due to changes in the

Structure	H_{ex} @500Oe (±2.5Oe)	H_{ex} @20kOe (±2.5Oe)	H_c @500Oe (±2.5Oe)	H_c @20kOe (±2.5Oe)	ΔH_{c1} @500Oe (±2.5Oe)	ΔH_{c1} @20kOe (±2.5Oe)
NiCr/IrMn Loop 1	275	330	260	255		
NiCr/IrMn Loop 2	270	325	255	250	10	10
Cu/IrMn Loop 1	425	435	190	195		
Cu/IrMn Loop 2	385	400	140	150	90	80

Table 6.5: Summary of the key results for the H_{set} dependence of H_{ex} for the Seed/IrMn/CoFe samples.

bulk AF grains as shown in the work of Fernandez-Outon et al. [26] and guaranteed by carrying out the measurements at T_{na}. These results further strengthen the concept that the mechanism of the interface is analagous to that of a system of fine particles. This spin cluster hypothesis appears to explain the results well however a model must be developed in order to test its validity.

Chapter 7

Effect of Nano Patterning on Exchange Bias

Read heads have made use of exchange bias to pin a reference F layer since the introduction of GMR read heads in 2000 [8]. Since then read heads have decreased in lateral dimensions to sub-100nm which is approaching that of 5 by 5 grains of a typical size of $\sim$6nm used in industrial materials. As has been established in chapters 3 and 6 exchange bias in granular films is dependent on the grain volume distribution and the F/AF interface. Therefore in sub-100nm structures the interface will begin to play a larger role. Furthermore large structure to structure variations will occur due to a distribution of the grain volume distributions.

Despite continued work over the past 15 years exchange bias in sub-100nm structures is not well understood. This is due in part to the large variety of materials, geometries, fabrication methods, and measurement techniques [18]. However as this work is concerned primarily with polycrystalline $IrMn_3$ films this will be the sole focus.

Three primary fabrication methods exist: lift-off [106, 142, 143], patterning and etching [19, 21, 22], and pre-patterned substrates [20]. The first two methods are described in detail in chapter 4 whilst the pre-patterned substrates function similar to that of a sample fabricated via lift-off. A decrease in H_{ex} and T_b with element size is seen across all methods apart from one variation in lift-off where the mask was formed via nanosphere lithography [142]. The observed increase in H_{ex} has been attributed to a change in the thickness of the layers as part of the fabrication process [18].

In earlier studies [19–22] the decrease in H_{ex} and T_b with element size was attributed to domain wall pinning in the AF. In the work of Baltz et al. [22] the thickness of the AF was varied for arrays of square elements with a lateral size of 90nm. No change in T_b with respect to the continuous film was observed for AF thicknesses greater than 14nm. Below t_{AF}=14nm the difference in T_b between the patterened and continuous films was found to increase linearly with decreasing t_{AF}. This shows that the decrease in H_{ex} and T_b is due to a change in the grain volume distribution of the elements. It was later proposed by Vallejo-Fernandez et al. [28, 29] and Baltz et. al. [144] that cutting of edge grains during the fabrication process led to a reduction of the median grain diameter D_m of the patterned structures. Vallejo-Fernandez et al. produced a model which was a modification of the York Model [28] in which each element has its own grain diameter distribution where any edge grains are cut giving an effective decrease in D_m. This leads to both an overall decrease in, and wider distribution of, D_m when averaged across all the elements.

The measurement of nanostructures is a difficult task due to the significant reduction in measurable material. Most studies make use of magneto-optical Kerr effect magnetometery [19–22, 143] due to the difficulty of fabricating suitably large arrays to measure in a VSM. In this work a series of 4x4mm arrays of dots of different sizes have been produced in order to confirm the model of Vallejo-Fernandez et al. [28, 29]. These samples have been produced via the lift-off method as there is significant evidence that ion etching leads to effects such as grain growth at the edges [24] and damage due to ion impact [23].

7.1 Structure Fabrication

A Polymethylglutarimide (PMGI)/ZEP double layer resist was spun on Si(100) substrates and patterned into masks using a JEOL-JBX-6300FS e-beam lithography system. The PMGI/ZEP double layer resist was chosen so as to limit structure edge artifacts as described in detail in chapter 4. A set of five 4×4mm arrays of dots of size 80, 140, 225, 325, and 425nm were chosen in order to observe the transition from that of approximately a continuous film to a sub-100nm structure. A 3:1 ratio between dot diameter and element-element spacing was used in an attempt to limit dipole-dipole interactions. A film of structure Ta(2)/Ru(5)/IrMn(10)/CoFe(5)/Ta(2) (nm) was deposited on the masked substrates

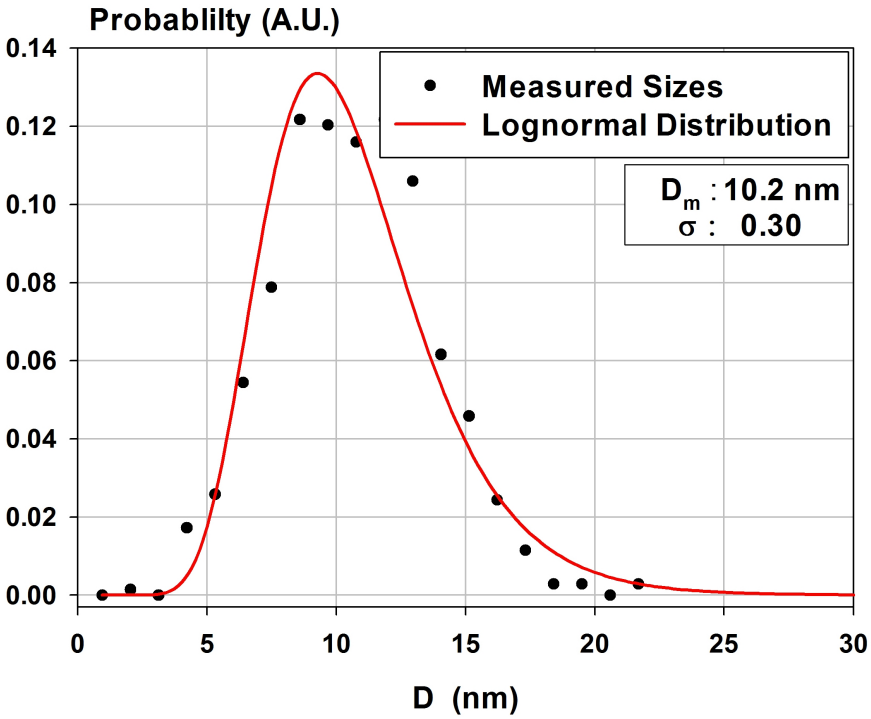

Figure 7.1: Measured grain diameter distribution for the continuous film where the line is the calculated lognormal distribution.

with lift-off carried out through soaking in cyclopentanone placed in an ultrasonic bath. A continuous film was also deposited for comparison to the patterned films. This particular layer structure was chosen for a number of reasons: 1) A Ta/Ru seed was chosen along with an $IrMn_3$ thickness of 10nm so that the distribution could be fully set at a temperature T_{set}=498K with T_{na}=298K. 2) The CoFe layer was made to be 5nm in order to maximise the moment of the sample without significant loss in H_{ex} which is known to follow a trend of $H_{ex} \propto 1/t_F$ [145]. 3) The thickness of the seed and capping Ta layers was minimised in order to limit deposition of material on the walls of the mask.

The grain size distribution for the film was measured and the lognormal distribution calculated and plotted as shown in figure 7.1.The films were found to have a D_m=(10.2±0.5)nm with a standard deviation of 0.30. The patterned films were inspected in an SEM in order to confirm size, spacing and overall array quality. A selection of images is shown in figure 7.2 for element sizes a) 80nm, b) 140nm, c) 325nm, and d) 425nm. For each element size a high and low magnification image is provided. Within the resolution of the SEM a 5%

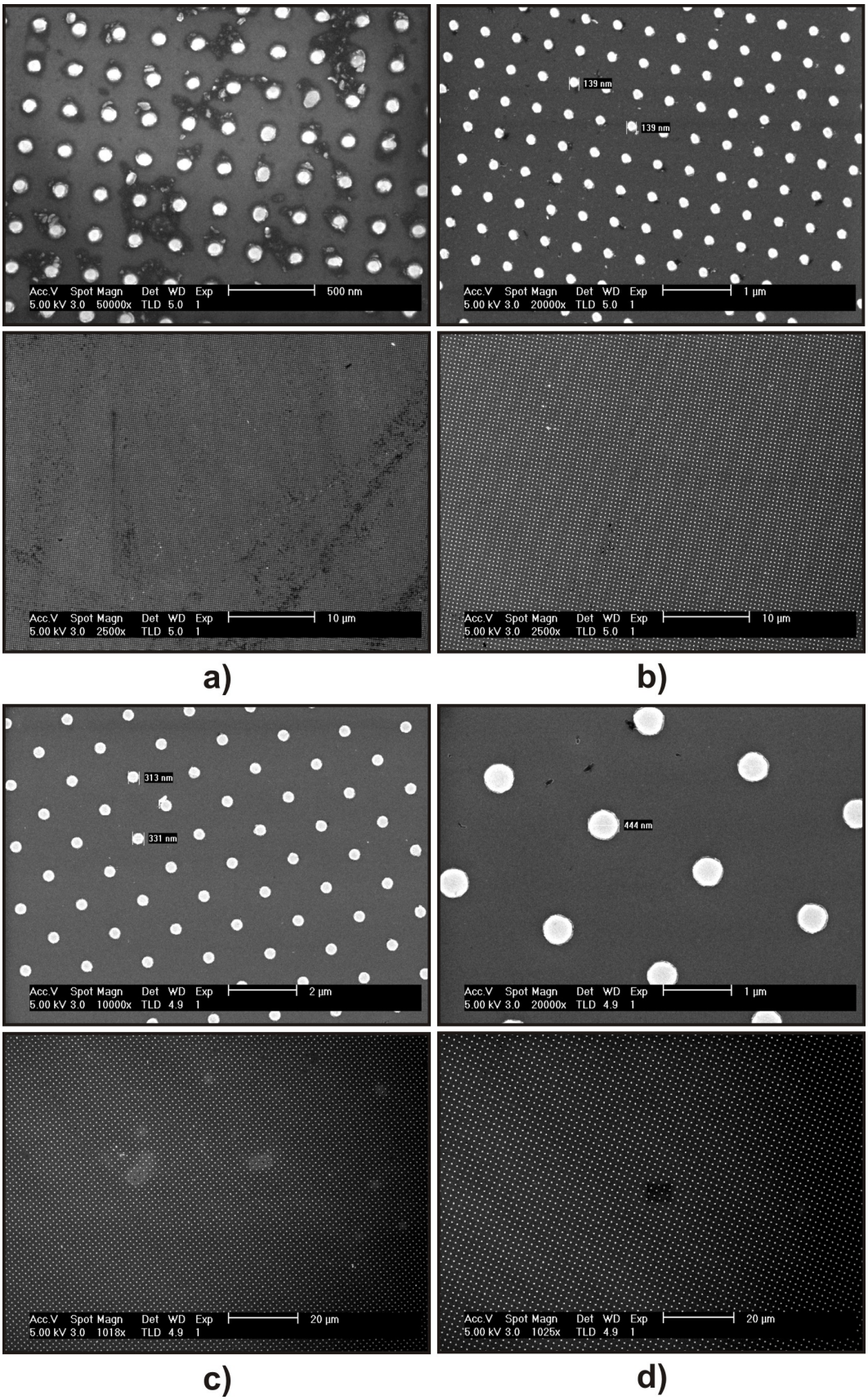

Figure 7.2: SEM images showing both a high magnification image for structure details and a low magnification image for array quality for dots of diameter a) 80nm, b) 140nm, c) 325nm and d) 425nm.

error in element diameter was measured for each size which translates into a 7% error in the element spacing. The arrays showed good ordering across the substrate apart from the outer few (5-10) rows of dots. This area of smaller dot sizes is a small fraction of the total area and is therefore unlikely to cause any significant variations in the final results. There was some damage to the arrays as a result of cutting the substrate for measurement in a VSM however this was again minimal.

In the arrays of 80 and 140nm dots a relatively large amount of debris is present in between the structures. This is most likely left over resist that was not fully cleared during the lift-off process. For the 80nm dots some appear to be significantly damaged. From figure 7.2 a) 3 of the $\sim$70 dots imaged have significant abnormalities. This is representative of the full array however how this would affect the final magnetic measurements is unclear. For all other element sizes above 140nm shape regularity was highly uniform.

7.2 Effect of Grain Cutting on Magnetic Properties

The magnetic and thermal properties of the continuous and patterned films were measured following the York protocols as described in chapter 5. The measurement parameters used were T_{set}=498K, t_{set}=5600s, t_{act}=1800s, and T_{ms}=298K where T_{ms}=T_{na} as measured for the continuous film. Due to the continuous flow cryostat design of the VSM T_{ms} could not be lowered below room temperature. This is because on patterning, the moment of the sample decreased from $\sim$0.125memu for the continuous film to $\sim$10μemu for the 80nm dots which is near the noise base of 5μemu for the VSM. The gas flow required to cool the sample caused sufficient disruption to the sample to make the patterned samples unmeasurable requiring the samples to be measured at room temperature.

The effect of the element diameter on H_{ex} is shown in figure 7.3. The change in H_{ex} with element size is similar to that as reported in other works [143,144] where no significant change in H_{ex} with element size occurs until sub-200nm. However this behaviour is observed after the value of H_{ex} decreases on patterning from 302Oe for the continuous film to $\sim$100Oe for the 225, 325, and 425nm dots. This discrepancy could be due to a distribution of element shapes which is not taken into account in the calculations. Non-uniformities around the edges of the elements could lead to differences in the nucleation field and hence

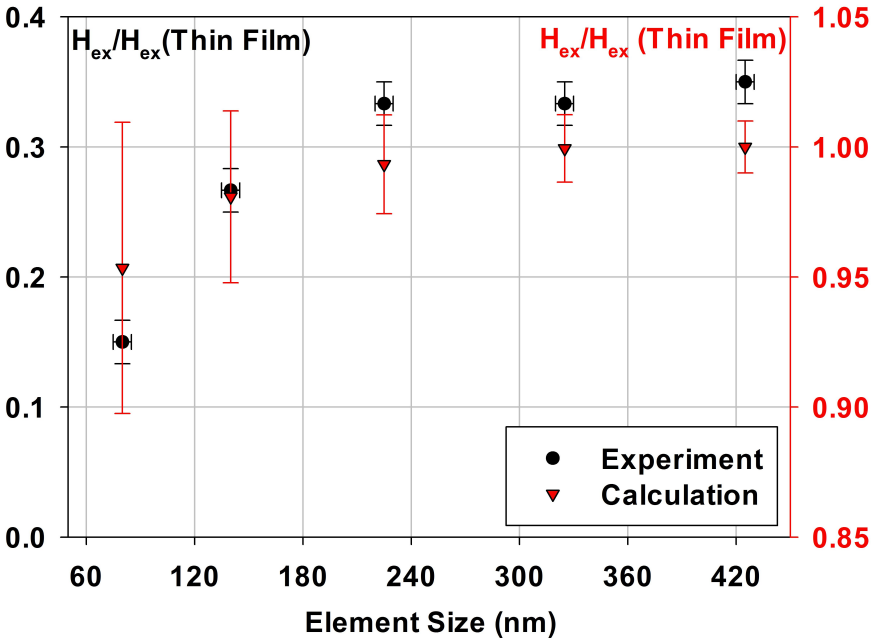

Figure 7.3: Change in H_{ex} with element size where the right y-axis corresponds to the calculated values and the left y-axis the measured values.

switching fields across the array lowering the value of H_{ex}. Dipole interactions between the elements could also cause a decrease in the switching field, however the spacing between the elements should cause this effect to be negligible. Furthermore edge roughness or asperities could vastly affect the distribution of properties across the structures.

The experimental results were compared to calculation using the model of Vallejo-Fernandez et al. [28, 29]. This model is a modification of the York model of exchange bias whereby the AF is modelled as granular with a distribution of diameters following a lognormal distribution with parameters D_m and σ. The model assumes that during the patterning process grains at the edges of the nanostructures will be cut randomly. This leads to an effective grain size distribution for each element that may differ significantly to that of the thin film. To calculate this an array of grains randomly distributed in diameter are generated. A circle equal to the element size is then drawn with any grains outside the boundary being removed. Any grains that are cut by the element boundary have their areas modified accordingly. The value of the exchange bias is then calculated by integrating over

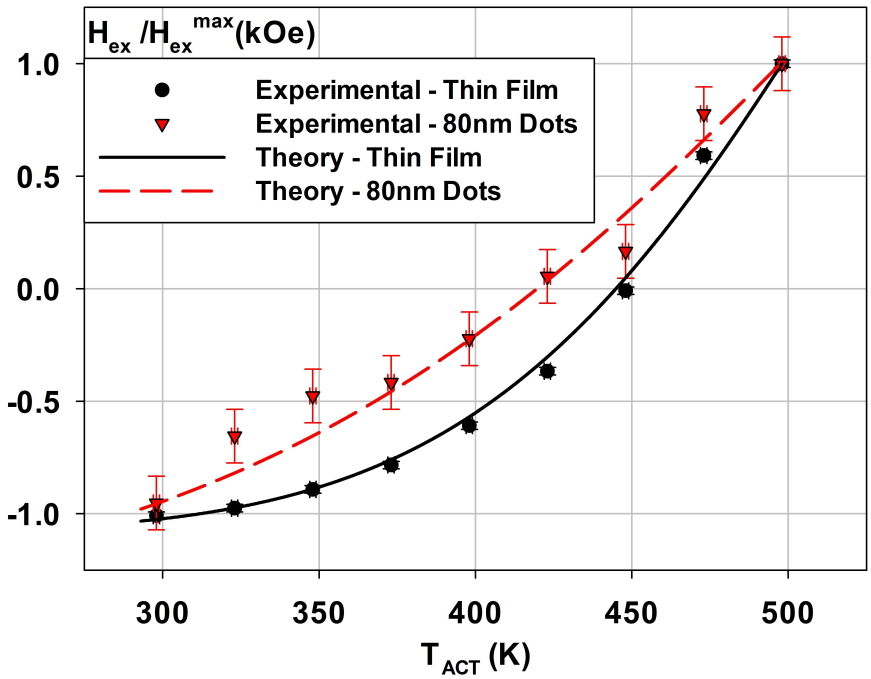

Figure 7.4: The measured distribution of T_b for the (black) continuous film and (red) 80nm dots where the line is the calculated distribution.

the AF grain volume distribution as discussed in chapter 3 and reproduced below.

$$H_{ex}(T_{ms}) \propto \int_{V_C(T_{ms})}^{V_{set}(T_{ms})} f(V)dV \tag{7.1}$$

This process is repeated over 10 000 elements to ensure good statistics. For the model the measured values of K_{AF}=6.5$\times$10^6 ergs/cc, D_m=10.2 nm, and σ=0.30 were used. The rest of the simulation parameters were: T_{set}=498K, T_{na}=293K, T_N=650K, t_{set}=5600s, t_{ms}=100s and f_0=2.1$\times$10^{12}s^{-1} [60].

The trend in H_{ex} is predicted to decrease with smaller element size which is in qualitative agreement with the data shown in figure 7.3 however the absolute values of H_{ex} were incorrect. This discrepency could either be due to an error in the grain size distribution of the elements or the interface. It is likely that the patterned films were thermally active during the course of the measurement, however the model takes this into account. Therefore it is likely that structure edge roughness or a damaged interface are the cause of the significant

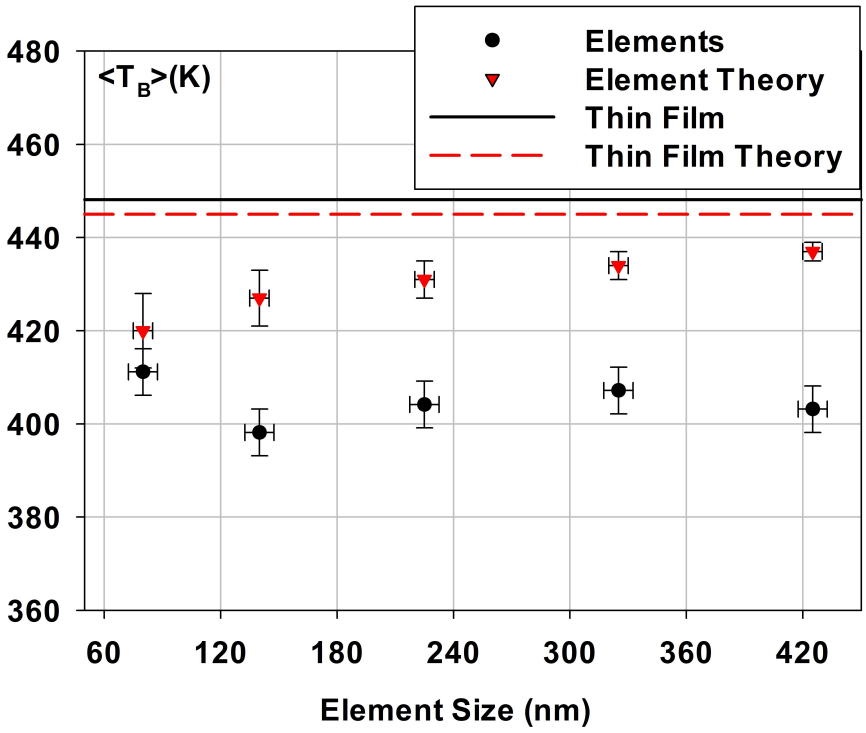

Figure 7.5: The measured (black) and calculated (red) change in $\langle T_b \rangle$ with element size where the lines correspond to the value of the continuous film.

decrease in H_{ex} on patterning. The error bars for the calculated values in figure 7.3 represent the standard deviation of H_{ex} for a given element size. Clearly any edge effects, particularly in sub-100nm elements, will greatly affect the distribution of H_{ex}.

The thermal stability of the nanostructures was quantified in terms of their distribution of blocking temperatures. The distribution of blocking temperatures for the continuous film and the 80nm elements are shown in Figure 7.4 where the solid and dashed lines correspond to calculated values. There is good agreement between theory and experiment however it is important to note that this is with the absolute values of H_{ex} scaled.The shape of the distribution is however an excellent fit with the values of the median blocking temperature $\langle T_b \rangle$ in relative agreement. Therefore it is the value of $\langle T_b \rangle$ that will be used to quantify the thermal stability of the nanostructures.

The experimental and calculated $\langle T_b \rangle$ for all samples is shown in Figure 7.5 where $\langle T_b \rangle$ is shown to decrease from 448K for the continuous film to $\sim$405K for the patterned systems.

No change is observed in $\langle T_b \rangle$ with element size apart from the initial patterning process. A gradual decrease is predicted by the model however the scale of the values is in good agreement. In the work of Sasaki et al. [143] a decrease in $\langle T_b \rangle$ from 360K to 330K is observed with element size from 400 to 100nm. However this was for a FeMn/NiFe system and furthermore the element spacing was less than the diameter and so element-element interactions could occur.

From these results it is clear that the reduction in H_{ex} is a consequence of a modification of the interface by the patterning process. The median blocking temperature is dominated by bulk effects and has been shown to be independent of interfacial effects [4,26]. However H_{ex} at a given temperature will be moderated by interfacial effects which are, in the case of nanodots, expected to be more significant than for the thin film case due to the restricted dimensions of the elements. Also as a double layer resist was used it is unlikely that the material deposited will be perfectly planar. This will lead to a film which is thicker at the centre compared to the edges therefore causing a domed interface between the F and AF layers.

During fabrication a major difficulty encountered was deposition of material on the resist walls. This leads to an effective minimum element size that is equivalent to twice the deposited film thickness. As element sizes of $<$20nm are required for technological applications this sets a maximum film thickness of 10nm. The film thickness used in this work was 24nm and as seen in the results, a summary of which is shown in table 7.1, a decrease in H_{ex} and $\langle T_b \rangle$ of 262Oe and 37K occurs for an element size of 80nm. Any attempts to decrease the film thicknesses to those required for 25nm structures leads to

Element Size	H_{ex} ($\pm$5Oe)	Calculated H_{ex} ($\pm$5Oe)	$\langle T_b \rangle$ ($\pm$5K)	Calculated $\langle T_b \rangle$ ($\pm$5K)
Continuous Film	302	553	448	445
425nm	105	553	403	437
325nm	100	553	407	434
225nm	100	549	404	431
140nm	90	542	398	427
80nm	40	527	411	420

Table 7.1: Summary of key results for dot size dependence of H_{ex}.

sample characteristics that are not suitable for applications. There are potential ways around this issue in the case of lift-off fabrication e.g. utilising seed layers to increase the AF anisotropy. However for maintaining simplicity of fabrication with freedom of layer structure, use of a hard masks and etching are required.

7.3 Etching of Exchange Biased Nanostructures

A preliminary measurement has been carried out in order to compare the difference in magnetic properties of nanostructures fabricated through lift-off and etching. In the work of Basith et al. [24] a comparison of the magnetic properties of NiFe nanowires patterned by e-beam lithography with lift-off and ion beam milling was carried out. A major finding of this study was the secondary grain growth in the wires due to milling. These grains were of diameters between 20-30nm and formed up to 30-40nm from the edge of the wires. However as the wire widths were 320-150nm this was only an edge effect. This was reflected as a minor change in domain wall characteristics. In the case of dots the percentage of the total area that will experience secondary grain growth will be greater. This is particularly the case in dots of diameter $<$100nm where grain growth will occur throughout the entire structure. This is expected to have large implications for an exchange bias system were H_{ex} and $\langle T_b \rangle$ are dependent on the AF grain volume [4].

In the work of Read et al. [23] an exchange biased system of structure UL/IrMn(5.5)/Co-Fe(t_F)/Ag(4) (nm) was deposited and treated to an ion etch. A significant decrease in H_{ex} was observed when the etch depth came within $\sim$3nm of the CoFe/IrMn interface. This was thought to be due to implantation of Ar, Co/Fe and capping layers e.g. Ag at the IrMn/CoFe interface. Therefore whilst the fabrication process of etching through a hard mask will allow for high quality film growth it is clear that significant changes in the film structure can occur in later processing steps. In order to test this an identical film to that in the previous section of structure Ta(2)/Ru(5)/IrMn(10)/CoFe(5)/Ta(2) (nm) was deposited on a 20mm Si substrate. A negative resist ma-N 2408 was spun on the films and patterned into three 4$\times$4mm arrays of dots of size a) 140nm, b) 240nm, and c) 440nm which were then treated to an Ar ion etch. This process is described in detail in chapter 4. As done for the samples produced via lift-off the patterned films were inspected in an SEM

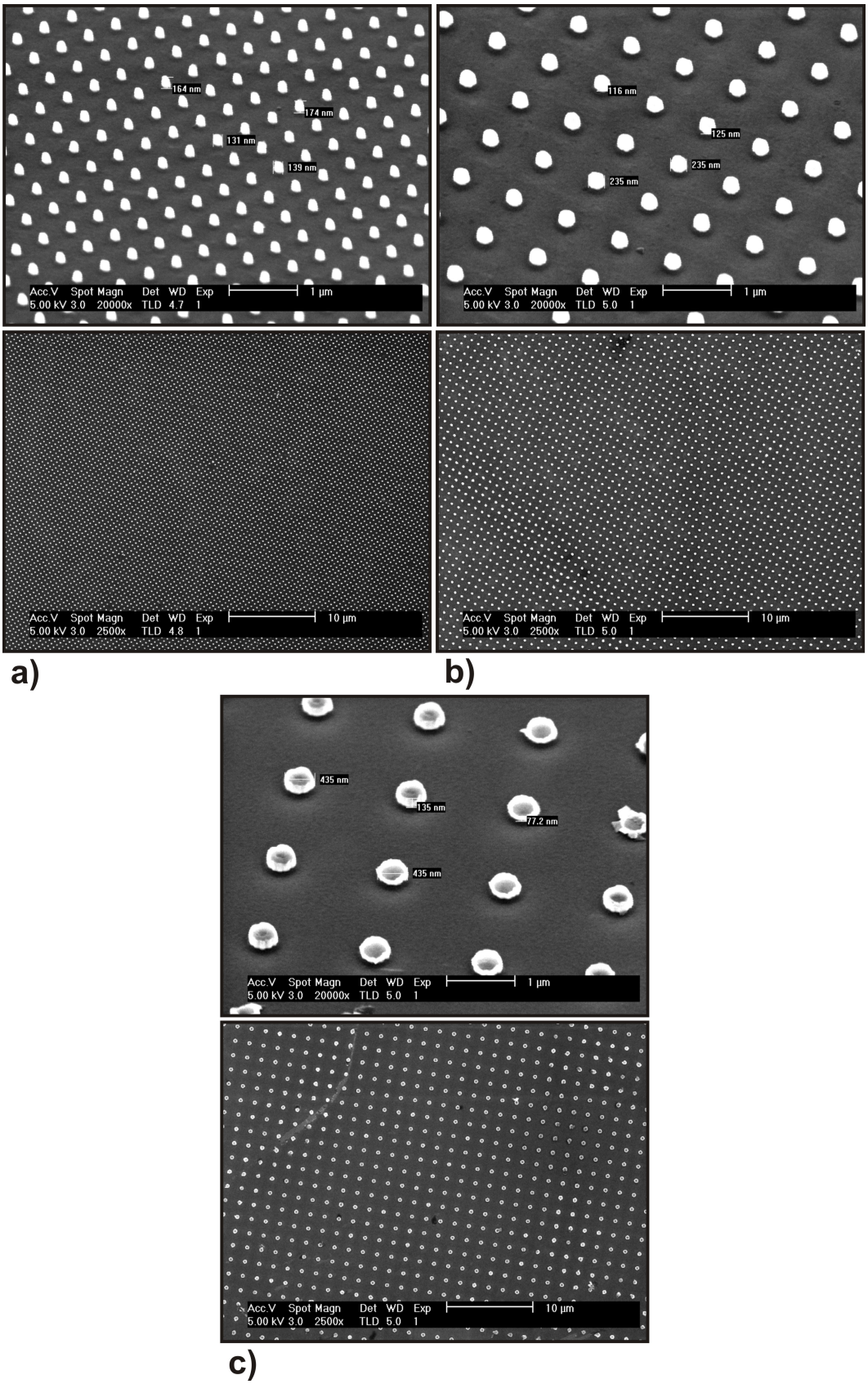

Figure 7.6: SEM images showing both a high magnification image with the sample table tilted at 45° to inspect the dot structure and a low magnification image to observe array quality for dots of diameter a) 140nm, b) 240nm, and c) 440nm.

in order to confirm size, spacing and overall array quality. A selection of these images are shown in figure 7.6.

The high magnification images were taken at a 45° tilt to get an indication of the quality of the top surface. In each sample a high contrast pillar of ∼140-180nm can been seen and is most likely the remaining resist hard mask. Due to the thickness of this cap of >100nm it is unlikely that any interfacial damage will occur as in the work of Read et al. [23]. From the low magnification images the structures are highly uniform with little damage due to cutting of the sample. This shows that the dots produced through etching are mechanically more robust and reproducible over larger areas. It is worth noting that whilst the samples produced via lift-off took a large number of iterations to optimise the film thickness and resist compositions those made via etching required a simple one step process.

The magnetic and thermal properties of the continuous and patterned films were measured in following with the York protocols with identical measurement parameters to those

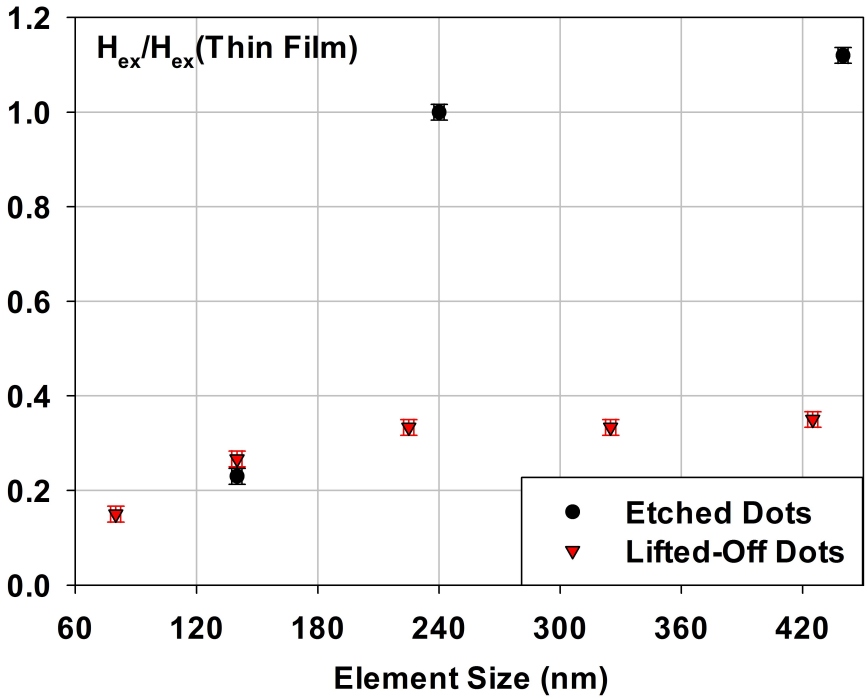

Figure 7.7: Change in H_{ex} with element size for dots produced via etching through a hard mask (black) and lift-off (red).

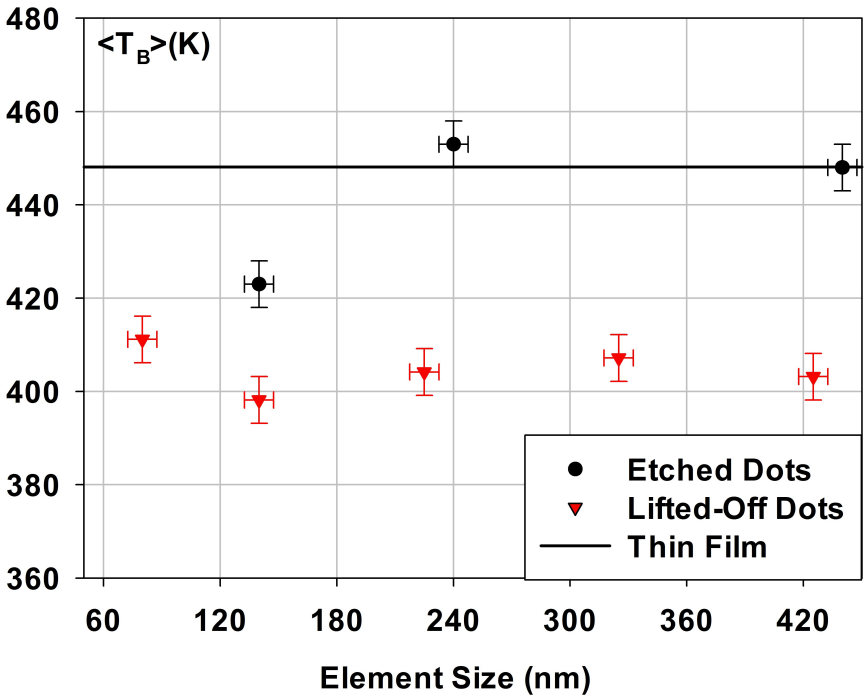

Figure 7.8: The measured change in $\langle T_b \rangle$ with element size for dots produced via etching through a hard mask (black) and lift-off (red) where the line corresponds to the value of the continuous film.

used for the samples produced via lift-off. Whilst no TEM analysis was carried out for these films the magnetic characteristics for the continuous film grown with the etched dots was identical to that in the previous chapter. This coupled with identical growth conditions shows that film grown for the dots produced via lift-off and etching was identical within the resolution of the magnetic measurements.

The effect of the element diameter on H_{ex} for the elements produced via etching and lift-off are shown in figure 7.7. For the 440nm diameter dots produced through etching (black) H_{ex} was 338Oe which is an increase of 36Oe for that obtained for the continuous film. This increased value of H_{ex} decreases with element size, in particular below 240nm which is in agreement with the literature [19, 21, 22] and similar to that of the dots produced through lift-off (red). This shows that the decrease in H_{ex} of 197Oe when patterning through lift-off is caused by poor film quality i.e. domed interfaces when sputtering through a mask. However the difference in H_{ex} between the 425 and 80nm diameter dots is only 15Oe showing that the change in granular structure with element size is negligible. This

Element Size	H_{ex} (±5Oe)	$\langle T_b \rangle$ (±5K)
Continuous Film	302	448
LO - 425nm	105	403
E- 440nm	338	448
LO - 225nm	100	404
E - 240nm	302	453
LO - 140nm	90	398
E - 140nm	70	428

Table 7.2: Summary of key results for the dot size dependence of H_{ex} and $\langle T_b \rangle$ where LO=Lift-off and E=Etched.

is reflected in the results for $\langle T_b \rangle$ reproduced in figure 7.8 and table 7.2. Whereas in the dots produced by etching the difference in H_{ex} between the 440 and 140nm diameter dots is 268Oe. This shows the changes in the sample structure due to patterning become more dominant with decreasing element diameter which implies that it is an edge related effect.

The effect of the element diameter on $\langle T_b \rangle$ for the elements produced via etching (black) and lift-off (red) are shown in figure 7.8. As discussed previously despite the initial change due to patterning in the dots produced via lift-off little change in the granular structure occurs. However for the dots produced by etching $\langle T_b \rangle$ remains equal to that for the continuous films within error for dots of diameter >200nm. The difference in $\langle T_b \rangle$ between dots of diameter 240 and 140nm is 25K which shows that there is a change in the granular structure with decreasing element size.

The effect of lift-off and etching on the granular structure and F/AF interface in exchange biased dots is clearly different in origin. Whilst deposition through a mask and subsequent lift-off leads to an initial decrease in H_{ex} of 197Oe from that of the continuous film a small change of 15Oe is observed with decreasing element size as shown in table 7.2. This shows that the change due to patterning is most likely an interfacial effect which is a result of deposition through a mask i.e. doming of the interface. This is reflected in the results for $\langle T_b \rangle$ where no change is observed. As for the dots produced by Ar ion etching H_{ex} initially increases by 36Oe with respect to the continuous film and consequently decreases by 268Oe with a dot size of 140nm as shown in table 7.2. This peak in H_{ex} shows that the change is an edge grain effect. This is further reflect by a decrease in $\langle T_b \rangle$ of 25K with

element sizes $<$240nm. As to whether this is due to grain cutting [28,29,144] or growth [24] is unclear and further work is required.

Chapter 8

Conclusions and Future Work

8.1 The Interface in Exchange Bias Thin Films

In this study a set of films were deposited as a continuation of the work by Aley et al. [17]. This was done to study the effect of the AF texture on the change in magnetisation reversal during the field annealing and cooling processes. The structures studied were X(x)/CoFe(3)/Ta(5) and X(x)/IrMn(10)/CoFe(3)/Ta(5) where X was a seed layer of NiCr or Cu with thicknesses x=7.5 and 5nm respectively. The texture of the films was confirmed through a series of XRD measurements where it was found that the sample grown on a NiCr seed layer induces a strong (111) in-plane texture in the $IrMn_3$ and consequently a (110) in-plane texture in the CoFe. For the sample grown on a Cu seed layer no texture can be seen in so far as the resolution of the equipment. Whilst the lattice spacing of the (111) plane for Cu and NiCr of $1.09\mathring{A}$ is a close match to that of $IrMn_3$ at $1.13\mathring{A}$ the layer deposition and consequently grain growth [128,129] for the two seed layers is different. This change in the growth process gives the difference in observed texture.

In order to measure the change in the magnetisation process of the ferromagnet due to exchange bias, the setting process of the AF was broken up into its various components. This procedure involved:

1. Growing the CoFe samples directly on the seed layer and measuring first in order to provide a control sample.

2. Measuring the IrMn/CoFe samples as deposited (i.e. without setting) to obtain the effect of disordered $IrMn_3$.

3. Annealing the IrMn/CoFe samples in zero field at a temperature T_{set}=498K for a time t_{set}=1800s and then cooling to T_{ms}=173K and then measuring a hysteresis loop.

4. Annealing the IrMn/CoFe samples in a field H_{set}=5kOe at T_{set}=498K for t_{set}=1800s and then cooling to T_{ms}=173K and measuring two loops in order to observe the training effect.

For the seed/CoFe samples the magnetisation reversal was through domain wall nucleation and reversal with both loops having a squareness of 0.75. However H_c was found to be 43 and 290Oe for the samples grown on the Cu and NiCr seed layers respectively. Whilst there are reports within the literature on the grain size dependence of H_c in polycrystalline CoFe thin films [132–137] the difference in D_m of 1.5nm in this work was insufficient to explain the scale of the change in H_c. It is thought that the difference in H_c was obtained through a variation in the distribution of the magnetocrystalline anisotropy with the (110) in-plane texture in the CoFe leading to an increase in the domain wall pinning . For the seed/IrMn/CoFe samples it was clear that the CoFe couples strongly to the $IrMn_3$ layer. Due to the unset nature of the $IrMn_3$ the magnetisation orientation of the grains are aligned with the easy axis which in the case of the sample grown on the NiCr seed layer is 2-D random in-plane and for the Cu seed layer 3-D random. This leads to loops inidicative of a randomly distributed unidirectional anisotropy superimposed on the uniaxial anisotropy of the CoFe. This gives the skewed loops of squareness 0.19 and 0.45 with H_c=210 and 350Oe for the samples grown on the Cu and NiCr seed layers respectively.

Annealing the seed/IrMn/CoFe samples in zero field was found to give rise to an irreproducible state in the AF. This was due to the remanent magnetisation in the F layer being sufficient to set the AF demonstrating that the AF is set through the exchange interaction with the F layer and not the external applied field. On field cooling the sample grown on the Cu seed layer the measured parameters were H_{ex}=630 and 605Oe for loops 1 and 2 respectively with ΔH_{c1}=60Oe. For the sample grown on the NiCr seed layer the measured parameters were H_{ex}=350 and 345Oe for loops 1 and 2 respectively with ΔH_{c1}=10Oe. The difference in H_{ex} is because the sample grown on the NiCr seed layer could not be

fully set without causing significant layer diffusion. The difference in ΔH_{c1} is thought to be due to the difference in the ordering of the interfacial spin clusters. In the case of the sample grown on the NiCr seed layer where there is a strong (111) in-plane texture the behaviour is thought to be similar to that of a 2-state system. During reversal the ordering of the clusters is maintained and so no training is observed. In the case of the sample deposited on the Cu seed layer the texture is poor giving a 3-D random orientation of the magnetocrystalline anisotropy. The out of plane orientation of the anisotropy field H_K works against the in-plane ordering of the interaction between the clusters giving behaviour similar to that of a biaxial system. After field cooling the clusters are fully aligned, however on reversal to negative saturation the clusters with H_K out of plane will disorient. On return to positive saturation these clusters align with their easy axes giving a decrease in the order of the interfacial spin clusters. This change in ordering leads to a decrease in H_{c1} and the training effect. It is clear from this work that the origins of H_{c1} and H_{c2} are different unlike in a traditional ferromagnet where the magnetisation reversal is symmetric. Therefore the coercivities in an exchange biased film are a manifestation of the energy barriers present in the spin clusters.

To test this hypothesis further the H_{set} dependence of H_{ex} and ΔH_{c1} was measured. For the sample grown on the NiCr seed layer an increase in H_{ex} of 55Oe is seen with H_{set} increasing from 250Oe to 20kOe. This trend is consistent with the work of Fernandez-Outon et al. [25, 26]. No change in ΔH_{c1} is observed which confirms an increase in ordering of a 2-state system where reversal is dictated by the distribution of H_K. For the sample grown on the Cu seed layer a decrease in ΔH_{c1} of 10Oe is observed with H_{set} increasing from 250Oe to 20kOe. This is accompanied by no change in H_{ex} with H_{set} for loop 1. However a change in in H_{ex} with H_{set} is observed in loop 2. The difference in the H_{set} dependence of the two loops is because the first loop takes into account the clusters with H_K out of plane. In the second loop these clusters are disoriented and so it is only the contribution due to the clusters with H_K in-plane that contribute. These results further strengthen the concept that the mechanism of the interface is analagous to that of a system of fine particles.

8.2 Exchange Bias in Nano Elements

In this study 4×4mm arrays of dots of diameters 80, 140, 225, 325, and 425nm were fabricated through lift-off. On patterning H_{ex} was found to decrease from 302Oe in the thin film case to 105Oe for the elements of diameter 425nm. Following this initial drop H_{ex} was found to decrease with element size to 40Oe for the dots 80nm in diameter. These results were compared to a modification of the York Model where grain cutting is assumed to occur at the edge of the elements [28, 29]. Whilst the model succesfully predicted the trend in H_{ex} with element size it failed to come into quantatative agreement. In particular the initial decrease in H_{ex} due to patterning was not predicted. This was thought to be due to a modification of the interface during the patterning process. Due to shadowing effects during deposition through the mask it is unlikely that the film will be perfectly planar. Furthermore deposition of material on the resist walls is known to occur giving a minimum element size dicated by the total layer thickness. As the total layer thickness in this work was 24nm a significant amount of shadowing due to edge growth will have occured. This is particularly the case for elements of size $<$140nm.

In order to confirm this hypothesis the distribution of T_b was measured for each array of elements and calculated using the grain cutting model. Whilst there was relative numerical agreement between the measured and calculated values of $\langle T_b \rangle$ the trend did not fully agree. In the case of the measured values there is no change in $\langle T_b \rangle$ within error whilst the calculated values decrease with respect to element size. As $\langle T_b \rangle$ is dominated by bulk effects [4, 26] this shows that the changes in H_{ex} are predominently due to changes at the interface which is in support of the hypothesis. What is clear from these results is that for the lift-off method the minimum element size is limited by the layer thickness. Any attempts to decrease the film thicknesses to those required for 25nm structures lead to sample characteristics that were not suitable for applications. This is not an issue when the film is patterned by etching through a hard mask.

A preliminary comparison of these methods was carried out were 4×4mm arrays of dots of diameters 140, 240, and 440nm were fabricated by etching through a hard mask. For the dots 440nm in diameter an increase in H_{ex} from 302Oe for the continuous film to 338Oe was measured with no change in $\langle T_b \rangle$. Both H_{ex} and $\langle T_b \rangle$ were then observed to decrease with element size which is in agreement with a change in the granular structure of the AF. Whilst

this could be a process of grain cutting there is evidence that secondary grain growth can occur in etched films [24]. Furthermore etching has been shown to cause significant damage to the F/AF interface through Ar ion and capping layer implantation [23]. However in the case of this work a thick (∼160nm) layer of resist remained on the surface of the structures whilst implantation was found to occur at distances of 3nm from the F/AF interface and so is unlikely to have occured. Therefore the origin of the change in the granular structure is not clear without further work.

The two methods of nano structure fabrication show different behaviour with decreasing element size. Whilst depositing through a mask causes a siginificant decrease in H_{ex} and $\langle T_b \rangle$ very little change occurs with further decreases in element size. However for dots produced through etching little change occurs for large elements, however for dots of diameters less than 240nm there is a rapid degeneneration in H_{ex} and $\langle T_b \rangle$. This shows that there is a significant change in granular structure near the edge of the elements which becomes more dominant with decreasing diameter.

8.3 Future Work and Applications

In order to confirm the validity of the spin clusters hypothesis a model is being developed by Vallejo-Fernandez and O'Grady. However until completion of the model there are a couple of experiments that may be performed to add further weight to the hypothesis. Firstly as has been established exchange bias is temperature dependent. In order to predict the temperature dependence of H_{ex} a baseline must be established. Temperature dependent measurement beginning from as near to 0K as possible are therefore required. Secondly if the cluster ordering in a sample with a poor in-plane (111) texture is dominated by interactions then there will be a strong temperature dependence of ΔH_{c1}. In particular an increase in ΔH_{c1} with decreasing temperature will be expected. This is because initial ordering post field cooling will be greater with decreasing temperature, however on field sweeping there will be insufficient thermal energy to re-establish the original order. Thirdly for the film with a poor texture the appearance of and increase in the H_{set} dependence of H_{ex} with decreasing temperature would be expected. This is because the increase in initial ordering due to a higher setting field will be more stable with decreasing temperature. Finally these

measurements could be compared to a film with a strong in-plane (111) texture where no change in ΔH_{c1} or the H_{set} dependence is expected. This is because the interface will be fully ordered as the ordering is dictated by the H_K of the clusters.

Furthermore the composition and crystal structure of the interface is not clear. A number of works have shown that the deposition of 1-2 atomic layers of Mn at the IrMn/CoFe interface leads to an increase in H_{ex} of up to 25% [146–148]. Furthermore with increasing Mn thickness there is a greater H_{set} dependence of H_{ex} [148]. This behaviour is seen for no other materials where instead a sharp decrease in H_{ex} is observed. Through cross-section TEM and Electron Energy-Loss Spectroscopy (EELS) element mapping the crystal structure and composition at the interface could be measured. However this will be non-trivial as 3 of the 4 expected atoms are Mn, Fe and Co which are near indistiguishable.

In order to confirm the difference between fabrication methods for the nanostructures a full comparison must be made. In particular a reproduction of the work of Basith et al. [24] should be carried out in the context of exchange biased nanostructures. By patterning a continuous film deposited on a SiN membrane the granular structure in the elements could be measured using TEM. This will also allow the measurement of the grain size distributions for multiple individual nanostructures. Furthermore a direct comparison of the change in film quality due to fabrication method can be carried out.

From the literature and the work presented in this thesis it is clear that nano scale patterning leads to a significant decrease in H_{ex} and $\langle T_b \rangle$ with element size [18, 19, 21, 22, 106, 142] due to a modification of the element granular structure [28, 29]. It is therefore necessary to develop a different method for patterning the AF layer in order to continue the current trend of the decrease in read head dimensions. As opposed to patterning a small (5-10nm) grain system the structure could be fabricated from a single crystal or large ($>$100nm) grain AF film. In this way a 'single grain' read head could be produced. In following with the strong domain wall pinning model as discussed in chapter 3 the magnetic and thermal properties of the film could be controlled via doping of the AF [96, 100]. Furthermore this doping could be provided from the etching step as in the work of Read et al. [23]. This should prevent the observed decrease in H_{ex} and $\langle T_b \rangle$ with element size and furthermore decrease the structure to structure variation in thermal properties. Theoretically this would allow for a minimum element size equal to that of the current D_m used which is $\approx$6nm.

Acronyms

AF Antiferromagnet.

AGFM Alternating Gradient Field Magnetometer.

BF Bright Field.

CAD Computer Aided Design.

DC Direct Current.

DF Dark Field.

DI Deionised.

DSP Digital Signal Processing.

EELS Electron Energy-Loss Spectroscopy.

F Ferromagnet.

GMR Giant Magneto Resistance.

HDD Hard Disk Drive.

HiTUS High Target Utilisation Sputtering.

IBD Ion Beam Deposition.

IPA 2-Propanol.

IRM Iso-Thermalremanent Magnetisation.

MBE Molecular Beam Epitaxy.

MOKE Magneto Optical Kerr Effect.

MRAM Magnetic Random Access Memory.

MTJ Magnetic Tunnel Junction.

PLD Pulsed Laser Deposition.

PMGI Polymethylglutarimide.

PMMA Polymethylmethacrylate.

RF Radio Frequency.

RKKY Ruderman, Kittel, Kasuya and Yosida.

SAF Synthetic Antiferromagnet.

SDWP Strong Domain Wall Pinning.

SEM Scanning Electron Microscope.

SNR Signal to Noise Ratio.

TEM Transmission Electron Microscope.

TMR Tunneling Magneto Resistance.

TRM Thermoremanent Magnetisation.

UHV Ultra High Vacuum.

UV Ultraviolet.

UVO Ultraviolet Ozone.

VSM Vibrating Sample Magnetometer.

XRD X-ray Diffractometer.

XRR X-ray Reflectivity.

List of Symbols

D_e Dose.

D Particle Diameter.

F Force.

H_{set} Setting Field.

M_r Remanent Magnetisation.

Z Proton Number.

d Lattice Spacing.

α_{AF} Angle Between the AF Orientation and the Axis.

α_h Angle Between the Applied Field and Easy Axis.

α_{pf} Angle of Scattering Vector k_s With Respect to the Plane of the Film.

β_M Angle Between the Magnetisation of the F and the Axis.

θ_B Bragg Angle.

θ_H Angle Between the Applied Field and the Axis.

θ_U Angle Between M_s and the c Axis.

θ_c Critical Angle.

θ_{ij} Angle Between the Spins i and j.

θ_m Angle Between the Magnetisation and the Easy Axis.

θ Angle from Centre.

$\hat{u}_{ea}$ Deviation from Easy Axis.

$2\theta_\chi$ Rotation Axis Perpendicular to Scattering Plane.

2θ Angle of X-ray Counter WRT Incident X-ray Beam.

χ Sample Rotation Axis Perpendicular to Scattering Plane.

ω X-ray Incident Angle.

ϕ In-plane Rotation.

α_b Beam Half Angle.

$\alpha_1, \alpha_2, \alpha_3$ Cosine of the Angle Between M_s and the Crystal Axis.

H_K^* Pseudo-Anisotropy Field.

K_0 First Anisotropy Term.

K_1 Second Anisotropy Term.

K_2 Third Anisotropy Term.

K_{AF} Antiferromagnet Magnetocrystalline Anisotropy.

K_F Ferromagnet Magnetocrystalline Anisotropy.

K_{sh} Shape Anisotropy Constant.

K_U Uniaxial Anisotropy Constant.

A_c Coil Area.

a_s^2 Area of Interface Per Spin.

a Area.

a_{111} Atomic Spacing In The (111) Plane.

k_B Boltzmann's Constant.

β_s Source Brightness.

ω_0 Amount of Sputtered Particles.

K_c Calibration Constant.

C Capacitance.

Q Charge Density.

C_P Polymer Concentration.

I Current.

i_s Cathode Current Density.

N_a Demagnetising Factor Along the Semi-Minor Axis a.

N_c Demagnetising Factor Along the Semi-Minor Axis c.

N_d Demagnetising Factor.

D_m Median Grain Diameter.

ϵ Electro Motive Force.

E_A Crystal Anisotropy Energy.

E_{ex} Exchange Energy.

E_{max} Maximum Energy of a Uniaxial Particle.

E_{min} Minimum Energy of a Uniaxial Particle.

E_T Total Energy.

E_Z Zeeman Energy.

V_P Critical Value of the Energy Barrier.

$\Delta\sigma$ Interfacial Energy Difference.

σ_d Domain Wall Energy per Unit Area.

ΔE Energy Barrier to Reversal.

A_{es} Exchange Stiffness.

J_{ex} Exchange Integral.

L_{ex} Exchange Length.

c_e Magnitude of the Exchange Constant.

S_{AF} Antiferromagnetic Layer Exchange Stiffness.

A_{exp} Exposure Area.

t_{exp} Exposure Time.

$\alpha/\gamma/\upsilon$ Exponential Factors.

H_s^* Exchange Field Felt by the Interfacial Spin Clusters.

H^* Exchange Field.

H_c Coercive Field.

H_d Demagnetising Field.

$H_{ex\infty}$ Loop Shift as $n_l \Rightarrow \infty$.

H_{ex}^i Exchange Field.

H_{ex} Exchange Field.

H_f Fluctuation Field.

H_K Anisotropy Field.

H_m Molecular Field.

h_n Normalised Field.

B_m Flux Density.

ϕ_F Dipole Flux.

F_M Induced Force.

f_0 Attempt Frequency.

$L(a_L)$ Langevin Function.

k Geometry Constant.

$\bigtriangledown H$ Field Gradient.

H_{c1} First Point of Reversal to -M_s.

H_{c2} Second Point of Reversal to $+M_s$.

H Applied Field.

C^* Interfacial Coupling Constant.

J_{INT} Interfacial Coupling Constant.

J_{net} Effective Interfacial Coupling per Spin.

N_s Number of Interfacial Spins.

d_{hkl} Interplanar Spacing.

a_L Langevin Variable.

L_p Lattice Parameter.

a_l Lattice Constant.

B Magnetic Field.

M_s Saturation Magnetisation.

M Magnetisation per Unit Volume.

m_n Normalised Magnetisation.

$\hat{M}_{FM}$ F Magnetisation Direction.

$\hat{m}_{int}$ AF Interfacial Magnetisation Direction.

μ Arithmetic Mean.

γ_m Molecular Field Constant.

m_{AF} AF Sub-Lattice Moment.

m Moment.

μ_m Magnetic Moment.

N Avogadro's Number.

n_l Number of Consequent Loops.

n Number of Atoms.

n_A Number of Atoms per Unit Cell.

P_{AF} Order Parameter.

h Plank's Constant.

P_{rev} Probability of Reversal.

r_a Anode Radii.

r_c Cathode Radii.

r_{3d} Radius of 3d Shell of Electrons.

r_A Atomic Radius.

R_{dep} Deposition Rate.

r_{dc} Ratio of Direction Coupling and Domain Wall Energies.

P_S Saturation Value of the AF Order.

L_D AF Domain Size.

d_s Spot Size.

S_i Spin Angular Momentum of Atom i.

S_j Spin Angular Momentum of Atom j.

σ Standard Deviation.

T_{act} Activation Temperature.

T_{al} Aligning Temperature.

$\langle T_b \rangle$ Median Blocking Temperature.

T_b Blocking Temperature.

T_C Curie Temperature.

$T_i(B)$ Critical Temperature for a Metastable Domain State.

T_{mp} Melting Temperature.

T_{ms} Temperature During Measurement.

T_{na} Temperature of No Thermal Activation.

T_{set} Setting Temperature.

T_t Transition Temperature.

T Temperature.

T_N Néel Temperature.

D_T Domain Thickness.

t_F Ferromagnetic Layer Thickness.

t_{AF} Antiferromagnetic Layer Thickness.

t_{res} Resist Thickness.

S Time Dependence Coefficient.

t_{al} Aligning Time.

τ Relaxation Time.

t_{ms} Time of Measurement.

t_{set} Setting Time.

t Time.

t_0 Constant of Time.

t_{act} Activation Time.

ΔH_{c1} Training Effect.

g_{hkl} Reciprocal Lattice Vector.

k_g Scattered X-ray Wave Vector.

k_o Incident X-ray Wave Vector.

k_s Scattering Vector.

v Velocity.

ω_v Rotational Velocity.

S_v Coefficient of Viscocity.

η Intrinsic Viscocity.

V Voltage.

V_C Critical Volume Below Which a Grain is Thermally Active for a Given Temperature.

V_{AF} Antiferromagnet Grain Volume.

V_m Median Grain Volume.

V_{set} Volume Set by the Temperature T_{set} Over a Time t_{set}.

λ_e Electron Wavelength.

λ_X X-ray Wavelength.

z_c Number of Order Unity.

References

[1] W. H. Meiklejohn and C. P. Bean, "New Magnetic Anisotropy," *Physical Review*, vol. 102, no. 5, pp. 1413–1414, 1956.

[2] J. Sort, V. Langlais, S. Doppiu, B. Dieny, S. S. Nach, J. S. M. Noz, M. D. Baró, C. Laurent, and J. Nogués, "Exchange Bias Effects in Fe Nanoparticles Embedded in an Antiferromagnetic Cr_2O_3 Matrix," *Nanotechnology*, vol. 15, pp. S211–S214, 2004.

[3] H. Brown, E. D. Dahlberg, and C. Hou, "Exchange Bias Measurements of CoFe/IrMn," *Journal of Applied Physics*, vol. 89, no. 11, pp. 7543–7545, 2001.

[4] K. O'Grady, L. E. Fernandez-Outon, and G. Vallejo-Fernandez, "A New Paradigm for Exchange Bias in Polycrystalline Thin Films," *Journal of Magnetism and Magnetic Materials*, vol. 322, no. 8, pp. 883–899, 2010.

[5] L. Wee, R. L. Stamps, L. Malkinski, Z. Celinski, and D. Skrzypek, "Thermal Training of Exchange Bias in Epitaxial Fe/$KNiF_3$," *Physical Review B*, vol. 69, no. 134425, pp. 1–10, 2004.

[6] J. Keller, P. Miltényi, B. Beschoten, G. Guntherodt, U. Nowak, and K. D. Usadel, "Domain State Model for Exchange Bias. II. Experiments," *Physical Review B*, vol. 66, pp. 1–11, 2002.

[7] S. M. Thompson, "The Discovery, Development and Future of GMR: The Nobel Prize 2007," *Journal of Physics D: Applied Physics*, vol. 093001, pp. 997–1012, 2008.

[8] J. R. Childress and R. E. Fontana, "Magnetic Recording Read Head Sensor Technology," *Comptes Rendus Physique*, vol. 6, pp. 997–1012, 2005.

[9] W. H. Meiklejohn and C. P. Bean, "New Magnetic Anisotropy," *Physical Review*, vol. 105, no. 3, pp. 904–913, 1957.

[10] W. H. Meiklejohn, "Exchange Anisotropy - A Review," *Journal of Applied Physics*, vol. 33, no. 3, pp. 552–570, 1962.

[11] A. P. Malozemoff, "Random-Field Model of Exchange Anisotropy at Rough Ferromagnetic-Antiferromagnetic Interfaces," *Physical Review B*, vol. 35, no. 7, pp. 3679–3682, 1987.

[12] D. Mauri, H. C. Siegmann, P. S. Bagus, and E. Kay, "Simple Model for Thin Ferromagnetic Films Exchange Coupled to an Antiferromagnetic Substrate," *Journal of Applied Physics*, vol. 62, no. 7, pp. 3047–3049, 1987.

[13] U. Nowak, K. D. Usadel, J. Keller, P. Miltényi, B. Beschoten, and G. Guntherodt, "Domain State Model for Exchange Bias. I. Theory," *Physical Review B*, vol. 66, pp. 1–9, 2002.

[14] S. Hassan, "Seagate Technologies," 07 2014. Private Communication.

[15] R. Stearett, W. G. Wang, X. Kou, J. F. Feng, J. M. D. Coey, J. Q. Xiao, and E. R. Nowak, "Influence of Exchange Bias on Magnetic Losses in CoFeB/MgO/CoFeB Tunnel Junctions," *Physical Review B*, vol. 86, pp. 1–11, 2012.

[16] S. Yuasa and D. D. Djayaprawira, "Giant Tunnel Magnetoresistance in Magnetic Tunnel Junctions with a Crystalline MgO (001) Barrier," *Journal of Physics D: Applied Physics*, vol. 40, pp. R337–R354, 2007.

[17] N. P. Aley, G. Vallejo-Fernandez, R. Kroeger, B. Lafferty, J. Agnew, Y. Lu, and K. O'Grady, "Texture Effects in IrMn/CoFe Exchange Bias Systems," *IEEE: Transactions on Magnetics*, vol. 44, no. 11, pp. 2820–2823, 2008.

[18] J. Nogués, J. Sort, V. Langlais, V. Skumryev, B. S. Nach, J. S. M. Noz, and M. D. Baró, "Exchange Bias in Nanostructures," *Physics Reports*, vol. 422, pp. 65–117, 2005.

[19] Y. Shen, Y. Yu, H. Xie, K. Li, J. Qiu, and Z. Guo, "Exchange Bias of Patterned NiFe/IrMn Film," *Journal of Applied Physics*, vol. 91, no. 10, pp. 8001–8003, 2002.

[20] V. Baltz, J. Sort, B. Rodmacq, and B. Dieny, "Size Effects on Exchange Bias in Sub-100nm Ferromagnetic-Antiferromagnetic Dots Deposited of Prepatterned Substrates," *Applied Physics Letters*, vol. 84, no. 24, pp. 4923–4925, 2004.

[21] J. Yu, A. D. Kent, and S. S. P. Parkin, "Exchange Biasing in Polycrystalline Thin Film Microstructures," *Journal of Applied Physics*, vol. 87, pp. 5049–5051, 2000.

[22] V. Baltz, J. Sort, S. Landis, B. Rodmacq, and B. Dieny, "Tailoring Size Effects on the Exchange Bias in Ferromagnetic-Antiferromagnetic $<$100 nm Nanostructures," *Physical Review Letters*, vol. 94, pp. 1–4, 2005.

[23] J. C. Read, P. M. Bracanca, N. Robertson, and J. R. Childress, "Magnetic Degradation of Thin Film Multilayers During Ion Milling," *Applied Physics Letters Materials*, vol. 2, no. 046109, pp. 1–7, 2014.

[24] M. A. Basith, S. McVitie, D. McGrouther, J. N. Chapman, and J. M. R. Weaver, "Direct Comparison of Domain Wall Behavior in Permalloy Nanowires Patterned by Electron Beam Lithography and Focused Ion Beam Milling," *Journal of Applied Physics*, vol. 110, no. 8, pp. 1–8, 2011.

[25] L. E. Fernandez-Outon, K. O'Grady, S. Oh, M. Zhou, and M. Pakala, "Large Exchange Bias IrMn/CoFe for Magnetic Tunnel Junctions," *IEEE: Transactions on Magnetics*, vol. 44, no. 11, pp. 2824–2827, 2008.

[26] L. E. Fernandez-Outon, G. Vallejo-Fernandez, and K. O'Grady, "Interfacial Spin Effects on H_{ex} in Metallic Polycrystalline Exchange Biased Systems," *Journal of Applied Physics*, vol. 103, pp. 1–3, 2008.

[27] B. Kaeswurm and K. O'Grady, "The Origin of Athermal Training in Polycrystalline Metallic Exchange Bias Thin Films," *Applied Physics Letters*, vol. 99, pp. 1–3, 2011.

[28] G. Vallejo-Fernandez and J. N. Chapman, "Size Effects in Submicron Exchange Bias Square Elements," *Applied Physics Letters*, vol. 94, no. 26, pp. 1–3, 2009.

[29] G. Vallejo-Fernandez and J. N. Chapman, "Thermal Stability of Exchange Bias Nanostructures," *Journal of Applied Physics*, vol. 107, pp. 1–3, 2010.

[30] K. Ando, S. Fujita, J. Ito, S. Yuasa, Y. Suzuki, Y. Nakatani, T. Miyazaki, and H. Yoda, "Spin-Transfer Torquen Magnetoresistive Random-Access Memory Technologies for Normally Off Computing," *Journal of Applied Physics*, vol. 115, pp. 1–6, 2014.

[31] L. Thomas, G. Jan, J. Zhu, H. Liu, Y. Lee, S. Le, R. Tong, K. Pi, Y. Wang, D. Shen, R. He, J. Haq, J. Teng, V. Lam, K. Huang, T. Zhong, T. Torng, and P. Wang, "Perpendicular Spin Transfer Torque Magnetic Random Access Memories with High Spin Torque Efficiency and Thermal Stability for Embedded Applications," *Journal of Applied Physics*, vol. 115, pp. 1–6, 2014.

[32] H. Sato, E. C. I. Enobio, M. Yamanouchi, S. Ikeda, S. Fukami, S. Kanai, F. Matsukura, and H. Ohno, "Properties of Magnetic Tunnel Junctions with a MgO/CoFeB/Ta/CoFeB/MgO Recording Structure Down to Junction Diameter of 11nm," *Applied Physics Letters*, vol. 105, pp. 1–4, 2014.

[33] D. Jiles, *Introduction to Magnetism and Magnetic Materials*. Chapman and Hall, 2 ed., 1998.

[34] B. D. Cullity and C. D. Graham, *Introduction to Magnetic Materials*. Wiley, 2 ed., 2009.

[35] J. C. Slater, "The Ferromagnetism of Nickel," *Physical Review*, vol. 49, pp. 537–545, 1936.

[36] S. S. P. Parkin, N. More, and K. P. Roche, "Oscillations in Exchange Coupling and Magnetoresistance in Metallic Superlattice Structures: Co/Ru, Co/Cr and Fe/Cr," *Physical Review Letters*, vol. 64, no. 19, pp. 2304–2307, 1990.

[37] J. Mathon, "Exchange Interactions and Giant Magnetoresistance in Magnetic Multilayers," *Contemporary Physics*, vol. 32, no. 3, pp. 143–156, 1991.

[38] C. D. Mee and E. D. Daniel, *Magnetic Recording*. McGraw-Hill, 2 ed., 1996.

[39] J. C. Slater, "Atomic Shielding Constants," *Physical Review*, vol. 36, pp. 57–64, 1930.

[40] L. Néel and N. Kurti, *Selected Works of Louis Néel*. Gordon and Breach, 1 ed., 1988.

[41] A. Kohn, A. Kovács, R. Fan, G. J. McIntyre, R. C. C. Ward, and J. P. Goff, "The Antiferromagnetic Structures of $IrMn_3$ and their Influence on Exchange Bias," *Nature Scientific Reports*, pp. 1–7, 2013.

[42] I. Tomeno, H. N. Fuke, I. H, M. Sahashi, and Y. Tsunoda, "Magnetic Neutron Scattering Study of Ordered Mn_3Ir," *Journal of Applied Physics*, vol. 86, no. 7, pp. 1–7, 1999.

[43] M. Tsunoda, K. Imakita, M. Naka, and M. Takahashi, "$L1_2$ Phase Formation and Giant Exchange Anisotropy in Mn_3Ir/Co-Fe Bilayers," *Journal of Magnetism and Magnetic Materials*, vol. 304, pp. 55–59, 2006.

[44] N. P. Aley and K. O'Grady, "Compositional Dependence of Antiferromagnetic Anisotropy in IrMn/CoFe Exchange Bias Systems," *Journal of Applied Physics*, vol. 109, no. 7, pp. 1–3, 2011.

[45] L. E. Fernandez-Outon, G. Vallejo-Fernandez, S. Manzoor, B. Hillebrands, and K. O'Grady, "Interfacial Spin Order in Exchange Biased Systems," *Journal of Applied Physics*, vol. 104, pp. 1–3, 2008.

[46] V. Baltz, G. Gaudin, P. Somani, and B. Dieny, "Influence of Edges on the Exchange Bias Properties of Ferromagnetic/Antiferromagnetic Nanodots," *Applied Physics Letters*, vol. 96, no. 26, pp. 1–3, 2010.

[47] G. Vallejo-Fernandez, L. E. Fernandez-Outon, and K. O'Grady, "Measurement of the Anisotropy Constant of Antiferromagnets in Metallic Polycrystalline Exchange Biased Systems," *Applied Physics Letters*, vol. 91, pp. 1–3, 2007.

[48] P. Merodio, A. Ghosh, C. Lemonias, E. Gautier, U. Ebels, M. Chshiev, H. Béa, V. Baltz, and W. E. Bailey, "Penetration Depth and Absorption Mechanisms of Spin Currents in $Ir_{20}Mn_{80}$ and $Fe_{50}Mn_{50}$ Polycrystalline Films by Ferromagnetic Resonance and Spin Pumpng," *Applied Physics Letters*, vol. 104, pp. 1–4, 2014.

[49] G. Vallejo-Fernandez and K. O'Grady, "Effect of the Distribution of Anisotropy Constants on Hysteresis Losses for Magnetic Hyperthermia Applications," *Applied Physics Letters*, vol. 103, pp. 1–4, 2013.

[50] R. C. O'Handley, *Modern Magnetic Materials - Principles and Applications*. John Wiley and Sons, 1 ed., 2000.

[51] J. S. Kouvel, "The Ferromagnetic-Antiferromangetic Properties of Copper-Maganese and Silver-Manganese Alloys," *Journal of Physical Chemistry Solids*, vol. 21, pp. 57–70, 1963.

[52] J. S. Kouvel, "A Ferromagnetic-Antiferromagentic Model for Copper-Maganese and Related Alloys," *Journal of Physical Chemistry Solids*, vol. 24, pp. 795–822, 1963.

[53] Y. Imry and S. K. Ma, "Random-Field Instability of the Ordered State of Continuous Symmetry," *Physical Review Letters*, vol. 35, no. 21, pp. 1399–1401, 1975.

[54] C. L. Chien, V. S. Gornakov, V. I. Nikitenko, A. J. Shapiro, and R. D. Shull, "Antiferromagnetic Spin Structure and Domains in Exchange-Coupled Multilayers," *IEEE Transactions on Magnetics*, vol. 38, no. 5, pp. 2736–2740, 2002.

[55] R. D. Shull, A. J. Shapiro, V. S. Gornakov, V. I. Nikitenko, and H. Zhao, "Stationary Antiferromagnetic Domains During Magnetisation Reversal in an Exchange-Biased FeMn/$Fe_{76}Mn_6C_{18}$ Bilayer," *Journal of Applied Physics*, vol. 93, no. 10, pp. 8603–8605, 2003.

[56] R. Carpenter, G. Vallejo-Fernandez, and K. O'Grady, "Interfacial Spin Cluster Effects in Exchange Bias Systems," *Journal of Applied Physics*, vol. 115, pp. 1–3, 2014.

[57] R. Street, J. C. Woolley, and P. B. Smith, "Magnetic Viscocity under Discontinuously and Continuously Variable Field Conditions," *Proceedings of the Physical Society: B*, vol. 65, no. 9, pp. 679–696, 1952.

[58] P. Gaunt, "Magnetic Viscosity and Thermal Activation Energy," *Journal of Applied Physics*, vol. 59, no. 12, pp. 4129–4132, 1986.

[59] G. Vallejo-Fernandez, N. P. Aley, L. E. Fernandez, and K. O'Grady, "Control of the Setting Process in CoFe/IrMn Exchange Bias Systems," *Journal of Applied Physics*, vol. 104, pp. 1–5, 2008.

[60] G. Vallejo-Fernandez, N. P. Aley, J. N. Chapman, and K. O'Grady, "Measurement of the Attempt Frequency in Antiferromagnets," *Applied Physics Letters*, vol. 97, pp. 1–3, 2010.

[61] R. L. Stamps, "Mechanisms for Exchange Bias," *Journal of Physics D: Applied Physics*, vol. 33, pp. R247–R268, 2000.

[62] R. Jungblut, R. Coehoorn, M. T. Johnson, J. aan de Stegge, and A. Reinders, "Orientation Dependence of the Exchange Biasing in Molecular-Beam-Epitaxy-Grown $Ni_{80}Fe_{20}/Fe_{50}Mn_{50}$ Bilayers," *Journal of Applied Physics*, vol. 75, no. 10, pp. 6659–6664, 1994.

[63] L. Néel, "Ferro-Antiferromagnetic Coupling in Thin Layers," *Annales de Physique*, vol. 61, no. 2, 1967.

[64] H. Zijlstra, "Coping with Brown's Paradox: The Pinning and Nucleation of Magnetic Domain Walls at Antiphase Boundaries," *IEEE Transactions on Magnetics*, vol. 15, no. 5, pp. 1246–1250, 1979.

[65] N. C. Koon, "Calculations of Exchange Bias in Thin Films with Ferromagnetic/Antiferrromagnetic Interfaces," *Physical Review Letters*, vol. 78, no. 25, pp. 4865–4868, 1997.

[66] T. C. Schulthess and W. H. Butler, "Consequences of Spin-Flop Coupling in Exchange Biased Films," *Physical Review Letters*, vol. 81, no. 81, pp. 4516–4519, 1998.

[67] T. C. Schulthess and W. H. Butler, "Coupling Mechanisms in Exchange Biased Films," *Journal of Applied Physics*, vol. 85, no. 8, pp. 5510–5515, 1999.

[68] J. Nogues, D. Lederman, T. J. Morgan, and I. K. Schuller, "Positive Exchange Bias in FeF_2-Fe Bilayers," *Physical Review Letters*, vol. 76, no. 24, pp. 4624–4627, 1996.

[69] J. Nogues, D. Lederman, T. J. Morgan, I. K. Schuller, and K. V. Rao, "Large Exchange Bias and its Connection to Interface Structure in FeF_2-Fe Bilayers," *Applied Physics Letters*, vol. 68, pp. 3186–3188, 1996.

[70] A. P. Malozemoff, "Mechanisms of Exchange Anisotropy," *Journal of Applied Physics*, vol. 63, pp. 3874–3879, 1988.

[71] W. Kleemann, "Random-Field Induced Antiferromangetic, Ferroelectric and Structural Domain States," *International Journal of Modern Physics B*, vol. 7, no. 13, pp. 2469–2475, 1992.

[72] S. J. Han, D. P. Belanger, W. Kleemann, and U. Nowak, "Relaxation of the Excess Magnetization of Random-Field-Induced Metastable Domains in $Fe_{0.47}Zn_{0.53}F_2$," *Physical Review B*, vol. 45, no. 17, pp. 9728–9735, 1992.

[73] D. P. Belanger, S. M. Rezende, A. R. King, and V. Jaccarino, "Hysteresis, Metastability and Time Dependence in d=2 and d=3 Random Field Ising Systems," *Journal of Applied Physics*, vol. 57, pp. 3294–3299, 1985.

[74] U. Nowak, A. Misra, and K. D. Usadel, "Modelling Exchange Bias Microscopically," *Journal of Magnetism and Magnetic Materials*, vol. 240, pp. 1–7, 2002.

[75] G. Scholten, K. D. Usadel, and U. Nowak, "Coercivity and Exchange Bias of Ferromagnetic/Antiferromagnetic Multilayers," *Physical Review B*, vol. 71, pp. 1–7, 2005.

[76] M. Ali, C. H. Marrows, and B. J. Hickey, "Onset of Exchange Bias in Ultrathin Antiferromagnetic Layers," *Physical Review B*, vol. 67, pp. 1–4, 2003.

[77] E. Fulcomer and S. H. Charap, "Thermal Fluctuation Aftereffect Model for Some Systems with Ferromagnetic-Antiferromagnetic Coupling," *Journal of Applied Physics*, vol. 43, no. 10, pp. 4190–4199, 1972.

[78] E. Fulcomer and S. H. Charap, "Temperature and Frequency Dependence of Exchange Anisotropy Effects in Oxidized NiFe Films," *Journal of Applied Physics*, vol. 43, no. 10, pp. 4184–4189, 1972.

[79] S. H. Charap and S. H. Fulcomer, "Slow Wall Motion in Oxidized Permalloy Films," *Physica Status Solidi (a)*, vol. 11, pp. 559–565, 1972.

[80] D. Paccard, C. Schlenker, O. Massenet, R. Montmory, and A. Yelon, "A New Property of Ferromagnetic-Antiferromagnetic Coupling," *Physica Status Solidi (b)*, vol. 16, no. 1, pp. 301–311, 1966.

[81] F. B. Hagedorn, "Exchange Anisotropy in Oxidized Permalloy Thing Films at Low Temperatures," *Journal of Applied Physics*, vol. 38, no. 9, pp. 3641–3645, 1967.

[82] C. Schlenker, "Couplage Ferro-Antiferromagnetique et Trainage Magnetique dans des Couches Minces Multiples Co-CoO et Ni-NiO Par," *Physica Status Solidi (b)*, vol. 28, no. 2, pp. 507–517, 1968.

[83] P. A. A. van der Heijden, T. F. M. M. Maas, J. C. S. Kools, F. Roozeboom, P. J. van der Zaag, and W. J. M. de Jonge, "Influences on Relaxation of Exchange Biasing in NiO/$Ni_{66}Co_{18}Fe_{16}$ Bilayers," *Journal of Applied Physics*, vol. 83, no. 11, pp. 7207–7209, 1998.

[84] P. A. A. van der Heijden, T. F. M. M. Maas, W. J. M. de Jonge, J. C. S. Kools, F. Roozeboom, and P. J. van der Zaag, "Thermally Assisted Reversal of Exchange Biasing in NiO and FeMn Based Systems," *Applied Physics Letters*, vol. 72, no. 4, pp. 492–494, 1998.

[85] M. D. Stiles and R. D. McMichael, "Model of Exchange Bias in Polycrystalline Ferromagnetic-Antiferromagnetic Bilayers," *Physical Review B*, vol. 59, no. 5, pp. 3722–3733, 1999.

[86] M. D. Stiles and R. D. McMichael, "Temperature Dependence of Exchange Bias in Polycrystalline Ferromagnetic-Antiferromagnetic Bilayers," *Physical Review B*, vol. 60, no. 18, pp. 12950–12956, 1999.

[87] M. D. Stiles and R. D. McMichael, "Coercivity in Exchange-Bias Bilayers," *Physical Review B*, vol. 63, pp. 1–10, 2001.

[88] K. Takano, R. H. Kodama, A. E. Berkowitz, W. Ca, and G. Thomas, "Interfacial Uncompensated Antiferromagnetic Spins: Role in Unidirectional Anisotropy in Polycrystalline $Ni_{81}Fe_{19}$/CoFe Bilayers," *Physical Review Letters*, vol. 79, no. 6, pp. 1130–1133, 1997.

[89] L. E. Fernandez-Outon, K. O'Grady, and M. J. Carey, "Thermal Phenomena in IrMn Exchange Biased Systems," *Journal of Applied Physics*, vol. 95, no. 11, pp. 6852–6852, 2004.

[90] M. Futamoto, N. Inaba, Y. Hirayama, K. Ito, and Y. Honda, "Compositional Microstructure and Micromagnetics of Co-Based Thin Film Media," *Materials Research Society Symposium Proceedings*, vol. 517, pp. 1–4, 1998.

[91] G. Vallejo-Fernandez, L. E. Fernandez, and K. O'Grady, "Antiferromagnetic Grain Volume Effects in Metallic Polycrystalline Exchange Bias Systems," *Journal of Physics D: Applied Physics*, vol. 41, pp. 1–5, 2008.

[92] M. El-Hilo, K. O'Grady, and R. W. Chantrell, "The Origin of Non-Linear ln(t) Behaviour in the Time Dependence of Magnetisation," *Journal of Magnetism and Magnetic Materials*, vol. 109, pp. L164–L168, 1992.

[93] L. E. Fernandez-Outon, G. Vallejo-Fernandez, S. Manzoor, B. Hillebrands, and K. O'Grady, "Interfacial Spin Order in Exchange Biased Systems," *Journal of Applied Physics*, vol. 104, pp. 1–3, 2008.

[94] J. D. Dutson, C. Huerrich, G. Vallejo-Fernandez, L. E. Fernandez-Outon, G. Yi, S. Mao, R. W. Chantrell, and K. O'Grady, "Bulk and Interfacial Effects in Exchange Bias Systems," *J. Phys. D: Appl. Phys.*, vol. 40, pp. 1293–1299, 2007.

[95] A. Hoffmann, "Symmetry Driven Irreversibilities at Ferromagnetic-Antiferromagnetic Interfaces," *Physical Review Letters*, vol. 93, no. 9, pp. 1–4, 2004.

[96] G. Vallejo-Fernandez and K. O'Grady, "Effect of Non-Magnetic Dilutions on the Blocking Temperature of Exchange Biased Systems," *IEEE: Transactions on Magnetics*, vol. 47, no. 10, pp. 3304–3307, 2011.

[97] A. Mougin, T. Mewes, R. Lopusnik, M. Jung, D. Engel, A. Ehresmann, H. Schmoranzer, J. Fassbender, and B. Hillebrands, "Modification of the Exchange Bias Effect by He Ion Irradiation," *IEEE Transactions on Magnetics*, vol. 36, no. 5, pp. 2647–2649, 2000.

[98] M. Fecioru-Morario, S. R. Alo, C. Papusoi, M. Sperlich, and G. Guntherodt, "Effects of Cu Dilution in IrMn on the Exchange Bias of CoFe/IrMn Bilayers," *Physical Review Letters*, vol. 99, pp. 1–4, 2007.

[99] N. P. Aley, C. Bonet, B. Lafferty, and K. O'Grady, "Effect of Cu Impurities on K_{AF} in $IrMn_{1-x}Cu_x$/CoFe Exchange Bias Systems," *IEEE Transactions on Magnetics*, vol. 45, no. 10, pp. 3858–3861, 2009.

[100] G. Vallejo-Fernandez, B. Kaeswurm, and K. O'Grady, "Defect and Impurity Effects in Exchange Bias Systems," *Journal of Applied Physics*, vol. 109, pp. 1–3, 2011.

[101] B. A. Joyce, "Molecular Beam Epitaxy - Fundamentals and Current Status," *Contemporary Physics*, vol. 31, no. 3, pp. 195–197, 1990.

[102] M. N. R. Ashfold, F. Claeyssens, G. M. Fuge, and S. J. Henley, "Pulsed Laser Ablation and Deposition of Thin Films," *Chemical Society Review*, vol. 33, pp. 23–31, 2003.

[103] K. Wasa, I. Kanno, and H. Kotera, *Handbook of Sputter Deposition Technology*. Elsevier, 2 ed., 2012.

[104] M. Vopsaroiu, G. Vallejo-Fernandez, M. J. Thwaites, J. Anguita, P. J. Grundy, and K. O'Grady, "Deposition of Polycrystalline Thin Films with Controlled Grain Size," *Journal of Physics D: Applied Physics*, vol. 38, pp. 490–496, 2005.

[105] M. J. Thwaites, "High Density Plasmas," *US Patent No. US 6,463,873 B1*, 2002.

[106] R. Carpenter, A. J. Vick, A. Hirohata, G. Vallejo-Fernandez, and K. O'Grady, "Effect of Grain Cutting in Exchange Biased Nanostructures," *Journal of Applied Physics*, vol. 115, pp. 1–3, 2014.

[107] M. J. Madou, *Fundamentals of Microfabrication and Nanotechnology: Volume 2*. CRC Press, 3 ed., 2012.

[108] O. Helliweg, J. K. Bosworth, E. Dobisz, D. Kercher, T. Hauet, G. Zeltzer, J. D. Risner-Jamtgaard, D. Yaney, and R. Ruiz, "Bit Patterned Media Based on Block Copolymer Directed Assembly with Narrow Magnetic Switching Field Distribution," *Applied Physics Letters*, pp. 1–3.

[109] K. Suzuki and B. W. Smith, *Microlithography - Science and Technology*. CRC Press, 2 ed., 2007.

[110] D. Chescoe and P. J. Goodhew, *The Operation of Transimission and Scanning Electron Microscopes*. Oxford University Press, 1 ed., 1990.

[111] M. D. Graef and M. E. Mchenry, *Structure of Materials*. Cambridge University Press, 2 ed., 2012.

[112] D. B. Williams and C. B. Carter, *Transmission Electron Microscopy: A Textbook for Materials Science*. Springer, 3 ed., 2009.

[113] L. University, "Introduction to Electron Microscopes." http://www.materials.ac.uk/elearning/matter/introductiontoelectronmicroscopes/tem/introduction.html/. [Online; accessed 01-January-2015].

[114] J. H. Wittke, "Introduction to Scanning Electron Microscopes." http://www4.nau.edu/microanalysis/microprobe-sem/instrumentation.html/. [Online; accessed 01-January-2015].

[115] C. G. Granqvist and R. A. Buhrman, "Ultrafine Metal Particles," *Journal of Applied Physics*, vol. 47, pp. 2200–2219, 1976.

[116] G. R. Jones, M. Jackson, and K. O'Grady, "Determination of Grain Size Distributions in Thin Films," *Journal of Magnetism and Magnetic Materials*, vol. 193, no. 1-3, pp. 75–78, 1999.

[117] Rigaku, "The Bridge," 07 2014. Private Communication.

[118] P. J. Flanders, "An Alternating-Gradient Magnetometer," *Journal of Applied Physics*, vol. 63, no. 8, pp. 3940–3945, 1988.

[119] K. O'Grady, V. G. Lewis, and D. P. E. Dickson, "Alternating Gradient Force Magnetometry: Applications and Extension to Low Temperatures," *Journal of Applied Physics*, vol. 73, no. 5608, pp. 5608–5613, 1993.

[120] E. O. Samwel, T. Bolhuis, and J. C. Lodder, "An Alternative Approach to Vector Vibrating Sample Magnetometer Detection Coil Setup," *Review of Scientific Instruments*, vol. 69, no. 9, pp. 3204–3209, 1998.

[121] S. Foner, "Versatile and Sensitive Vibrating-Sample Magnetometer," *Review of Scientific Instruments*, vol. 30, no. 7, pp. 548–557, 1959.

[122] H. J. Richter, "On the Construction of Detection Coils for a Vectorial Vibrating Sample Magnetometer," *Journal of Magnetism and Magnetic Materials*, vol. 111, no. 1-2, pp. 201–213, 1992.

[123] X. Peng, A. Morrone, K. Nikolaev, M. Kief, and M. Otrowski, "Effect of Material Selection and Background Impurity on Interface Property and Resulted CIP-GMR

Performance," *Journal of Magnetism and Magnetic Materials*, vol. 321, pp. 2902–2910, 2009.

[124] M. Pakala, Y. Huai, G. Anderson, and L. Miloslavsky, "Effect of Underlayer Roughness, Grain Size, and Crystal Structure on Exchange Coupled IrMn/CoFe Thin Films," *Journal of Applied Physics*, vol. 87, no. 9, pp. 6653–6655, 2000.

[125] C. V. Thompson, "Grain Growth in Polycrystalline Thin Films of Semiconductors," *Interface Science*, vol. 6, no. 83, pp. 85–93, 1998.

[126] C. V. Thompson, "Structure Evolution During Processing of Polycrystalline Thin Films," *Annual Review of Material Science*, vol. 30, pp. 159–190, 2000.

[127] A. E. Lita and J. E. S. Jr., "Charaterization of Surface Structure in Sputtered Al Films: Correlation to Microstructure Evolution," *Journal of Applied Physics*, vol. 85, no. 2, pp. 876–882, 1998.

[128] C. V. Thompson and R. Carel, "Texture Development in Polycrystalline Thin Films," *Materials Science and Engineering B*, vol. 32, pp. 211–219, 1995.

[129] Paritosh, D. J. Srolovitz, C. C. Battaile, X. Li, and J. E. Butler, "Simulation of Faceted Film Growth in Two-Dimensions: Microstructure, Morphology and Texture," *Acta Metallurgica*, vol. 47, no. 7, pp. 2269–2281, 1999.

[130] A. M. Brown and M. F. Ashby, "Correlations for Diffusion Constants," *Acta Metallurgica*, vol. 28, pp. 1085–1101, 1980.

[131] J. Sagar, C. N. T. Yu, L. Lari, and A. Hirohata, "Growth of Polycrystalline Heusler Alloys for Spintronic Devices," *Journal of Physics D: Applied Physics*, vol. 47, pp. 1–4, 2014.

[132] M. Vopsaroiu, K. O'Grady, M. T. Georgieva, P. J. Grundy, and M. J. Thwaites, "Growth Rate Effects in Soft CoFe Films," *IEEE: Transactions on Magnetics*, vol. 41, no. 10, pp. 3253–3255, 2005.

[133] M. Vopsaroiu, M. T. Georgieva, P. J. Grundy, M. J. Thwaites, and K. O'Grady, "Preparation of High Moment CoFe Films with Controlled Grain Size and Coercivity," *Journal of Applied Physics*, vol. 97, pp. 1–3, 2005.

[134] C. L. Platt, A. E. Berkowitz, D. J. Smith, and M. R. McCartney, "Correlation of Coercivity and Microstructure of Thin CoFe Films," *Journal of Applied Physics*, vol. 88, no. 4, pp. 2058–2062, 2000.

[135] H. S. Jung, W. D. Doyle, J. E. Wittig, J. F. Al-Sharab, and J. Bentley, "Soft Anisotropic High Magnetisation Cu/FeCo Films," *Applied Physics Letters*, vol. 81, no. 13, pp. 2415–2417, 2002.

[136] H. S. Jung and W. D. Doyle, "CoFe-IrMn Exchange-Coupled Soft Underlayers for Perpendicular Media," *IEEE: Transactions on Magnetics*, vol. 38, no. 5, pp. 2015–2017, 2002.

[137] H. S. Jung, W. D. Doyle, and S. Matsunuma, "Influence of Underlayers on the Soft Properties of High Magnetization FeCo Films," *Journal of Applied Physics*, vol. 93, no. 10, pp. 6462–6464, 2003.

[138] G. Herzer, "Grain Size Dependence of Coercivity and Permeability in Nanocrystalline Ferromagnets," *IEEE: Transactions on Magnetics*, vol. 26, no. 5, pp. 1397–1402, 1990.

[139] J. Nogués and I. K. Schuller, "Exchange Bias," *Journal of Magnetism and Magnetic Materials*, vol. 192, pp. 203–232, 1999.

[140] C. Y. Hung, M. Mao, S. Funada, T. Schneider, L. Miloslavsky, M. Miller, C. Qian, and H. C. Tong, "Exchange Biasing and Thermal Stability of CoFe/PtPdMn Films," *Journal of Applied Physics*, vol. 87, no. 9, pp. 4915–4917, 2000.

[141] S. Chikazumi and S. H. Charap, *Physics of Magnetism*. John Wiley and Sons, 1 ed., 1964.

[142] J. Sort, H. Glaczynska, U. Ebels, B. Dieny, M. Giersig, and J. Rybczynski, "Exchange Bias Effects in Submicron Antiferromagnetic-Ferromagnetic Dots Prepared by Nanosphere Lithography," *Journal of Applied Physics*, vol. 95, pp. 7516–7518, 2004.

[143] I. Sasaki, R. Nakatani, K. Ishimoto, Y. Endo, Y. Shiratsuchi, Y. Kawamura, and M. Yamamoto, "Size Effects on Exchange Bias in Polycrystalline Ni-Fe/Fe-Mn Square Dots," *Journal of Magnetism and Magnetic Materials*, vol. 310, pp. 2677–2679, 2007.

[144] V. Baltz, G. Gaudin, P. Somani, and B. Dieny, "Influence of Edges on the Exchange Bias Properties of Ferromagnetic/Antiferromagnetic Nanodots," *Applied Physics Letters*, vol. 96, pp. 1–3, 2010.

[145] K. A. Seu, H. Huang, J. F. Lesoine, H. D. Showman, J. W. F. Egelhoff, L. Gan, and A. C. Reilly, "Co Layer Thickness Dependence of Exchange Biasing for IrMn/Co and FeMn/Co," *Journal of Applied Physics*, vol. 93, no. 10, pp. 6611–6613, 2003.

[146] M. Tsunoda, S. Yoshitaki, Y. Ashizawa, D. Y. Kim, C. Mitsumata, and M. Takahashi, "Enhancement of Exchange Bias by Ultra-Thin Mn Layer Insertion at the Interface of Mn-Ir/Co-Fe Bilayers," *Physica Status Solidi b*, vol. 244, no. 12, pp. 4470–4473, 2007.

[147] M. Ali, C. H. Marrows, and B. J. Hickey, "Controlled Enhancement or Suppression of Exchange Biasing Using Impurity δ Layers," *Physical Review B*, vol. 77, pp. 1–7, 2008.

[148] R. Carpenter, N. C. Cramp, and K. O'Grady, "Effect of Mn Interface Doping in Polycrystalline Exchange Bias Thin Films," *IEEE: Transactions on Magnetics*, vol. 48, no. 11, pp. 4351–4354, 2012.